UNIVERSITÉ DE GENÈVE
Dèpartement de Physique de la Matiére
Condensèe

FACULTÉ DES SCIENCES
Professeur D. van der Marel

Towards a quantitative understanding of the high T_C phenomenon.

THÈSE

présenté à la Faculté des Sciences de l'Université de Genève
pour obtenir le grade de docteur ès Sciences, mention science

par

Erik van Heumen
de
Amsterdam (Netherlands)

Thèse n° 0001

GENÈVE
Atelier de reproduction de la Section de Physique
2009

Abstract

English

High temperature superconductivity is one of the enigmas of contemporary condensed matter physics. Twenty years of research have uncovered many aspects of these materials with as many, sometimes orthogonal, explanations. The nature of the superconducting state remains a puzzle, but hopes are that an understanding of this phenomenon will open the way to designing materials with even higher superconducting transition temperatures. This thesis is an experimentalist's approach to understanding the phenomenon of high temperature superconductivity. The tool of choice will be optical spectroscopy: one of the three tools that were historically important in the understanding of "conventional" superconductivity in metals, the other two being acoustic attenuation and tunneling spectroscopy. In the absence of any interaction of the electrons with impurities, the lattice vibrations (known as phonons) or other electrons, the optical conductivity is given by a zero frequency δ-function. Any interaction will give rise to a broadening of this peak. The width and frequency dependence of the resulting AC conductivity contains information on the interactions responsible for the broadening. In conventional superconductors the relevant interaction for the occurrence of superconductivity is the electron-phonon interaction. Using a theoretical description known as the Migdal-Eliashberg-Nambu theory (from here on strong coupling theory), and measurements of the phonon spectral density, predictions can be made about the superconducting properties of a material, like the critical temperature below which superconductivity sets in. Under certain approximations it is possible to extract this phonon density of states from optical experiments. Before the discovery of high temperature superconductivity it was widely believed that the highest possible critical temperatures were of the order of 40 K. As a result the discovery of superconductivity at more than twice that temperature, forced the conclusion that the old theory had to be abandoned. In this thesis I will present a detailed analysis of optical experiments using this "old" theory as a starting point. There is an increasing body of experimental work that indicates that the interaction between electrons at a low energy scale can be described by this formalism. I will make the *a priori* assumption that the strong coupling theory can

be used as a first approximation or effective theory. The goal will be to extract from the optical experiments a spectral density similar to the phonon spectral density for conventional superconductors. This can then be used to make predictions about other properties of these materials and thereby test if the theory can be self-consistently applied. In the first chapter I will point out some recent advances in the field, and recapitulate some well known beliefs. The second chapter details the tools and methods of optical spectroscopy. Chapter three and four outline the experimental results obtained during the course of this work. Chapter five of this thesis describes aspects of the strong coupling theory and an analysis of the experiments. I will in particular show that the temperature dependence of the optical spectra is determined accurately by this formalism. In chapter six is is shown that these results have important consequences for the optical sum rule. Finally, in the seventh and last chapter the picture emerging from the previous two chapters is discussed: that of electrons strongly interacting through the exchange of bosons. These bosons turn out to have both an electronic and phononic origin. The analysis is extended and compared to experimental results obtained in other studies and by other methods. I will show that the normal state for optimally doped and overdoped cuprates can be described within the Migdal-Eliashberg-Nambu framework. The final result presented in this thesis is a reproduction of the famous dome of critical temperatures calculated using the spectral densities extracted from experiments.

French

La supraconductivité à haute température est l'une des énigmes de la physique du solide moderne. En 20 ans de recherches, de nombreuses découvertes on été faire avec autant d'interprétations parfois orthogonales. La nature de l'état supraconducteur dans ces matériaux demeure un puzzle mais l'enjeu est de taille car comprendre les phénomènes physiques à son origine, c'est se donner la possibilité d'élaborer des matériaux avec des transitions supraconductrice à des températures bien plus élevées.

Cette thèse est une approche expérimentale pour comprendre le phénomène de la supraconductivité à haute température par des méthodes de spectroscopie optique. Cette technique a été choisie car elle a été l'un des trois outils qui ont fait la lumière sur le mécanisme de la supraconductivité conventionnelle avec l'atténuation acoustique et la spectroscopie à effet tunnel.

En l'absence d'interaction d'un electron avec des impuretés, les vibrations du réseau crystallin (phonons) ou les autres électrons, la conductivité optique est une fonction de Dirac à fréquence nulle. Toute interaction se traduit par un élargissement de cette fonction. La

largeur de ce pic et la dépendance en fréquence de la conductivité contiennent des informations importantes sur cet élargissement. Dans les supraconducteurs dits conventionnels, l'interaction responsable de la supraconductivité est l'interaction électron-phonon. En combinant la théorie de Migdal-Eliashberg-Nambu (pour des couplages forts) et des mesures de densité spectral de phonon, il est possible de prédire de nombreuses propriétés d'un matériaux parmi lesquelles la température à laquelle la supraconductivité apparaît. Sous certaines conditions, il est possible d'extraire la densité d'état de phonons de mesures optiques.

Avant l'avènement de la supraconductivité à haute température, il était convenu que la plus haute température possible pour une transition supraconductrice était de l'ordre de 40 K. La découverte de températures de transitions plus de deux fois supérieures a conduit à l'abandon des "vielles théories".

Dans cette thèse, je vais présenter une analyse détaillée d'expériences optiques en utilisant cette "vielle théorie" comme point de départ. Un nombre croissant de travaux expérimentaux montrent que les interactions entre électrons peuvent être décrites en utilisant ce formalisme. Je vais donc présumer que la théorie de couplage fort peut être utilisée comme une première approximation. Le but consiste à extraire d'expériences optiques, une densité spectrale similaire à la densité de phonon dans le mécanisme de la supraconductivité conventionnelle.

Dans le premier chapitre, je vais présenter les dernières avancées dans ce domaine et récapituler les quelques fondements ou "croyances" précédemment établis. Le second chapitre détaillera l'outil de la spectroscopie optique et les méthodes d'analyse des données. Les chapitres 3 et 4 présenteront les principaux résultats expérimentaux de ce travail, et une analyse de ces données au travers de la théorie du couplage fort fera l'objet du cinquième chapitre. Je montrerai en particulier que la dépendance en température de ces spectres optiques peut être décrite avec une grande précision par ce formalisme. Dans le chapitre 6, je montrerai que ces résultats ont un impact important sur les règles de somme optique. Finalement, dans le chapitre 7, une image émergente des deux chapitres précédents sera discutée: celle de phonon en forte interaction d'échange avec des bosons. Ces bosons étant d'origine à la fois électronique et phononiques. Cette analyse est étendue et comparée à des résultats expérimentaux issus d'autres méthodes de mesure. Je montrerai que l'état normal de cuprates au dopage optimal et sur-dopés peut être décrit dans le cadre de la théorie Migdal-Eliashberg-Nambu. L'image finale de ce travail est la reproduction du fameux dôme de températures critiques en fonction du dopage calculé uniquement à partir des densités spectrales extraites des données optiques.

Contents

1 Introduction **1**

1.1 The road to high temperature superconductivity. 1

1.2 From Mott insulator to Fermi liquid 3

1.3 Correlations and superconductivity 6

2 Theory of Optical Spectroscopy **11**

2.1 Introduction 11

2.2 Electromagnetism and Matter 12

2.2.1 Maxwell's equations 12

2.2.2 Linear Response Theory 13

2.2.3 Kramers-Kronig relations 15

2.2.4 Polaritons 16

2.3 Experimental Techniques 20

2.3.1 Reflection and Transmission at an interface 20

2.3.2 Reflectivity experiments 21

2.3.3 Grazing Incidence Experiments 23

2.3.4 Spectroscopic Ellipsometry 25

2.4 Quantum theory 27

2.4.1 The Kubo-formalism 29

2.4.2 Sum Rules 31

2.4.3 Applications of sum rules to superconductors 35

2.4.4 Extended Drude formalism 38

3 Optical spectroscopy of high-T_c superconductors: $HgBa_2CuO_{4+\delta}$. 41

3.1 Introduction . . . 41
3.2 Experimental details . . . 41
3.3 $HgBa_2CuO_{4+\delta}$ . . . 43
3.4 Sample . . . 45
3.5 Reflectivity experiments . . . 45
3.6 Ellipsometry . . . 48
3.7 Optical conductivity . . . 48
3.8 Specific heat measurements . . . 50
3.9 Extended Drude analysis . . . 51
3.10 Superfluid density . . . 52
3.11 Low frequency spectral weight . . . 54
3.12 Specific heat anomaly . . . 58

4 Doping dependent optical properties of $Bi_2Sr_2CuO_{6+\delta}$. 61

4.1 Introduction . . . 61
4.2 Samples . . . 62
4.3 Normal incidence reflectivity. . . . 62
4.4 Grazing incidence reflectivity . . . 63
4.5 Ellipsometry . . . 64
4.6 In-plane conductivity . . . 65
4.7 c-axis conductivity . . . 66
4.8 Extended Drude analysis . . . 68

5 Analysis of optical spectra and the strong coupling formalism. 71

5.1 Introduction . . . 71
5.2 Strong coupling theory . . . 71
5.3 The bosonic spectral function $\tilde{\Pi}(\omega)$ . . . 75
5.3.1 Marginal Fermi liquid. . . . 75
5.3.2 Spin fluctuation theory. . . . 76
5.3.3 MFL and MMP + phonon models . . . 76
5.3.4 Histogram representation. . . . 76
5.4 The method . . . 77
5.5 Analysis of optical spectra: $HgBa_2CuO_{4+\delta}$ . . . 78
5.6 $Bi_2Sr_2CuO_{6+\delta}$: comparison between ARPES and optics. . . . 81
5.7 Temperature dependence in the strong coupling formalism. . . . 86

5.8 Summary 88

6 Temperature dependence of the single band sum rule. 89

6.1 Introduction 89
6.2 Kinetic energy and cut off effects on the optical sum rule 89
6.3 Einstein phonons 90
6.4 Gapped MFL and MMP models 92
6.5 The superconducting state 95

7 A minimal model of high temperature superconductivity. 99

7.1 Introduction 99
7.2 Electron-boson coupling in other cuprates 99
7.3 Comparison with other optical experiments. 104
7.4 Other inversion methods. 105
7.5 Discussion 111
7.6 Conclusion 114

Chapter 1

Introduction

1.1 The road to high temperature superconductivity.

The discovery of superconductivity in Hg by Kamerlingh-Onnes in 1911 can be seen as the beginning of the golden age of modern condensed matter physics. The quest to understand this phenomenon drove the invention of new theoretical tools, experimental techniques and materials. The influence of these discoveries ranges from the abstract understanding of the mass generation of elementary particles to the applied use of superconducting magnet technology in the newly build LHC. Incidentally, one of the hopes is that the same technology may prove that the mass generation process is actually responsible for the mass of the W$\pm$ and Z bosons that carry the weak interaction. Bardeen, Cooper and Schrieffer put forward a solution of the superconductivity problem in 1957 [1, 2]. They showed that the electrons could overcome their repulsive interaction due to the interaction with phonon degrees of freedom. The predictions of their theory have largely been proven correct. However, their theory predicted a certain degree of universality. For example, the ratio of the gap, Δ, to the critical temperature, T_c was predicted to be $2\Delta/k_bT_c = 3.52$. This ratio was indeed observed in some materials, like Sn, but not for others, like Pb. In the last case this ratio was significantly larger: $2\Delta/k_bT_c \approx 4.38$. The understanding of this non-universality came from Migdal-Eliashberg-Nambu (strong coupling) theory [3, 4, 5]. This theory can be seen as a quantitative theory of superconductivity arising from the electron-phonon interaction. The contribution by Migdal was to derive a theory for the electron-phonon interaction in normal metals, while Eliashberg and Nambu extended this theory into the superconducting state. At the same time Giaever [6] proved one of the predictions of BCS theory correct. He showed that the current-voltage characteristic of a normal to superconducting tunnel junction gave direct evidence of the density of states predicted by the BCS theory. In fig. 1.1 we reproduce the result obtained in ref. [7] They noted deviations from the density of states predicted by BCS, but did not realize their origin (see caption of fig. 1.1). The understanding of the origin of these little bumps turned out to be

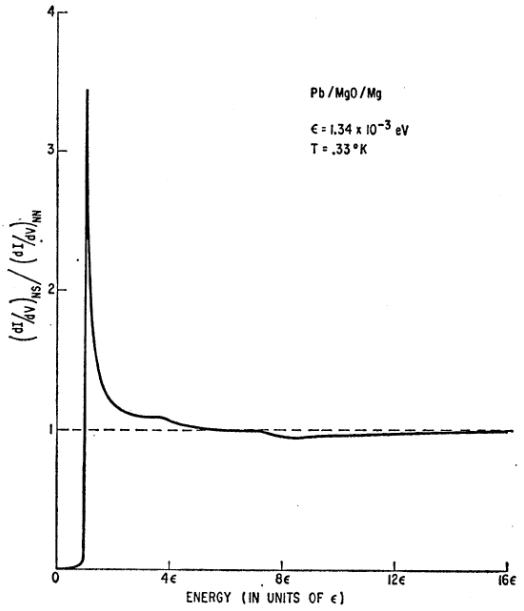

Figure 1.1: Relative tunneling conductance of a Pb-Mgo-Mg sandwich plotted against energy. At higher energy there are definite divergences from the BCS density of states as can be seen from the bumps in the experimental curve. Note that the crossover point occurs at the Debeye temperature. Figure and caption adapted from ref. [7]

conclusive evidence in favor of the electron-phonon mechanism for superconductivity [8, 9]. With a working theory in hand it became possible to think about the limitations on the critical temperature. In the 60's and 70's much effort was put in determining whether there existed an upper limit on the critical temperature. An anecdotal account of the work carried out at the Lebedev institute in the group of V.L Ginzburg at that time is given by I. Mazin [10]. Ginzburg's main interest was to find mechanisms other than the electron-phonon interaction, and hopefully to enhance the critical temperature to room temperature. Even though the argument, leading to an upper limit on the critical temperature of about 40 K by Cohen and Anderson [11], was proven to be incorrect by Kirzhnits [12], hopes of achieving room temperature superconductivity where diminishing, since the highest critical temperature observed was no higher than $T_c \approx 22$ K in the A-15 superconductor $NbGe_3$. In 1986 Bednorz and Muller reported superconductivity in $Ba_xLa_{5x}Cu_5O_{5(3y)}$ with a critical temperature above 30 K [13]. This was already a substantial improvement and it took only one year before superconductivity was found in $YBa_2Cu_3O_7$ with an onset temperature $T_c \approx 93$ K [14]. This discovery enabled applications of superconductivity at temperatures that could be reached using liquid nitrogen as coolant. Currently the highest critical temperature observed is $T_c = 163$ K for $HgBa_2Ca_2Cu_3O_{8+\delta}$ under pressure [15].

The literature build up in more then 20 years of research is extensive. Many excellent reviews have been written on equally many aspects of these compounds. Consequently, I can highlight only a few aspects in this introduction. I will do this based on a simplified phase diagram that reflects the features

believed to be universal to all cuprates . Several reviews that form the basis of this discussion are given in Ref.'s [16, 17, 18, 19, 20, 21, 22, 23, 24, 25].

1.2 From Mott insulator to Fermi liquid

The cuprate high temperature superconductors form a class of structurally complicated compounds. Conducting layers of CuO_2 are interspersed with insulating "rocksalt" layers (also known as block layers). Two examples of crystal structures are shown in fig.'s 3.1 and 4.1. The undoped materials turn out to be insulating even though band structure calculations predict them to be metallic [16]. The electronic configuration of Cu^{2+} is such that there is a single electron in the $d_{x^2-y^2}$ orbital that makes up the only band crossing the Fermi energy. This fact allows us to make an oversimplified picture of the electronic structure of the CuO_2 plane. In figure 1.2 the Cu atoms are indicated in blue. The oxygen atoms are not shown, but each bond between the Cu atoms represents one O atom. Also indicated is

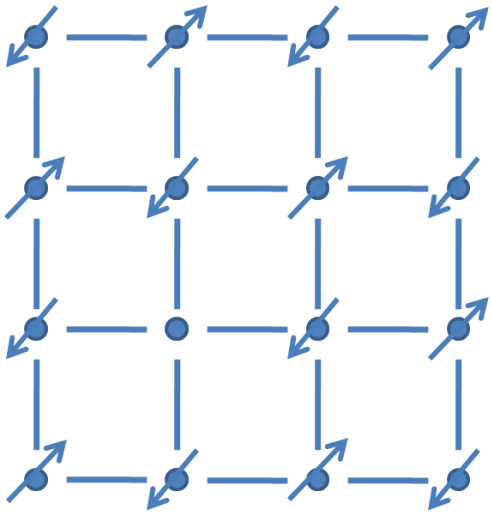

Figure 1.2: Schematic of the CuO_2 plane. Each blue ball represents a Cu atom while each bond represents one O atom. Arrows indicate the spin orientation of the electron on each site.

the spin state of the electron on each site. The electrons strongly repel each other through the Coulomb interaction U. However, there is a finite overlap between the states on two neighboring copper atoms creating a hopping matrix element t. The properties of the groundstate depends on the ratio of t to U. If $U \gg t$ the result is that, at half filling (i.e. exactly one electron per site), the electrons are localized with one electron per site. Some kinetic energy can be regained by anti-parallel alignment of the spins on neighboring sites. This situation can be described by a Hamiltonian known as the Hubbard model,

$$H = -t \sum_{<i,j>,\sigma} (c^{\dagger}_{i,\sigma} c_{j,\sigma} + h.c.) \quad + \quad U \sum_{i} n_{i,\uparrow}, n_{i,\downarrow} \tag{1.1}$$

In the case of $U \gg t$ this reduces to the so-called t-J model,

$$H = -t \sum_{<i,j>,\sigma} (c^{\dagger}_{i,\sigma} c_{j,\sigma} + h.c.) \quad + \quad J \sum_{<i,j>} (\mathbf{S}_i \cdot \mathbf{S}_j - \frac{1}{4} n_i n_j) \tag{1.2}$$

where $J = 4t^2/U$ is known as the exchange constant. The on-site repulsion U is estimated to be of the order $U \approx 8$ eV, but one experimentally observes only a gap of about 2 eV. The difference is thought to arise form the fact that the Cu $d_{x^2-y^2}$ orbitals are hybridized with the oxygen $p_{x,y}$ orbitals. In this case one can show that the gap is not determined by the on-site repulsion U but by the charge transfer energy $\Delta = \varepsilon_p - \varepsilon_d$ [26], which is of the order 2 eV.

So far we have considered the case where there resides exactly one electron per site. The simplest way to add or remove electrons from the CuO_2 plane is by changing the oxygen content. This can be done by annealing crystals at high temperature in an oxygen rich or oxygen deficient atmosphere. Another method is to partially substitute elements in the block layers with elements that have a different valency. This leads to electron doped or hole doped cuprates. Doping leads to the schematic phase diagram indicated in figure 1.3. From fig. 1.2 it is immediately clear that adding or removing electrons destroys the insulating state. For example, in the case of electron removal, the hole that is left behind can easily move around. The phase diagram shown in fig. 1.3 includes only the phases that seem to be

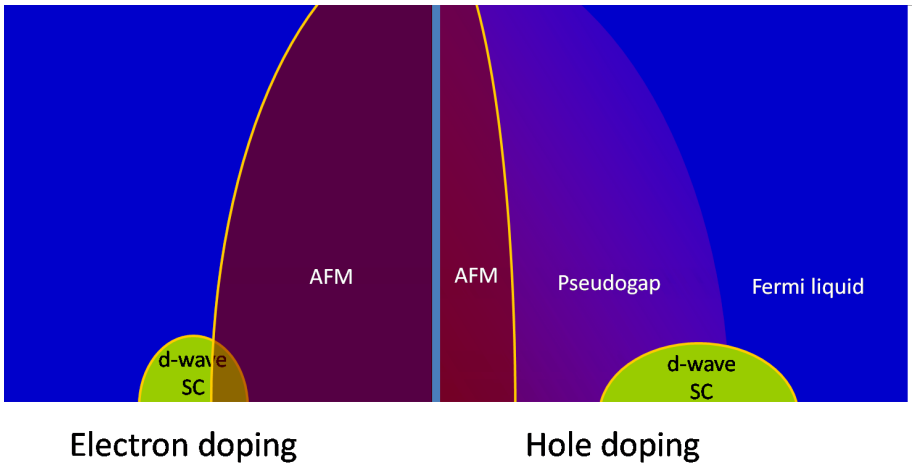

Figure 1.3: Schematic phase diagram for electron doped (left) and hole doped (right) cuprates.

universal to all families. We first confine our attention to the zero temperature phase diagram. At low doping the system still has anti-ferromagnetic correlations. There are debates going on about the nature of this state. One proposal is that this state is a realization of the resonating valence bond (RVB) state proposed by Anderson [27]. Others have argued that doping the Mott insulator destroys the strongly correlated state, but anti-ferromagnetic order survives. It is easy to see from figure 1.2 that a moving hole disrupts the anti-ferromagnetic background. Exchanging a hole and a spin on adjacent sites, one

sees that on its new site this spin breaks the anti-parallel arrangement with neighboring spins. So, with increasing hole doping the anti-ferromagnetic correlations are suppressed and the anti-ferromagnetic state eventually gives way to the superconducting state, with a $d-wave$ symmetry of the superconducting gap around the Fermi surface. This state persist until one has added about 0.3 holes per Cu atom, or 30 $\%$ doping. For even higher dopings it is believed that the groundstate is a conventional Fermi liquid. The picture on the electron doped side is somewhat different with anti-ferromagnetism persisting to higher dopings. The superconducting state that eventually emerges seems to be closely linked to the antiferromagnetism and the dome is much narrower. The critical temperatures observed are also lower. This particle-hole asymmetry is another aspect that is not completely understood. For finite temperature one finds that the Néel temperature at half filling is of the order of 400 K. With increasing doping the Néel temperature decreases, and the anti-ferromagnetic state is replaced by a state known as the pseudogap state. Many suggestions for the nature of this state have been put forward. One idea is that below the pseudogap temperature, known as T*, pair forming correlations start to appear. At lower temperatures these "precursor" Cooper pairs, condense and a phase coherent, superconducting state is formed. In this case the ransition would be of the Bose-Einstein condensation type. Other ideas include the formation of a new state of matter. The problem with this last proposal is the fact that the T* line appears to be a crossover temperature rather than an actual phase transition. Recently, some evidence was reported that at T* a novel form of magnetic order sets in [28]. The form of ordering observed by these authors breaks time reversal symmetry while preserving translational symmetry. These observations are consistent with two recent theoretical proposals [29, 30, 31]. With increasing doping the pseudogap temperature decreases. Recently, Hufner *et al.* collected results from several experimental probes [32]; their compilation is reproduced in figure 1.4. The experiments give evidence for two distinct energy scales. The highest one is related to the pseudogap phenomenon. This compilation suggests that the pseudogap phenomenon disappears only at high doping where the superconducting state disappears. They observe that the pseudo-gap observed by ARPES is only half the size of the one measured by STM and Raman scattering. This suggest that this energy scale is related to a pairing gap. The peculiarities of the pseudogap state are then those of a phase fluctuating superconductor [33, 34]. The other energy scale can be associated with the condensation energy. This picture supports the idea that the superconducting transition changes from the BEC to the BCS type with increasing doping.

Strongly overdoped samples conform to a more standard Fermi liquid picture. The Fermi surface is sharp with well defined quasi particles. Together with the above observation of a crossover to standard BCS behavior, this suggests that overdoped samples are described by an extension of strong coupling theory, modified to support the $d-wave$ symmetry of the order parameter. In this thesis I will use this formalism to analyze properties of the normal state. The samples that will be analyzed range from

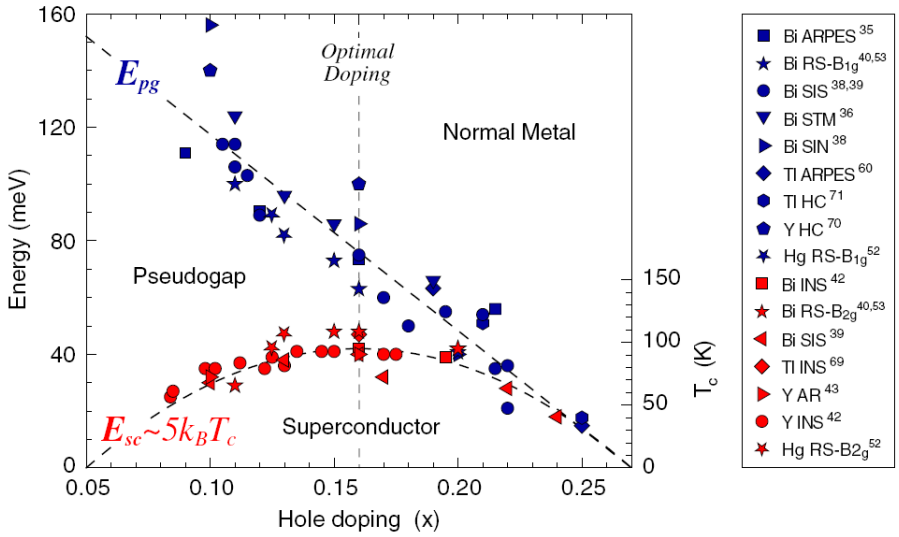

Figure 1.4: Pseudogap energy scale determined by $E_{pg} = 2\Delta_{pg}$ from several experimental probes: angle-resolved photoemission spectroscopy (ARPES), tunneling (STM, SIN, SIS), Andreev reflection (AR), Raman scattering (RS) and heat conductivity (HC). The critical temperature determines the second energy scale as $E_{sc} \approx 5\mathrm{k}_b\mathrm{T}_c$ Also included are inelastic neutron scattering (INS) results for Ω_r, the magnetic resonance mode energy. Figure adapted from [32]

strongly underdoped to strongly overdoped. With decreasing doping the interaction strength strongly increases and this will eventually result in a breakdown of the Fermi liquid picture. We find some evidence that for underdoped samples the formalism indeed needs to be extended. However, the recent observation of quantum oscillations in strongly underdoped $YBa_2Cu_3O_{6.5}$, indicating the presence of a coherent Fermi surface, suggest that even in strongly underdoped compounds a remnant of the Fermi liquid state survives.

1.3 Correlations and superconductivity

One can separate the field into two schools of thought regarding the nature of the superconducting state. The first school beliefs that superconductivity in the cuprates arises from strong correlation effects. This is borne out most clearly by the work of Anderson and collaborators [27, 35, 36]. Roughly, the idea is that, when doped, the Mott insulator gives way to the RVB liquid. In such a liquid electrons are paired into singlet states. The electrons close to the Fermi energy reside in the anti-bonding band made up out of the Cu orbitals with $x^2 - y^2$ symmetry. This results in pair wave functions with a node at the origin: two electrons making up a pair never come very close, avoiding the repulsive core of the Coulomb potential. The pairing into this singlet state is then governed by the superexchange interaction $J \sim 150$ meV. This energy scale is very large, and could explain why T_c is high. Unfortunately, neither

the Hubbard nor the $t-J$ model are easily solvable. As a result it is not clear that in these models the ground state can be superconducting in any parameter range. One method to study the occurrence of superconductivity in these models is through a variational approach. In this approach one starts from a trial wave function with a few parameters that can are optimized so as to minimize the expectation value of the ground state energy. An example of such a trial wave function is [37],

$$|\Psi\rangle = e^{h\hat{K}/t}e^{-g\hat{D}}|\Psi_0\rangle \tag{1.3}$$

The two operators $\hat{K}$ and $\hat{D}$ are the first and second term of Eq. 1.1 respectively. h and g are two parameters that are to be determined variationally. The wave function with $h = 0$ is known as a Gutzwiller wave function. The state $|\Psi_0\rangle$ can be the BCS wave function, an anti-ferromagnetic state or just the Fermi sea. The effect of applying the right hand operator to this state is to completely project out all doubly occupied sites, while the effect of the other operator is to restore some kinetic energy. Eichenberger and Baeriswyl recently showed that at half filling the anti-ferromagnetic state has a lower energy while at higher dopings the superconducting state wins [37].

The second approach to understanding superconductivity in the cuprates uses an extension of the strong coupling theory already mentioned. In normal metals two electrons interact with each other through the Coulomb interaction and by exchanging phonons. In the simplest picture this is just a superposition of terms [38, 39],

$$V_{eff}(q,\omega) = \tilde{V}_c(q,\omega) + \tilde{V}_{e-ph}(q,\omega) + \tilde{V}_{e-sf}(q,\omega) \tag{1.4}$$

Here $\tilde{V}_c$ is the screened Coulomb interaction, $\tilde{V}_{e-ph}$ is the screened electron-phonon interaction and $\tilde{V}_{e-sf}$ is the interaction between electrons and paramagnons. However, if the interactions are strong the electron-electron vertex can depend in a non-linear way on these couplings. The interactions are screened due to the presence of the other electrons. The screened Coulomb interaction is strictly positive if the dielectric function is larger then zero. The second term however is negative for frequencies $\omega \lesssim \omega_q$, with ω_q a typical phonon frequencies. This negative part can become larger then the repulsive Coulomb part and bind two electrons in a pair. The BCS theory simplifies this effective interaction by replacing it with a constant attractive interaction for frequencies smaller then the Debeye frequency and zero above. This is a reasonable approximation if the electron-phonon interaction is weak. The Eliashberg theory includes the frequency dependence of the interaction and is valid for both small and large coupling constants (at least up to $\lambda \approx 3$. There are no conventional electron-phonon superconductors with a larger coupling constant).

The BCS theory leads to the gap equation,

$$\Delta_k = -\sum_{k'} \frac{V_{k,k'}\Delta_{k'}}{2E_{k'}} tanh\left(\frac{\beta E_{k'}}{2}\right) \tag{1.5}$$

Where Δ_k is the energy gap, $V_{k,k'}$ is the effective inter electron interaction, $\beta = (k_B T)^{-1}$ and $E_k = \sqrt{\varepsilon_k^2 + \Delta_k^2}$. In BCS theory the electron-phonon interaction and Fermi surface are assumed to be isotropic. This favors $s-wave$ pairing: the gap is also isotropic. In this case, the solution to Eq. 1.5 requires that the effective interaction is negative. The observation of a $d-wave$ gap in the cuprates is difficult to understand in the above picture. There is however a second possibility to solve the gap equation, first put forward by Scalapino *et al.* [39]. These authors leave out the electron-phonon interaction, but take into account an effective interaction mediated by the exchange of paramagnons (third term in Eq. 1.4). This interaction is repulsive everywhere but strongly peaked at a momentum transfer of $Q = (\pi, \pi)$. Figure 1.5 shows the scattering process. This interaction scatters two electrons from

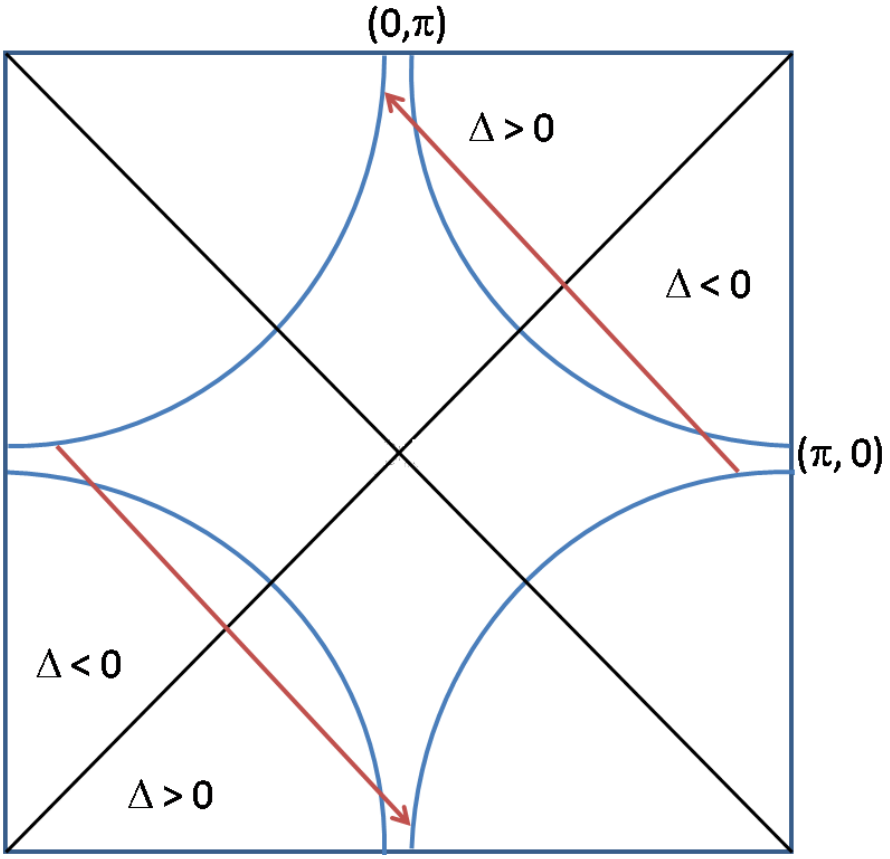

Figure 1.5: In the paramagnon theory of Scalapino *et al.* two electrons with opposite momentum states are scattered to states on opposite sides of the Fermi surface that differ with the initial state by (π, π), indicated by the red arrows.

opposite sides of the Fermi surface. This scattering is most effective near the anti-nodal regions around $(0, \pi)$ and $(\pi, 0)$. Looking at Eq. 1.5 one realizes that a possible solution for positive $V_{k,k'}$ is given by $\Delta_k = \Delta_0(\cos k_x - \cos k_y)$. It is interesting to note that the publication of this idea coincided with the publication of the discovery of the high temperature superconductors and that it predicted the

possibility of a $d-wave$ gap. It took several years before it was experimentally realized that the gap symmetry was indeed $d-wave$. It took even longer before convincing evidence was given [40].

In this thesis I will present the latest experimental results obtained from optical spectroscopy. I will first discuss some optical properties of solids. This will be used as introduction to the experimental part of this work. In chapters 3 and 4 I present the experimental results. In chapter 5 I will discuss how one can analyze optical properties in the strong coupling formalism. Chapter 6 describes how this formalism can be used to explain the anomalous behavior of the optical sum rule that has been reported in earlier studies. Finally in chapter 7 I will present a minimal model that explains a large body of experimental facts, including the high critical temperature of these materials.

Chapter 2

Theory of Optical Spectroscopy

2.1 Introduction

In this chapter I will discuss some of the basic physics of correlated electron systems from an optical spectroscopists viewpoint. The interaction of light and matter will be discussed first from a classical point of view, based on the Maxwell equations. This will be the basis for a discussion of the optical techniques that are used in the experiments described in this work. I will then continue with a discussion of the quantum mechanical description of the interaction between light and matter, using the Kubo-formalism. Finally, I will discuss the application of sum rules to correlated systems and what happens when interactions, like the electron-phonon interaction, become important. The first part of the review is not meant to be complete. Readers with interest for further details are referred to references [41] and [42]. In the following all fields, currents, charge densities etc. are implied to be position and time dependent if not written explicitly. Bold quantities imply vectors or matrices. A large part of this chapter is based on the lecture notes I wrote for the course given by Dirk van der Marel at the *XIth Training Course in the Physics of Strongly Correlated Systems* in Vietri sul Mare. It has been published in the proceedings of the school [43] and is available also from the arXiv [44].

2.2 Electromagnetism and Matter

2.2.1 Maxwell's equations

We start this review with the microscopic Maxwell equations,

$$\nabla \cdot \mathbf{e} = 4\pi\rho_{micro}, \tag{2.1}$$
$$\nabla \times \mathbf{e} = -\frac{1}{c}\frac{\partial}{\partial t}\mathbf{b}, \tag{2.2}$$
$$\nabla \cdot \mathbf{b} = 0, \tag{2.3}$$
$$\nabla \times \mathbf{b} = \frac{1}{c}\frac{\partial}{\partial t}\mathbf{e} + \frac{4\pi}{c}\mathbf{j}_{micro}. \tag{2.4}$$

Here **e** and **b** are the microscopic electric and magnetic fields respectively. ρ_{micro} is the total microscopic charge distribution and j_{micro} the total microscopic current distribution (i.e. due to internal and external sources). Note that these equations are written in the C.G.S. system of units. To convert them to S.I. units, simply replace 4π by $1/\varepsilon_0$. The charge distribution for a collection of point sources with charge q_i can be written classically,

$$\rho_{micro} = \sum_i q_i \delta(\mathbf{r} - \mathbf{r_i}), \tag{2.5}$$

or quantum mechanically as,

$$\rho_{micro} = -e\Psi^*(\mathbf{r})\Psi(\mathbf{r}). \tag{2.6}$$

Equations (2.1-2.4) are not very practical to work with. As a first step we rewrite them in a more familiar form. To do this we average the fields, charge and current distributions over a volume ΔV,

$$\rho_{total}(\mathbf{r}) = \frac{1}{\Delta V}\int_{\Delta V} \rho_{micro}(\mathbf{r}+\mathbf{r}')d^3\mathbf{r}', \tag{2.7}$$
$$\mathbf{J}_{total}(\mathbf{r}) = \frac{1}{\Delta V}\int_{\Delta V} \mathbf{J}_{micro}(\mathbf{r}+\mathbf{r}')d^3\mathbf{r}', \tag{2.8}$$

and similarly for **e** and **b**. This is a sensible procedure under the condition that $a_0 \ll \Delta V \ll (2\pi c/\omega)^3$ where a_0 is the Bohr radius. Using these averaged distributions we arrive at the standard Maxwell equations in free space,

$$\nabla \cdot \mathbf{E}_{total}(\mathbf{r},t) = 4\pi\rho_{total}(\mathbf{r},t), \tag{2.9}$$
$$\nabla \times \mathbf{E}_{total}(\mathbf{r},t) = -\frac{1}{c}\frac{\partial}{\partial t}\mathbf{B}_{total}(\mathbf{r},t), \tag{2.10}$$
$$\nabla \cdot \mathbf{B}_{total}(\mathbf{r},t) = 0, \tag{2.11}$$
$$\nabla \times \mathbf{B}_{total}(\mathbf{r},t) = \frac{1}{c}\frac{\partial}{\partial t}\mathbf{E}_{total}(\mathbf{r},t) + \frac{4\pi}{c}\mathbf{J}_{total}(\mathbf{r},t). \tag{2.12}$$

In order to see how matter interacts with propagating electromagnetic waves we have to distinguish between induced and external sources. We write $\mathbf{J}_{total} \equiv \mathbf{J}_{ext} + \mathbf{J}_{ind}$ and $\rho_{total} \equiv \rho_{ext} + \rho_{ind}$. Both the induced and external charge and current distributions have to obey the continuity equations separately,

$$\nabla \cdot \mathbf{J}_{ind/ext} + \frac{\partial}{\partial t}\rho_{ind/ext} = 0. \tag{2.13}$$

We can distinguish three different types of macroscopic internal sources,

$$\mathbf{J}_{ind} = \mathbf{J}_{cond} + \frac{\partial \mathbf{P}}{\partial t} + c\nabla \times \mathbf{M}. \tag{2.14}$$

The first term on the right hand side, $\mathbf{J}_{cond}$, corresponds to the response of the free charges. The second term is the current due to changes in the polarization state of the system. Finally, we include a term representing a current due to magnetization. Note that this last term is purely transversal (the divergence of a rotation is always zero) and so is easy to distinguish from the other two terms. It is convenient to introduce new fields

$$\mathbf{D}(\mathbf{r}, t) \equiv \mathbf{E}_{ext}(\mathbf{r}, t) \equiv \mathbf{E}(\mathbf{r}, t) + 4\pi\mathbf{P}(\mathbf{r}, t), \tag{2.15}$$

$$\mathbf{H}(\mathbf{r}, t) \equiv \mathbf{B}(\mathbf{r}, t) - 4\pi\mathbf{M}(\mathbf{r}, t), \tag{2.16}$$

so that using equations (2.14-2.16) in equations (2.9) and (2.12) we find,

$$\nabla \cdot \mathbf{D}(\mathbf{r}, t) = 4\pi\rho_{ext}(\mathbf{r}, t), \tag{2.17}$$

$$\nabla \times \mathbf{H}(\mathbf{r}, t) = \frac{1}{c}\frac{\partial}{\partial t}\mathbf{D}(\mathbf{r}, t) + \frac{4\pi}{c}\mathbf{J}_{ext}(\mathbf{r}, t) + \frac{4\pi}{c}\mathbf{J}_{cond}(\mathbf{r}, t). \tag{2.18}$$

2.2.2 Linear Response Theory

In the spirit of linear response theory we assume that the response of polarization, magnetization or current are linear in the applied fields:

$$\mathbf{P} = \chi_e \mathbf{E}, \tag{2.19}$$

$$\mathbf{M} = \chi_m \mathbf{H}, \tag{2.20}$$

$$\mathbf{J} = \sigma \mathbf{E}. \tag{2.21}$$

The electric and magnetic susceptibilities can be expressed in terms of a dielectric function $\varepsilon' = 1 + 4\pi\chi_e$ and magnetic permittivity $\mu' = 1 + 4\pi\chi_m$. The dielectric function is a response function that connects the external field $\mathbf{E}_{ext}$ at position $\mathbf{r}$ and time t with the field $\mathbf{E}$ at all other times and positions. So in general,

$$\mathbf{E}_{ext}(\mathbf{r}, t) = \int_{-\infty}^{t} \int \varepsilon'(\mathbf{r}, \mathbf{r}', t, t')\mathbf{E}(\mathbf{r}', t')d^3r'dt'. \tag{2.22}$$

We will be mainly interested in the Fourier transform of $\varepsilon' \equiv \varepsilon(\mathbf{q},\omega)$ however. It is an easy exercise to express the Maxwell equations in terms of $\mathbf{q}$ and ω which we leave to the reader. We can use these definitions to once again rewrite the Maxwell equations in the following form,

$$\begin{aligned}
\nabla \cdot (\varepsilon' \mathbf{E}) &= 4\pi\rho_{ext}, && (2.23)\\
\nabla \times \mathbf{E} &= -\frac{1}{c}\frac{\partial}{\partial t}(\mu')\mathbf{H}, && (2.24)\\
\nabla \cdot \mu' \mathbf{H} &= 0, && (2.25)\\
\nabla \times \mathbf{H} &= \frac{1}{c}\frac{\partial}{\partial t}(\varepsilon' \mathbf{E}) + \frac{4\pi\sigma}{c}\mathbf{E}. && (2.26)
\end{aligned}$$

We are now in a position to study the response of a solid to an externally applied field or light wave. For simplicity we assume that our solid is homogeneous so that $\nabla\varepsilon' = 0$ and $\nabla\mu' = 0$. We can describe light waves by plane waves, i.e.

$$\mathbf{E}(\mathbf{r},t) = \mathbf{E_0} e^{i(\mathbf{q}\cdot\mathbf{r}-\omega t)}, \quad (2.27)$$

$$\mathbf{B}(\mathbf{r},t) = \mathbf{B_0} e^{i(\mathbf{q}\cdot\mathbf{r}-\omega t)}. \quad (2.28)$$

Using (2.28) on the right hand side of Faraday's equation (2.10) and rearranging we find,

$$\mathbf{B} = \frac{c}{i\omega}\nabla \times \mathbf{E}. \quad (2.29)$$

If we now take the curl of this equation and use the fact that we can express $\mathbf{M}$ in terms of $\mathbf{B}$ as (see equations (2.16) and (2.20)),

$$\mathbf{M} = \frac{\mu'^{-1} - 1}{4\pi}\mathbf{B}. \quad (2.30)$$

we find that

$$\begin{aligned}
\nabla \times \mathbf{M} &= \frac{\mu'^{-1} - 1}{4\pi}\nabla \times \mathbf{B} = \frac{c}{i\omega}\frac{\mu'^{-1} - 1}{4\pi}\nabla \times \nabla \times \mathbf{E}\\
&= \frac{c}{i\omega}\frac{\mu'^{-1} - 1}{4\pi}(\nabla^2\mathbf{E} - \nabla(\nabla \cdot \mathbf{E}) = \frac{cq^2}{i\omega}\frac{\mu'^{-1} - 1}{4\pi}\mathbf{E}^T. && (2.31)
\end{aligned}$$

Note that in this equation we are left with only the transversal field since the curl of a curl is transverse. We give two further identities for completeness,

$$\frac{\partial \mathbf{P}}{\partial t} = -i\omega\frac{1-\varepsilon'}{4\pi}\mathbf{E}, \quad (2.32)$$

and,

$$J_{cond} = \sigma\mathbf{E}. \quad (2.33)$$

Finally, we note that inside the solid $\rho_{ext} = J_{ext} = 0$. With this we have all the ingredients to express equation (2.18) in terms of $\mathbf{E}$ and $\mathbf{J}$. We split this equation in transversal and longitudinal parts to find,

$$\begin{aligned}
\frac{\mathbf{J}^T_{ind}(\mathbf{q},\omega)}{\mathbf{E}^T(\mathbf{q},\omega)} &\equiv \frac{i\omega}{4\pi}\{1 - \varepsilon'(\mathbf{q},\omega) - \frac{i4\pi}{\omega}\sigma(\mathbf{q},\omega) - \frac{c^2q^2}{\omega^2}(1 - \frac{1}{\mu(\mathbf{q},\omega)})\}, && (2.34)\\
\frac{\mathbf{J}^L_{ind}(\mathbf{q},\omega)}{\mathbf{E}^L(\mathbf{q},\omega)} &\equiv \frac{i\omega}{4\pi}\{1 - \varepsilon'(\mathbf{q},\omega) - \frac{i4\pi}{\omega}\sigma(\mathbf{q},\omega)\}. && (2.35)
\end{aligned}$$

We can define a new dielectric function with longitudinal and transverse components and write the previous equation in a more compact form,

$$\frac{\mathbf{J}_{ind}^{L,T}(\mathbf{q},\omega)}{\mathbf{E}^{L,T}(\mathbf{q},\omega)} \equiv \frac{i\omega}{4\pi}\{1-\varepsilon^{L,T}(\mathbf{q},\omega)\}. \tag{2.36}$$

This new dielectric function ε is now a complex quantity: $\varepsilon \equiv \varepsilon' + i\varepsilon'' = \varepsilon' + i4\pi\sigma/\omega$. Using the last relation we can also define a complex conductivity $\hat{\sigma} \equiv \sigma' + i\sigma''$ and it is related to the dielectric function by,

$$\hat{\sigma} = \frac{i\omega}{4\pi}(1-\varepsilon). \tag{2.37}$$

The real part of ε is often called the reactive part and the imaginary part the dissipative part. The real and imaginary parts are also indicated with a subscript 1 and 2 instead of (') and (").

2.2.3 Kramers-Kronig relations

A fundamental principle in physics is the principle of causality: an effect cannot precede its cause. This principle provides us with a very useful relation between the real and imaginary parts of a response function like the optical conductivity as we now show. First we express the induced current due to an electric field in terms of a memory function,

$$j(t) = \int_{-\infty}^{t} M(t-t')E(t')dt'. \tag{2.38}$$

The memory function has the property that $M(\tau < 0) = 0$. This is simply a restatement of the causality principle: we switch on a driving force at time $\tau = 0$ so before that time there can be no current. We define the Fourier transform of M in equation (2.38) as,

$$\hat{\sigma}(\omega) = \int_{0}^{\infty} M(\tau)e^{i\omega\tau}d\tau. \tag{2.39}$$

To do the integral we change to the complex frequency plane, $\omega \to z = \omega_1 + i\omega_2$. The exponential in Eq. (2.39) now splits in a complex and real part,

$$\hat{\sigma}(\omega) = \int_{0}^{\infty} M(\tau)e^{i\omega_1\tau}e^{-\omega_2\tau}d\tau. \tag{2.40}$$

The second exponent in this integral is bounded in the upper half plane for $\tau > 0$ and in the lower half plane for $\tau < 0$, so that we can evaluate the integral in the upper half plane since $M(\tau < 0) = 0$. We use the contour shown in figure 2.1. Since all poles occur on the real axis, the complete contour is zero,

$$\oint dz \frac{\hat{\sigma}(z)}{z-\omega} = 0. \tag{2.41}$$

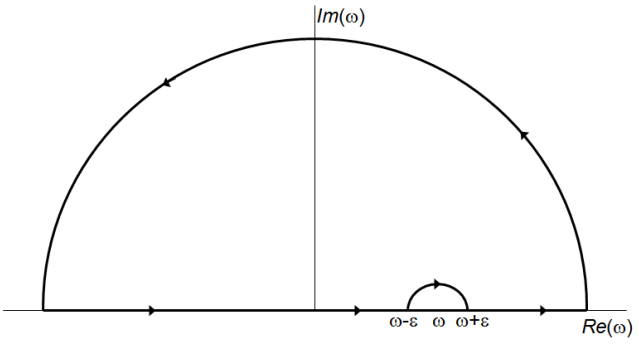

Figure 2.1: Contour used to derive the KK-relations.

The integral along the large semi circle is also zero. So we are left with,

$$\int_{-\infty}^{\omega-\varepsilon} dz \frac{\hat{\sigma}(z)}{z-\omega} + \int_{\omega+\varepsilon}^{\infty} dz \frac{\hat{\sigma}(z)}{z-\omega} + \int_{\pi}^{0} d(\omega+\epsilon e^{i\phi}) \frac{\hat{\sigma}(\omega+\epsilon e^{i\phi})}{\epsilon e^{i\phi}} = 0. \tag{2.42}$$

The first two integrals give the principle value of the integral for $\epsilon \to 0$,

$$\mathcal{P} \int_{-\infty}^{\infty} d\omega' \frac{\hat{\sigma}(\omega')}{\omega'-\omega} - \pi i \hat{\sigma}(\omega') = 0. \tag{2.43}$$

From which the Kramers-Kronig relations follow,

$$\sigma_1(\omega) = \frac{1}{\pi}\mathcal{P} \int_{-\infty}^{\infty} \frac{\sigma_2(\omega')}{\omega'-\omega} d\omega', \tag{2.44}$$

$$\sigma_2(\omega) = -\frac{1}{\pi}\mathcal{P} \int_{-\infty}^{\infty} \frac{\sigma_1(\omega')}{\omega'-\omega} d\omega'. \tag{2.45}$$

Using $Im(M(\tau)) = 0$ we see that $\hat{\sigma}(-\omega) = \hat{\sigma}^*(\omega)$, which implies that $\sigma_1(-\omega) = \sigma_1(\omega)$ and $\sigma_2(-\omega) = -\sigma_2(\omega)$. These relations can be used to rewrite equations (2.44) and (2.45),

$$\sigma_1(\omega) = \frac{2}{\pi}\mathcal{P} \int_{0}^{\infty} \frac{\omega'\sigma_2(\omega')}{\omega'^2-\omega^2} d\omega', \tag{2.46}$$

$$\sigma_2(\omega) = -\frac{2\omega}{\pi}\mathcal{P} \int_{0}^{\infty} \frac{\sigma_1(\omega')}{\omega'^2-\omega^2} d\omega'. \tag{2.47}$$

The relations (2.44) and (2.45) between the real and imaginary parts of the optical conductivity are examples of the general relations between real and imaginary parts of causal response functions and they are referred to as Kramers-Kronig (KK) relations.

2.2.4 Polaritons

In this section we discuss the properties of electromagnetic waves propagating through solids. Such a wave is called a polariton. A polariton is a photon dressed up with the excitations that exist inside solids. For example one can have phonon-polaritons which are photons dressed up with phonons.

Although the solutions of the Maxwell equations, i.e. the fields **E** and **B**, have the same form as before (Eq. (2.27) and (2.28)) they obey different dispersion relations as we will now see. As before we assume that $\nabla\varepsilon' = \nabla\mu' = 0$ and that $\rho_{ext} = J_{ext} = 0$. Taking the curl of Eq. (2.24) we obtain for the left-hand side,

$$\nabla \times \nabla \times \mathbf{E} = -\nabla^2 \mathbf{E}^T, \tag{2.48}$$

where the T indicates that we are left with a purely transverse field. We then use Eq. (2.26) to work out the right-hand side of Eq. (2.24) and we obtain the wave equation,

$$\nabla^2 \mathbf{E}^T = \frac{\varepsilon'\mu}{c^2}\frac{\partial^2 \mathbf{E}^T}{\partial t^2} + \frac{4\pi\sigma\mu}{c^2}\frac{\partial \mathbf{E}^T}{\partial t}. \tag{2.49}$$

From this wave equation we easily obtain the dispersion relation for polaritons travelling through a solid by substituting Eq. (2.27),

$$\mu(\mathbf{q},\omega)\{\varepsilon'(\mathbf{q},\omega) + i\frac{4\pi\sigma(\mathbf{q},\omega)}{\omega}\}\omega^2 = \mu\varepsilon^L\omega^2 = \mathbf{q}^2c^2. \tag{2.50}$$

The dispersion relation for longitudinal waves can be found by observing that for longitudinal waves $\nabla \times \mathbf{E} = 0$ and hence the dispersion relation is simply,

$$\mu(\mathbf{q},\omega)\{\varepsilon'(\mathbf{q},\omega) + i\frac{4\pi\sigma(\mathbf{q},\omega)}{\omega}\} = 0. \tag{2.51}$$

The polariton solutions to Eq. (2.50) are of the form

$$\mathbf{E}(\mathbf{r},t) = \mathbf{E_0}e^{i(\mathbf{q}.\mathbf{r}-\omega t)}, \tag{2.52}$$

with

$$|q| = \frac{\sqrt{\mu\varepsilon}\omega}{c}. \tag{2.53}$$

We now define the refractive index,

$$\hat{n}(\mathbf{q},\omega) = n + ik \equiv \sqrt{\mu\varepsilon}. \tag{2.54}$$

In all cases considered here $n > 0$ and $k > 0$. We also note that $Im(\varepsilon) \geq 0$ but it is possible to have $Re(\varepsilon) < 0$. If $k > 0$ the wave travelling through the solid gets attenuated,

$$\mathbf{E}(\mathbf{r},t) = \mathbf{E_0}e^{i\omega(nr/c-t)-r/\delta}. \tag{2.55}$$

The extinction of the wave occurs over a characteristic length scale δ called the skin depth,

$$\delta = \frac{c}{\omega k} = \frac{c}{\omega Im\sqrt{\mu\varepsilon_1 + i4\pi\mu\sigma_1/\omega}}. \tag{2.56}$$

Note that we can have $k > 0$ if $Im(\varepsilon) = 0$ and $Re(\varepsilon) < 0$ so that the wave gets attenuated even though there is no absorption. In table 2.1 we indicate some limits of the skin depth.

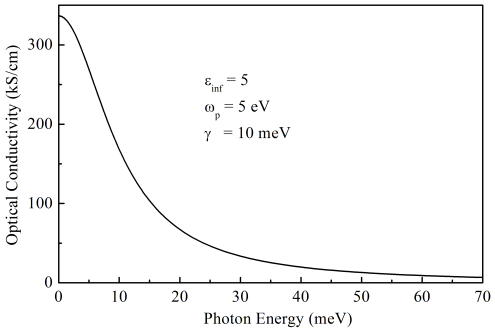

Figure 2.2: Real part of the optical conductivity for parameter values indicated in the graph. The curve is calculated using equation (2.57).

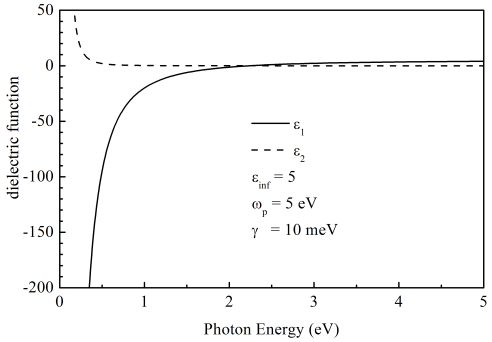

Figure 2.3: Dielectric function corresponding to equation (2.58) with the same parameters as in figure 2.2.

Insulator	$\frac{4\pi\sigma_1}{\omega} \ll \varepsilon_1$	$\delta \approx \frac{c}{2\pi\sigma_1}\sqrt{\frac{\varepsilon_1}{\mu}}$
Metal	$\frac{4\pi\sigma_1}{\omega} \gg \varepsilon_1$	$\delta \approx \frac{c}{\sqrt{2\pi\mu\sigma_1\omega}}$
Superconductor	$\frac{4\pi\sigma_1}{\omega} \ll \varepsilon_1 = -\frac{c^2}{\lambda^2\omega^2}$	$\delta \approx \frac{\lambda}{\sqrt{\mu}}$

Table 2.1: Some limiting cases of the general expression Eq. (2.56). λ in the last line is the London penetration depth.

To illustrate some of the previous results we now have a look at the simplest model of a metal: the Drude-model. The optical conductivity in the Drude model is,

$$\hat{\sigma} = \frac{ne^2}{m}\frac{1}{\tau^{-1} - i\omega}. \tag{2.57}$$

Often $1/\tau$, the time in between scattering events, is written as a scattering rate γ. The plasma frequency is defined as $\omega_p^2 \equiv 4\pi ne^2/2m$. The dielectric function can now be written as,

$$\varepsilon(\omega) = 1 + 4\pi\chi_{bound} - \frac{4\pi ne^2}{m}\frac{1}{\omega(\gamma - i\omega)} = \varepsilon_\infty - \frac{4\pi ne^2}{m}\frac{1}{\omega(\gamma - i\omega)}, \tag{2.58}$$

where for completeness we have included the contribution due to the bound charges, represented by a high energy contribution ε_∞. Figure 2.2 shows the optical conductivity given by equation (2.57) for parameter values typical of a metal. Using the same parameters we can calculate the dielectric function given by equation (2.58). The results are shown in figure 2.3. We note that the real part of the dielectric function is negative for $\omega < \omega_p/\sqrt{\varepsilon_\infty}$ and positive for $\omega > \omega_p/\sqrt{\varepsilon_\infty}$. The point where it crosses zero is called the screened plasma frequency ω_p^* (screened by interband transitions).

We can also easily calculate the optical constants,

$$\hat{n} = \sqrt{\varepsilon_\infty - \frac{\omega_p^2}{\omega\left(\omega + i\tau^{-1}\right)}}. \tag{2.59}$$

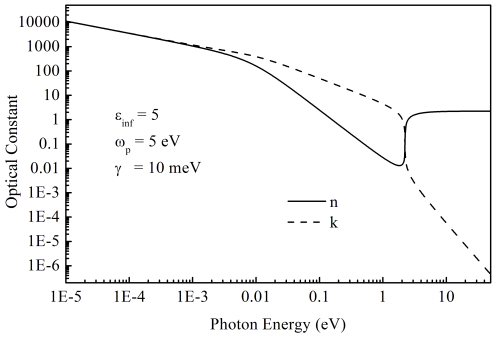

Figure 2.4: Optical constants corresponding to equation (2.58) with the same parameters as in figure 2.2.

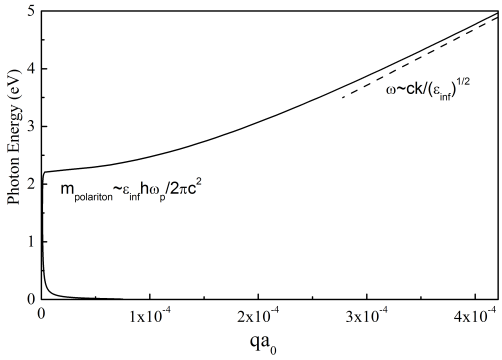

Figure 2.5: Polariton dispersion calculated with the same parameters as in figure 2.2.

The real and imaginary part are displayed in figure 2.4. We see that at the screened plasma frequency both n and k show a discontinuity.

The polariton dispersion follows from equation (2.50). Here we assume that μ = 1 and frequency independent and use Eq. (2.58) to solve (2.50) for $\omega(q)$. The polariton dispersion consists of two branches the lowest one for $0 \leq \omega \leq 1/\tau$ and one for $\omega \geq \omega_p/\sqrt{\varepsilon_\infty}$.

Finally we show the skin depth in figure 2.6. We see that for frequencies smaller than the scattering

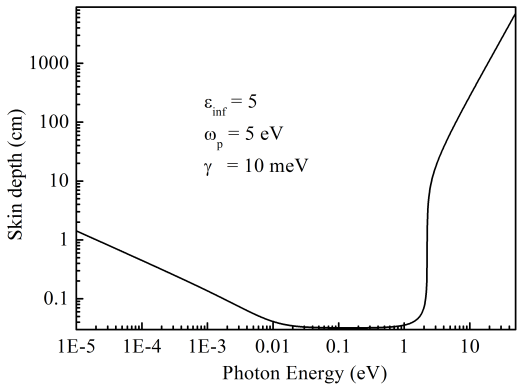

Figure 2.6: Skin depth calculated with the same parameters as in figure 2.2.

rate, γ, light waves can enter the material. This is called the classical skin effect. For frequencies larger than the screened plasma frequency the material becomes transparent again.

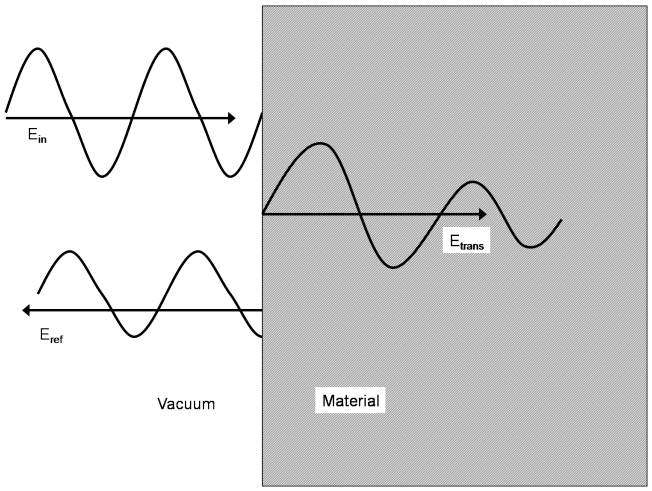

Figure 2.7: Electromagnetic waves reflecting from a material. The reflected wave has a smaller amplitude and is phase shifted with respect to the incoming wave. The transmitted wave is continuously attenuated inside the material.

2.3 Experimental Techniques

The goal of optical spectroscopy is to determine the complex dielectric function or equivalently the complex optical conductivity. Since electromagnetic waves have small momenta compared to the typical momenta of a solid, i.e. $\mathbf{q} \ll 1/a_0$, we usually only probe the $q \to 0$ limit of the optical constants. In this limit,

$$\lim_{q\to 0}(\varepsilon^T(\mathbf{q},\omega) - \varepsilon^L(\mathbf{q},\omega)) = 0, \tag{2.60}$$

$$\varepsilon(\mathbf{q}\to\mathbf{0},\omega) = \varepsilon_1(\omega) + i\frac{4\pi}{\omega}\sigma_1(\omega). \tag{2.61}$$

In some cases we can directly obtain information on both real and imaginary components separately, but more often we obtain information where the contributions are mixed. We then make use of some form the KK-relations to disentangle the two.

2.3.1 Reflection and Transmission at an interface

When we shine light on an interface between vacuum and a material, part of the light is reflected and another part is transmitted as in figure 2.7. At the boundary the electromagnetic waves have to obey the following boundary conditions,

$$\mathbf{E}_i + \mathbf{E}_r = \mathbf{E}_t, \tag{2.62}$$

$$\mathbf{E}\times\mathbf{H} \,//\, \mathbf{k}. \tag{2.63}$$

From these two equations it follows that the reflected magnetic field suffers a phase shift at the boundary,

$$\mathbf{H}_i - \mathbf{H}_r = \mathbf{H}_t. \tag{2.64}$$

Using equation (2.27) in equation (2.24) we obtain,

$$iqc\mathbf{E}^T = i\omega\mu\mathbf{H}. \tag{2.65}$$

so that, using the dispersion relation (2.50),

$$\frac{\mathbf{H}}{\mathbf{E}^T} = \sqrt{\frac{\varepsilon}{\mu}}. \tag{2.66}$$

From now on we set $\mu = 1$ unless otherwise indicated. In that case $\mathbf{H}/\mathbf{E}^T = \hat{n}$. Combining this result with Eq. (2.64) we get,

$$\mathbf{E}_i - \mathbf{E}_r = \hat{n}. \tag{2.67}$$

Together with Eq. (2.62) we can now solve for $\mathbf{E}_r/\mathbf{E}_i$ and $\mathbf{E}_t/\mathbf{E}_i$,

$$\hat{r} \equiv \mathbf{E}_r/\mathbf{E}_i = \frac{1-\hat{n}}{1+\hat{n}}, \tag{2.68}$$

$$\hat{t} \equiv \mathbf{E}_t/\mathbf{E}_i = \frac{2}{1+\hat{n}}. \tag{2.69}$$

The two quantities $\hat{r}$ and $\hat{t}$ are the complex reflectance and transmittance.

2.3.2 Reflectivity experiments

The real reflection coefficient $R(\omega)$ which is measured in a reflection experiment is related to $\hat{r}$ via

$$R = |\hat{r}|^2 = \left|\frac{(n-1)^2 + k^2}{(n+1)^2 + k^2}\right|. \tag{2.70}$$

Note that in this experiment we obtain no information on the phase of $\hat{r}$. In these experiments the angle of incidence is as close to normal incidence as possible. To measure $R(\omega)$ one first measures the reflected intensity I_s from the sample under study. To normalize this intensity one then has to take a reference measurement. This can be done by replacing the sample with a mirror (i.e a piece of aluminum or gold) and again measure the reflected intensity, I_{ref}. The reflection coefficient is then $R(\omega) \equiv I_s(\omega)/I_{ref}(\omega)$. A better way is to evaporate a layer of gold or aluminum *in-situ* and measure the reflected intensity as a reference. This way one automatically corrects for surface imperfections and, if done properly, there are no errors due to different size and shape of the reflecting surface. To obtain the optical constants from such an experiment we have to make use of KK-relations. If we define, $\hat{r}(\omega) \equiv \sqrt{R(\omega)}e^{i\theta}$, then the logarithm of $\hat{r}(\omega)$ is

$$\ln \hat{r}(\omega) = \ln \sqrt{R(\omega)} + i\theta. \tag{2.71}$$

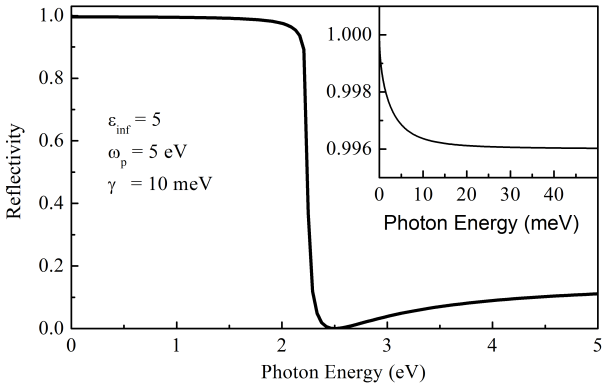

Figure 2.8: Reflectivity calculated using parameters typical for a metal. The inset shows the low energy reflectivity on an enhanced scale.

The phase θ in this expression is the unknown we want to determine. If we interpret $\hat{r}$ as a response function we can use the same arguments as in the section on KK relations and calculate $\theta(\omega)$ from,

$$\theta(\omega) = -\frac{\omega}{\pi} P \int_0^\infty \frac{\ln R(\omega')}{\omega'^2 - \omega^2} d\omega', \tag{2.72}$$

which is just the same as the KK-relation for $\hat{\epsilon}$. The complex dielectric function is calculated from $R(\omega)$ and $\theta(\omega)$ using,

$$\hat{\varepsilon}(\omega) = \left(\frac{1 - \sqrt{R(\omega)} e^{i\theta(\omega)}}{1 + \sqrt{R(\omega)} e^{i\theta(\omega)}} \right)^2. \tag{2.73}$$

Although in principle exact, this technique is in practice only approximate. The reason is that we cannot measure $R(\omega)$ from zero to infinite frequency. Most experiments probe a frequency range between a few meV and a few eV. To do the integral in Eq. (2.73) one then has to use extrapolations in the frequency ranges where no data is available. For metals the low frequency extrapolation which is most often used is the so-called Hagen-Rubens approximation,

$$R(\omega) = 1 - \alpha\sqrt{\omega}. \tag{2.74}$$

For frequencies above the interband transitions one often uses an extrapolation that is proportional to ω^{-4}. As an example of a possible experimental result we show in figure 2.8 the reflectivity calculated from the Drude model for the same parameters as in section on polaritons.

The reflectivity is close to one until just below the plasma frequency. At the zero crossing of ε_1 the reflectivity has a minimum. The inset shows a blow up of the "flat" region below 50 meV. Here one can clearly see the Hagen-Rubens behavior mentioned above. If the sample under investigation is anisotropic one has to use polarized light along one of the principle crystal axes to perform the experiment.

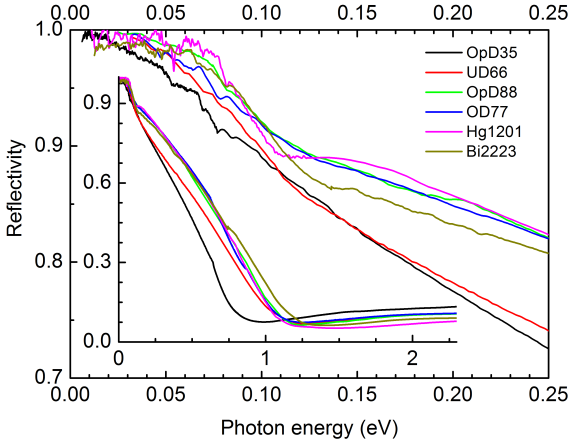

Figure 2.9: Comparison of samples at 20 K. The inset shows the reflectivity on an expanded scale. OpD35: Bi2201, see chapter 4. UD66,OpD88,OD77: Bi2212, see Ref. [45, 46]. Hg1201: see chapter 3. Bi2223: see Ref. [47].

The reflectivity of high temperature superconductors is often referred to as that of a "bad metal". This means that the reflectivity shows a clear plasma edge, but not very sharp (see inset of figure 2.9). This sharpness is determined by the scattering rate and in cuprates it is large compared to that of clean metals. As we will see in later chapters, the origin of this scattering rate is not due to impurities but to the scattering of bosonic degrees of freedom. A second feature of the reflectivity of cuprates is that at low temperature the system is superconducting and this has important consequences for the reflectivity. Figure 2.9 shows a comparison of the reflectivity for several superconductors below their critical temperature. The most interesting part for this comparison is the low frequency reflectivity. Due to the presence of a zero frequency δ-function in the conductivity and a partial gap in the electronic spectrum the reflectivity remains close to one. Above a threshold frequency, which in conventional superconductors is close to 2Δ, the reflectivity starts to decrease. The figure shows that there is a correlation between the critical temperature and the point where the reflectivity departs from one. This can be related to the increase of superfluid density and is a manifestation of the Uemura relation [48].

2.3.3 Grazing Incidence Experiments

A closely related technique is to measure reflectance under a grazing angle of incidence. Here one has to distinguish between experiments performed with different incoming polarizations as shown in figure 2.10. We distinguish between p-polarized light and s-polarized light. For p-polarization the electric field is parallel to the plane of incidence, whereas for s-polarization it is perpendicular to it (s stands for senkrecht). Since in principal the optical constants along the three crystal axes can be different, we use the labels a, b and c for the optical constants as indicated in figure 2.10. For p-polarized light the

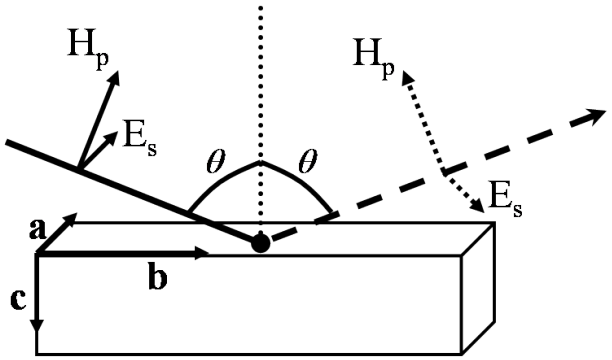

Figure 2.10: Grazing incidence experiment. The result of the experiment is extremely sensitive to the precise orientation of the crystal axes with respect to the incoming light.

complex reflectance is,

$$r_{\mathrm{p}} = \frac{\hat{n}_c\hat{n}_b\cos\theta - \sqrt{\hat{n}_c^2 - \sin^2\theta}}{\hat{n}_c\hat{n}_b\cos\theta + \sqrt{\hat{n}_c^2 - \sin^2\theta}}. \tag{2.75}$$

The angle θ in this equation is the angle relative to the surface normal under which the experiment is performed. For s-polarized light the complex reflectance is,

$$r_{\mathrm{s}} = \frac{\cos\theta - \sqrt{\hat{n}_a^2 - \sin^2\theta}}{\cos\theta + \sqrt{\hat{n}_a^2 - \sin^2\theta}}. \tag{2.76}$$

An example of such an experiment is shown in figure 2.11. In this example the samples are from the bismuth based family of cuprates. They have a layered structure consisting of conducting copper-oxygen sheets, interspersed with insulating bismuth-oxygen layers. Since the bonding between layers is not very strong it is very difficult to obtain samples that are sufficiently thick along the insulating c-direction. The grazing incidence technique is used here to probe the optical constants of the c-axis

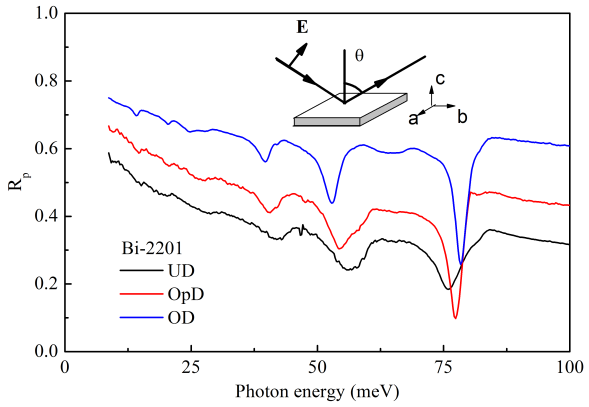

Figure 2.11: Grazing incidence reflectivity of $Bi_2Sr_2CuO_{6+\delta}$ samples for three different dopings. The inset indicates the measurement geometry. These experiments are discussed in more detail in chapter 4.

without the need of a large ac-face surface area. A disadvantage in this particular experiment is that it is not possible to determine accurately the absolute value of the optical constants. It is possible however to determine the so-called loss function $Im(-1/\hat{\varepsilon}_c)$. The experiment is performed on the ab-plane of the sample using p-polarized light and we can simplify the expression for $\hat{r}_p$ by using the fact that the a and b direction are almost isotropic. The resulting expression for $\hat{r}_p$ is,

$$\hat{r}_{\mathrm{p}} = \frac{\sqrt{\hat{\varepsilon}_b}\cos\theta - \sqrt{1-\sin^2\theta/\hat{\varepsilon}_c}}{\sqrt{\hat{\varepsilon}_b}\cos\theta + \sqrt{1-\sin^2\theta/\hat{\varepsilon}_c}}. \tag{2.77}$$

From this equation we can derive the following relation between the grazing incidence reflectivity and a pseudo loss-function $L(\omega)$ [49],

$$L(\omega) \equiv \frac{(1-R_p)}{(1+R_p)} \approx Im\frac{2e^{i\phi_p}}{|n_b|\cos\theta}\sqrt{1-\frac{\sin^2\theta}{\hat{\varepsilon}_c}}. \tag{2.78}$$

The function $\sqrt{1-\frac{\sin^2\theta}{\hat{\varepsilon}_c}}$ has maxima at the same position as the true loss-function. In chapter 5 we compare this spectrum to the bosonic spectral density density of $Bi_2Sr_2CuO_{6+\delta}$.

2.3.4 Spectroscopic Ellipsometry

The third technique we introduce here is spectroscopic ellipsometry. This relatively new technique has two major advantages over the previous techniques. Firstly, the technique is self-normalizing meaning that no reference measurement has to be done and secondly, it provides directly both the real and imaginary parts of the dielectric function.

As with the grazing incidence technique we have to distinguish between s- and p-polarized light and label the crystal axes. Instead of measuring R_p or R_s independently, we now measure directly the amplitude and phase of the ratio $\hat{r}_p/\hat{r}_s = |\hat{r}_p/\hat{r}_s|e^{i(\eta_p-\eta_s)}$. To see how this can be done we first describe the experimental setup. There are a number of different setups one can use and here we describe the simplest. This setup consists of a source followed by a polarizer. With this polarizer we can change the orientation of the polarization impinging on the sample. The light reflected from the sample passes through another polarizer (called analyzer) and then hits the detector. Depending on the orientation of the first polarizer we can change the electric field strength of s- and p-polarized light according to,

$$E_p = |E_i|\cos(P), \tag{2.79}$$

$$E_s = |E_i|\sin(P). \tag{2.80}$$

$$\tag{2.81}$$

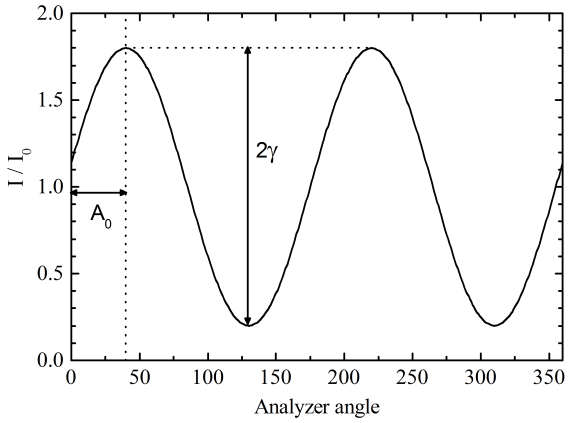

Figure 2.12: Result of an ellipsometric measurement. The phase shift A_0 and amplitude 2γ are the two quantities that we are interested in.

From the expressions for $\hat{r}_p$ and $\hat{r}_s$, (2.75) and (2.76), in the previous section it follows that,

$$\hat{\rho} \equiv \frac{r_{\mathrm{p}}}{r_{\mathrm{s}}} = \frac{\sqrt{\hat{n}_c^2 - \sin^2\theta} - \hat{n}_c\hat{n}_b\cos\theta}{\sqrt{\hat{n}_c^2 - \sin^2\theta} + \hat{n}_c\hat{n}_b\cos\theta} \cdot \frac{\sqrt{\hat{n}_a^2 - \sin^2\theta} + \cos\theta}{\sqrt{\hat{n}_a^2 - \sin^2\theta} - \cos\theta}. \tag{2.82}$$

Our task is now to invert this equation and express the optical constants in terms of measured quantities and instrument parameters. For an isotropic sample this can be done quite easily. We define the pseudodielectric function $\tilde{\varepsilon}$ such that:

$$\hat{\rho} \equiv \frac{\sin\theta\tan\theta - \sqrt{\tilde{\varepsilon} - \sin^2\theta}}{\sin\theta\tan\theta + \sqrt{\tilde{\varepsilon} - \sin^2\theta}}, \tag{2.83}$$

where we note that $\hat{\varepsilon} = \varepsilon_a = \varepsilon_b = \varepsilon_c$ in an optically isotropic medium. This equation can be inverted to obtain $\tilde{\varepsilon}$,

$$\tilde{\varepsilon}(\omega) = \sin^2\theta\left[1 + \tan^2\theta\left(\frac{1-\rho}{1+\rho}\right)^2\right]. \tag{2.84}$$

So all that is left to do is to express $\hat{\rho}$ in terms of experimental parameters. The experiment is done in the following way: we fix the polarizer at some angle $0 < P < 90$ and then we record the intensity while rotating the analyzer 360 degrees. The result is shown in figure 2.12. We then measure the amplitude of the resulting sine wave, γ and the phase offset with respect to zero, A_0 (we assume here that for $P = 0$ the polarizer and analyzer are aligned parallel to each other). With some goniometry and figure 2.12 we can show that,

$$\tan 2A_0 = \frac{2\rho_1\tan(P)}{|\rho|^2 - \tan^2(P)}, \tag{2.85}$$

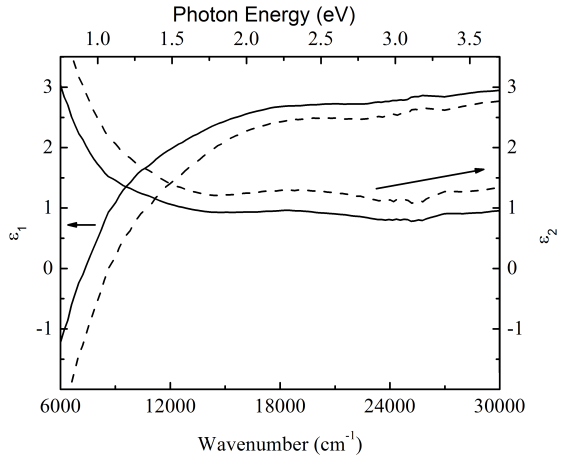

Figure 2.13: Dielectric function measured ellipsometrically on a $HgBa_2CuO_{4+\delta}$ sample. The true dielectric function is shown in solid lines. The pseudo dielectric function (i.e. actually measured) is shown as a dashed line. Data taken from ref. [50] and discussed in chapter 3 of this work.

and

$$\gamma = \frac{\sqrt{4\rho_1^2 \tan^2(P) + \left(|\rho|^2 - \tan^2(P)\right)^2}}{|\rho|^2 + \tan^2(P)}. \tag{2.86}$$

The combination of these equations with Eq. (2.84) is all we need to describe an ellipsometric experiment on an isotropic sample. For an anisotropic sample the problem is slightly more difficult. However, there exists a theorem due to Aspnes which states that the inversion of Eq. (2.82) results in Eq. (2.84) but now the dielectric function on the left-hand side is a so-called pseudo-dielectric function. This pseudo-dielectric function is mainly determined by the component parallel to the intersection of sample surface and plane of incidence (component along b in figure 2.10), but still contains a small contribution of the two other components. If we perform three measurements, each along a different crystal axis, we can correct the pseudo dielectric functions and obtain the true dielectric functions. If the sample is isotropic along two directions, as is the case in high temperature superconductors for example, only two measurements are required. Figure 2.13 shows in dashed lines the pseudo dielectric function of $HgBa_2CuO_4$. In this case the a and b axes have the same optical constants. The c-axis dielectric function was determined from reflectivity measurements and subsequently used to correct the pseudo dielectric function measured by ellipsometry on the ab-plane. The true dielectric function after this correction is shown as the solid line.

2.4 Quantum theory

We now move to the quantum theoretical description of the interaction of light and matter using the Kubo-formalism. So far we have been using a "geometrical" or macroscopic view of this interaction,

but in this section we will consider the effects of the absorption of photons by electrons. Consider for simplicity a metal. The electronic states of the system are described by a set of bands, some of which are fully occupied, some partially and the rest empty, figure 2.14. When photons interact with these

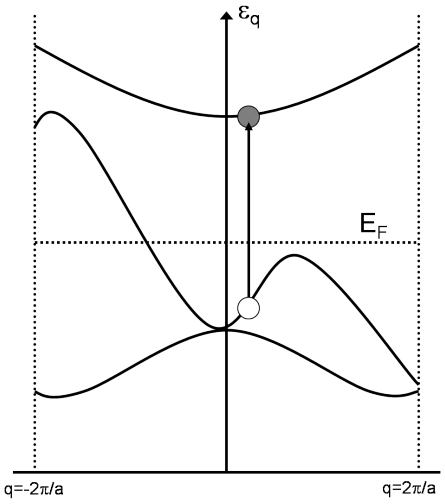

Figure 2.14: The indicated transition is an interband transition. Al states below the dashed line indicated by E_F are occupied all states above are empty.

band electrons they can be absorbed and in this process the electron is excited to a higher lying band leaving behind a hole. In this way we create electron-hole pairs and this (dipole) transition from a state $|\Psi_\nu^N\rangle$ to a state $|\Psi_\mu^N\rangle$ is characterized by an optical matrix element,

$$M_{\mu\nu}(\vec{q}) = \left\langle \Psi_\mu^N \; |\hat{\mathbf{v}}_q| \; \Psi_\nu^N \right\rangle . \tag{2.87}$$

If the transition is from one band to another band we call the transition an *interband* transition and if the transition is within a band we call it a *intraband* transition. In figure 2.15 we show the optical conductivity of KCl. In this compound a strong onset is seen in the optical conductivity around ≈8.7 eV. This onset is due to the excitation of electrons from the occupied p-band related to the Cl^- ions to the unoccupied s-band of the K^+ ions. Since this particular transition involves moving charge from the chlorine atoms to the potassium atoms this type of excitation is called a charge transfer (CT) excitation [26]. Another important feature in figure 2.15 are the strong peaks seen around 7.5 eV. Many theories often neglect so-called vertex corrections because these corrections cancel if the interactions between electrons are isotropic. However in real materials interactions are more often than not anisotropic and this means that these corrections have to be taken into account. The peaks seen in figure 2.15 are due to transitions from bound states of electron-hole pairs, called excitons, which arise due to the vertex corrections. Before we start our display of the Kubo-formalism we first introduce some notation. We

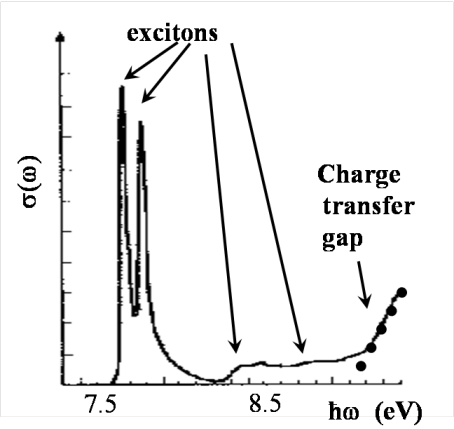

Figure 2.15: Optical conductivity of KCl. The series of strong peaks are due to excitons. The onset in absorption around 9 eV is the onset of charge transfer excitations.

introduce the field operators,

$$\psi^\dagger_\sigma(\mathbf{r}) = \sum_k e^{-i\mathbf{k}\cdot\mathbf{r}} \hat{c}^\dagger_{k,\sigma}. \tag{2.88}$$

The density operator is given by,

$$\hat{n}_\sigma(\mathbf{r}) = \psi^\dagger_\sigma(\mathbf{r})\psi_\sigma(\mathbf{r}). \tag{2.89}$$

The Fourier transform of $\hat{n}_\sigma(\mathbf{r})$ is,

$$\hat{n}_\sigma(\mathbf{r}) = \frac{1}{V}\sum_q e^{-i\mathbf{q}\cdot\mathbf{r}} \rho_q, \tag{2.90}$$

with

$$\rho_q = \sum_{k,\sigma} \hat{c}^\dagger_{k-q/2,\sigma} \hat{c}_{k+q/2,\sigma}. \tag{2.91}$$

The velocity operator is defined as,

$$\hat{\mathbf{v}}_q = \frac{\hbar}{m}\sum_{k,\sigma} \mathbf{k}\hat{c}^\dagger_{k-q/2,\sigma} \hat{c}_{k+q/2,\sigma}. \tag{2.92}$$

Finally, we note that the operators $\hat{n}_\sigma(\mathbf{r})$ and $\hat{\mathbf{v}}_q$ satisfy,

$$\frac{i}{\hbar}\left[\hat{n}_\sigma(\mathbf{r}), \hat{H}\right] + \nabla\cdot\hat{\mathbf{v}}_q = 0. \tag{2.93}$$

2.4.1 The Kubo-formalism

To calculate the optical conductivity from a microscopic starting point we have to add to the Hamiltonian of the system a term that describes the interaction with the electromagnetic field described by,

$$\mathbf{E}^T(\mathbf{r},t) = \frac{i\omega}{c}\sum_q \mathbf{A}_q e^{i(\mathbf{q}\cdot\mathbf{r}-\omega t)}, \tag{2.94}$$

Note that we have chosen the transverse gauge which we will use throughout the rest of the chapter. The interaction Hamiltonian is given by,

$$H' = -\frac{e\hbar}{c}\sum_q e^{i(\mathbf{q}\cdot\mathbf{r}-\omega t)}\mathbf{A}_q\cdot\hat{\mathbf{v}}_{-q}, \tag{2.95}$$

and in the presence of an electromagnetic field we use the minimal coupling,

$$\hat{\mathbf{v}}_q \to \hat{\mathbf{v}}_q - \frac{e\hbar}{mc}\mathbf{A}_q e^{i(\mathbf{q}\cdot\mathbf{r}-\omega t)}\hat{\rho}_q. \tag{2.96}$$

We now start by examining the current operator $\mathbf{J}(\mathbf{r},t) = \mathbf{J}^{(1)}(\mathbf{r},t)+\mathbf{J}^{(2)}(\mathbf{r},t)$. It consists of two terms the first of which is called the diamagnetic term,

$$\mathbf{J}^{(1)}(\mathbf{r},t) = -\frac{ne^2}{mc}\mathbf{A}(r,t) = \frac{ine^2}{m\omega}\mathbf{E}^T(r,t), \tag{2.97}$$

where in the last equality we have used Eq. (2.94). The second term is more difficult. It is given by,

$$\mathbf{J}^{(2)}(\mathbf{r},t) = \frac{e^2}{V}\int_{-\infty}^{\mathrm{t}}\left\langle \mathrm{e}^{\mathrm{i}H'\tau}\mathrm{e}^{-\mathrm{i}H\tau}\hat{\mathbf{v}}(r,t)\mathrm{e}^{\mathrm{i}H\tau}\mathrm{e}^{-\mathrm{i}H'\tau}\right\rangle \mathrm{e}^{\mathrm{i}\omega(\mathrm{t}-\tau)}\mathrm{d}\tau. \tag{2.98}$$

We make here the approximation of using linear response theory: we expand the exponentials $e^{iH'\tau}$ to first order in $\mathbf{A}(\mathbf{r},t)$ and then stop the series expansion. After some algebra we arrive at,

$$\frac{J^{(2)}}{\mathbf{E}(\mathbf{r},t)} = \frac{ie^2}{\omega V}\sum_n \mathbf{v}_{-q}^{nm}\mathbf{v}_q^{mn}\left[\frac{1}{\omega - E_n + E_m + i0^+} - \frac{1}{\omega + E_n - E_m + i0^+}\right], \tag{2.99}$$

where we have defined,

$$\mathbf{v}_q^{mn} \equiv \langle\Psi_m|\hat{\mathbf{v}}_q|\Psi_n\rangle. \tag{2.100}$$

The result we have obtained is for zero temperature but is easily generalized to finite T if we use the grand canonical ensemble. Combining Eq. (2.97) and Eq. (2.99) we find for the optical conductivity,

$$\sigma_{\alpha,\alpha}(\mathbf{q},\omega) = \frac{iNe^2}{mV\omega} + \frac{ie^2}{V\omega}\sum_{n,m\neq n} e^{\beta(\Omega-E_n)}\left[\frac{v_{\alpha,q}^{nm}v_{\alpha,-q}^{mn}}{\omega-\omega_{mn}+i\eta} - \frac{v_{\alpha,-q}^{nm}v_{\alpha,q}^{mn}}{\omega+\omega_{mn}+i\eta}\right], \tag{2.101}$$

where we have defined $\omega_{mn} \equiv E_m - E_n$. The optical conductivity consists now of three contributions: the diamagnetic term followed by a contribution to positive frequencies and a contribution to negative frequencies. We note that in general $\sigma_{\alpha,\alpha}(\mathbf{q},\omega)$ is a tensor as indicated by the α subscripts. We further note that the diamagnetic term does not give a real contribution to the conductivity. This term gives a δ-function contribution at zero frequency and this is exactly canceled by a delta function in the second part. This can be seen by using the fact that for every n we have the following relationship,

$$\sum_{n,m\neq n}\frac{v_{\alpha,q}^{nm}v_{\alpha,-q}^{mn}}{\omega_{mn}} = \frac{N}{2m}. \tag{2.102}$$

So we can rewrite Eq. (2.101) as,

$$\sigma_{\alpha,\alpha}(\mathbf{q},\omega) = \frac{ie^2}{V}\sum_{n,m\neq n}\frac{e^{\beta(\Omega-E_n)}}{\omega_{mn}}\left[\frac{v^{nm}_{\alpha,q}v^{mn}_{\alpha,-q}}{\omega-\omega_{mn}+i\eta}+\frac{v^{nm}_{\alpha,-q}v^{mn}_{\alpha,q}}{\omega+\omega_{mn}+i\eta}\right], \tag{2.103}$$

From here on we take the limit $q \to 0$ and define a generalized oscillator strength Ω_{mn} as,

$$\Omega^2_{mn} \equiv \frac{8\pi e^2 e^{\beta(\Omega-E_n)}|v^{nm}_{\alpha}|^2}{\omega_{mn}V}. \tag{2.104}$$

With this definition we are lead to the Drude-Lorentz expansion of the optical conductivity,

$$\sigma_{\alpha,\alpha}(\omega) = \frac{i\omega}{4\pi}\sum_{n,m\neq n}\frac{\Omega^2_{mn}}{\omega(\omega+i\gamma_{mn})-\omega^2_{mn}}. \tag{2.105}$$

2.4.2 Sum Rules

Sum rules play an important role in optics. Using the equations of the previous section we derive the Thomas-Reich-Kuhn sum rule also known as the f-sum rule. The f-sum rule states that, apart from some constants, the area under σ_1 is proportional to the number of electrons and inversely proportional to their mass. This can be shown as follows: integrating Eq. (2.105) we have,

$$\mathrm{Re}\int_{-\infty}^{\infty}\sigma(\omega)\,d\omega = \frac{1}{4}\sum_{n,m\neq n}\Omega^2_{mn}. \tag{2.106}$$

Using the expression for Ω_{mn}, Eq. (2.104), and expression (2.102) we can rewrite the sum on the right hand side as,

$$\sum_{n,m\neq n}\Omega^2_{mn} = \frac{4\pi e^2 N}{mV}\sum_{n}e^{\beta(\Omega-E_n)} = \frac{4\pi e^2 N}{mV}. \tag{2.107}$$

So the f-sum rule states that,

$$\int_{-\infty}^{\infty}\sigma_1(\omega)d\omega = \frac{\pi e^2 N}{mV}, \tag{2.108}$$

as promised. This is the full universal sum rule. It is often rewritten as an integral over positive frequencies only and using the definition of the plasma frequency ω_p,

$$\omega_p^2 \equiv \frac{4\pi e^2 N}{mV}, \tag{2.109}$$

as,

$$\int_0^{\infty}\sigma_1(\omega)d\omega = \frac{\omega_p^2}{8}. \tag{2.110}$$

We can also define *partial* sum rules, i.e. sum rules where we integrate up to a certain frequency cutoff Ω_c. In such a case the sum rule is not universal (this means for instance that the value of this sum rule

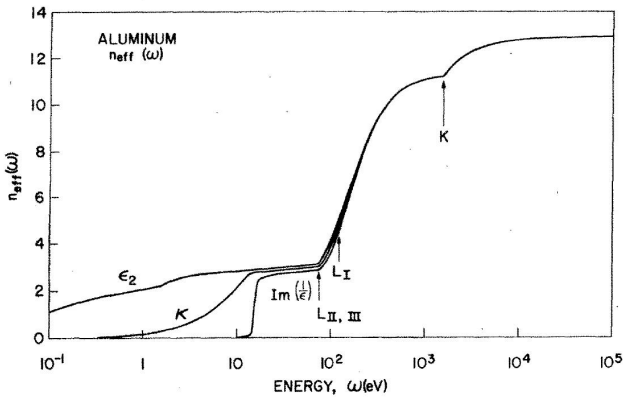

Figure 2.16: Effective number of carriers $n_{eff}(\Omega_c)$ as a function of cutoff frequency Ω_c for Al. Figure adapted from [51].

can depend on temperature) and we can now define a plasma frequency that depends on the chosen cutoff frequency,

$$\omega^2_{p,valence} \equiv \frac{4\pi e^2}{m} n_{eff}(\Omega_c). \tag{2.111}$$

A nice example of the application of the partial sum rule is shown in figure 2.16. Here the partial sum rule is applied to the optical conductivity of aluminum [51]. Here the effective number of carriers contributing to the sum rule is plotted as a function of Ω_c. $n_{eff}(\Omega_c)$ slowly increases to a value of roughly three around 50 eV. This means that as we increase the cutoff from zero to 50 eV we are slowly integrating over the intraband transitions and when we reach a value of 50 eV we have integrated over all transitions involving the three valence electrons. For higher energies the interband transitions start to contribute with a sharp onset near 80 eV. Finally at 10^4 eV the sum rule saturates at 13 electrons, the total number of electrons of aluminum.

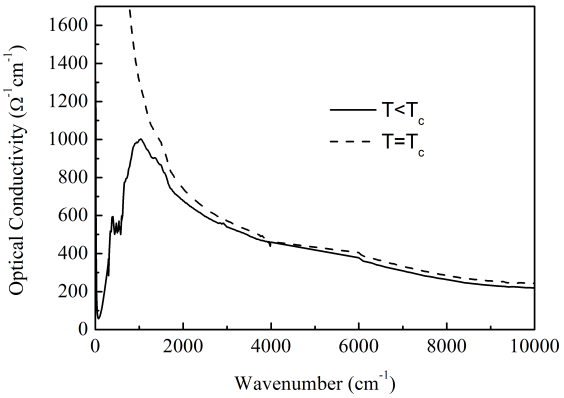

Figure 2.17: Optical conductivity of Bi-2212 at T_c and below. The difference in area between the two curves is an estimate of the superfluid density.

Another application of sum rules can be found in superconductors. In a superconductor the electrons form a superfluid condensate. This condensate shows up in the optical conductivity as a delta function at zero frequency (it contributes a diamagnetic term as in Eq. (2.101)). At the same time a gap opens up in low frequency part of the spectrum where the optical conductivity is (close to) zero, see figure 2.17. In the normal state the system is usually metallic and characterized by a Drude peak. In optical experiments we cannot measure the zero frequency response and so we cannot directly measure the spectral weight $\omega_{p,s}^2$ of the condensate. However, using sum rules we can estimate its spectral weight because the total spectral weight has to remain constant. This is summarized in the Ferrel-Glover-Tinkham (FGT) sum rule [52], which states that the difference in spectral weight between the optical conductivity in the superconducting and normal state is precisely the spectral weight of the condensate,

$$\omega_{p,s}(T)^2 = 8 \int_{0^+}^{\infty} \{\sigma(\omega, T_c) - \sigma(\omega, T)\}\, d\omega. \tag{2.112}$$

Note that we integrate here from 0^+.

We will now derive expressions for the conductivity sum rule from a more microscopic point of view [53]. To do that we return to the Kubo expression for the optical conductivity,

$$\sigma_1(\omega) = \frac{\pi e^2}{V} Tr \left\langle \Psi_n \right| \hat{\mathbf{v}} \left\{ \frac{\delta\left(\omega - \hat{H} + E_n\right)}{\hat{H} - E_n} + \frac{\delta\left(\omega + \hat{H} - E_n\right)}{\hat{H} - E_n} \right\} \hat{\mathbf{v}} \left| \Psi_n \right\rangle. \tag{2.113}$$

The Hamiltonian in this expression is that of the system of interacting electrons without the interaction of light. It represents the optical conductivity for the system in an arbitrary (ground or excited) many-body state $|\Psi\rangle$. A peculiar point of this expression is that although the velocity operators create a single electron-hole pair, due to the fact that the hamiltonian in the denominator of this expression still contains the interactions between all particles in the system, the optical conductivity represents the response from the full collective system of electrons. If we integrate this expression over frequency we get,

$$\int_{-\infty}^{\infty} \sigma_1(\omega)\, d\omega = \frac{2\pi e^2}{V} Tr \left\langle \Psi_n \right| \hat{\mathbf{v}} \frac{1}{\hat{H} - E_n} \hat{\mathbf{v}} \left| \Psi_n \right\rangle. \tag{2.114}$$

We now take a closer look at the right-hand side of this expression. Remember that,

$$\hat{\mathbf{v}} = \frac{i}{\hbar} \left[\hat{H}, \hat{\mathbf{x}}\right]. \tag{2.115}$$

Using the commutator we can rewrite,

$$-2i\hbar\hat{\mathbf{v}} \frac{1}{\hat{H} - E_n} \hat{\mathbf{v}} = \left(\hat{H}\hat{\mathbf{x}} - \hat{\mathbf{x}}\hat{H}\right) \frac{1}{\hat{H} - E_n} \hat{\mathbf{v}} + \hat{\mathbf{v}} \frac{1}{\hat{H} - E_n} \left(\hat{H}\hat{\mathbf{x}} - \hat{\mathbf{x}}\hat{H}\right). \tag{2.116}$$

Inserting this back into Eq. (2.114) we find after some rearranging

$$\int_{-\infty}^{\infty} \sigma_1(\omega)\, d\omega = \frac{i\pi e^2}{\hbar V} \langle [\hat{\mathbf{v}}, \hat{\mathbf{x}}] \rangle , \tag{2.117}$$

where $\langle ... \rangle$ stands for the trace over all many-body states. Here we have used that,

$$\hat{\mathbf{x}}\hat{H}\frac{1}{\hat{H}-E_n}\hat{\mathbf{v}} = \hat{\mathbf{x}}\left(\hat{H}-E_n\right)\frac{1}{\hat{H}-E_n}\hat{\mathbf{v}} + \hat{\mathbf{x}}E_n\frac{1}{\hat{H}-E_n}\hat{\mathbf{v}} = \hat{\mathbf{x}}\hat{\mathbf{v}} + \hat{\mathbf{x}}E_n\frac{1}{\hat{H}-E_n}\hat{\mathbf{v}}, \tag{2.118}$$

and the fact that $\hat{H}|\Psi_n\rangle = E_n|\Psi_n\rangle$. We can now obtain different expressions for the sum rule by working out the commutator on the right-hand side of Eq. (2.117) based on different model assumptions. In table 2.2 we summarize some results. The sum rule for band electrons is in practice the most

Free electrons	$[\hat{\mathbf{v}}, \hat{\mathbf{x}}] = \frac{\hbar}{im}\sum_{k\sigma} \hat{n}_{k\sigma}$
Band electrons	$[\hat{\mathbf{v}}, \hat{\mathbf{x}}] = \frac{\hbar}{im}\sum_{k\sigma} \hat{n}_{k\sigma} [\hat{\mathbf{v}}, \hat{\mathbf{x}}] = \frac{\hbar}{i}\sum_{k\sigma} \frac{\partial^2 \varepsilon_{k\sigma}}{\partial k^2}\hat{n}_{k\sigma}$
N.N.	$[\hat{\mathbf{v}}, \hat{\mathbf{x}}] = -\frac{\hbar a^2}{i}\sum_{k\sigma} \varepsilon_{k\sigma}\hat{n}_{k\sigma}$

Table 2.2: Expressions for the commutator in Eq. (2.117) for three different cases. N.N. stands for Nearest Neighbors tight binding model

useful. Suppose that we have a system with only a single reasonably well isolated band around the Fermi level that can be approximated by a tight binding dispersion $\varepsilon_k = -t\cos(ka)$. In that case we find an interesting relation,

$$\int_0^{\Omega_c} \sigma_1(\omega, T) d\omega = -\frac{\pi e^2 a^2}{2\hbar^2 V}\sum_{k,\sigma} \langle \hat{n}_{k\sigma}\varepsilon_k \rangle_T = -\frac{\pi e^2 a^2}{2\hbar^2 V} E_{kin}(T). \tag{2.119}$$

This sum rule states that by measuring the optical spectral weight we are in fact measuring the kinetic energy of the charge carriers contributing to the optical conductivity. In real systems this relation only holds approximately: usually there are other bands lying nearby and the integral on the left contains contributions from these as well. Often the bands are described by more complicated dispersion relations in which case the relation $\partial^2\varepsilon_k/\partial k^2 = -\varepsilon_k$ does not hold. We can make some other observations from the sum rule for band electrons. Suppose again we have a single empty cosine like band (it is only necessary that the band is symmetric but it simplifies the discussion) at $T = 0$. Since the band is empty, the spectral weight is equal to zero. If we start adding electrons the spectral weight starts to increase until we reach half-filling. If we add more electrons the spectral weight will start to decrease again because the second derivative becomes negative for $k > \pi/2a$. If we completely fill the band the contributions from $k > \pi/2a$ will precisely cancel the contributions from $k < \pi/2a$ and the

spectral weight is again zero. Now consider what happens if we have a half-filled band and start to increase the temperature. Due to the smearing of the Fermi-Dirac distribution higher energy states will get occupied leaving behind lower energy empty states. The result of this is that the spectral weight starts to decrease. One can show using the Summerfeld expansion that the spectral weight follows a T^2 temperature dependence. In the extreme limit of $T \to \infty$ something remarkable happens: the Fermi-Dirac distribution is 1/2 everywhere and the electrons are equally spread out over the band. The metal has become an insulator!

2.4.3 Applications of sum rules to superconductors

Before we have a look at some applications of sum rules to superconductors we first summarize some results from BCS theory. We want to apply our ideas to cuprate superconductors so we use a modified version from the original theory to include the possibility of d-wave superconductivity. In other words we suppose that there is some attractive interaction between the electrons that has a momentum dependence. The energy difference between the normal and superconducting state due to interactions can be written as [54],

$$\langle \hat{H}_s^{int} \rangle - \langle \hat{H}_s^{int} \rangle = \int d^3 r g(r) V(r) = \sum_k g_k V_k, \tag{2.120}$$

where $g(r)$ and g_k are the pair correlation function and its fourier transform respectively. We can find

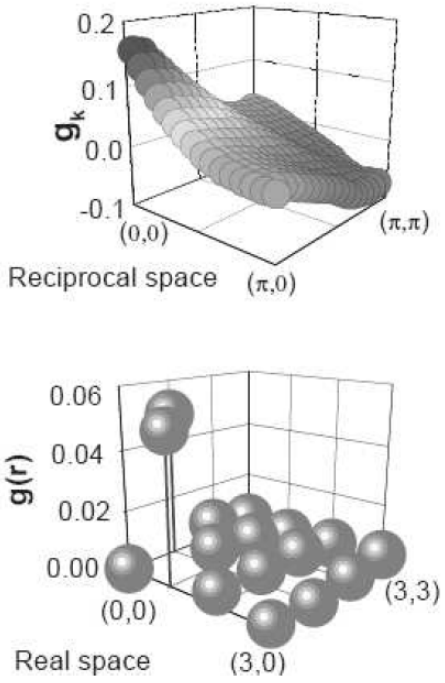

Figure 2.18: Real and momentum space picture of the correlation functions $g(r)$ and g_k. Figure adapted from [54].

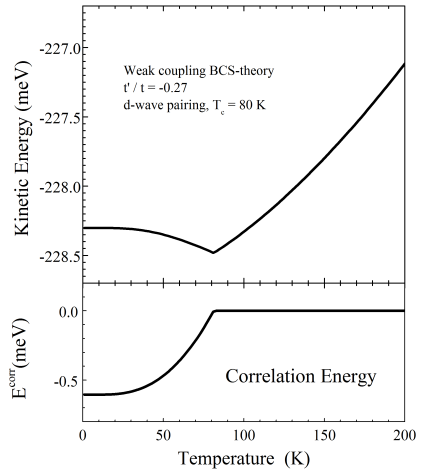

Figure 2.19: Correlation energy and kinetic energy as a function of temperature for a d-wave BCS superconductor. Figure adapted from [54].

an expression for g_k,

$$g_k = \sum_q \frac{\Delta_{q+k}\Delta_q^*}{4E_{q+k}E_q}. \tag{2.121}$$

As usual,

$$E_k = \sqrt{(\varepsilon_k - \mu)^2 + \Delta^2}, \tag{2.122}$$

and the temperature dependence of Δ_k is given by,

$$\Delta_k = \sum_q \frac{V_q\Delta_q}{2E_q} \tanh\left(\frac{E_k}{2k_bT}\right). \tag{2.123}$$

We now use a set of parameters extracted from ARPES measurements to do some numerical simulations. First of all we calculate g_k and fourier transform it to obtain $g(r)$. The results are shown in figure 2.18.

Although g_k is not so illuminating $g(r)$ is. This function is zero at the origin and strongly peaked at the nearest neighbor sites. This is a manifestation of the d-wave symmetry. We also note that the correlation function drops off very fast for sites removed further from the origin. In figure 2.19 we show the results for a calculation of the correlation and kinetic energy using the parameters extracted from ARPES measurements on Bi-2212. The kinetic energy is calculated from,

$$\langle \hat{H}_{kin} \rangle = \sum_k \varepsilon_k \{1 - \frac{\varepsilon_k - \mu}{E_k} \tanh\left(\frac{E_k}{2k_bT}\right)\}. \tag{2.124}$$

We see that the kinetic energy *increases* in the superconducting state. This can be easily understood by looking at what happens to the particle distribution function below T_c, as indicated in the left panel of figure 2.20: when the system enters the superconducting state the area below the Fermi energy

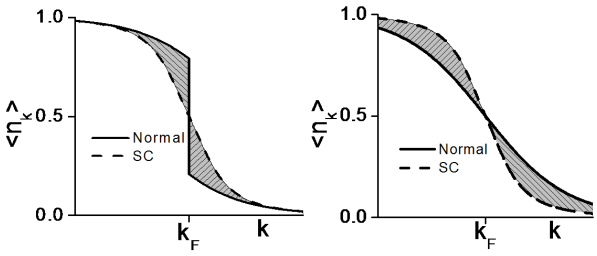

Figure 2.20: Left: Distribution function for the normal (Fermi liquid like) state and the superconducting state. Right: Distribution function for a non-Fermi Liquid like state and the superconducting state.

decreases and the area above the Fermi energy increases thereby increasing the total kinetic energy of the system. Nevertheless the total internal energy, which is the sum of the interaction energy and the kinetic energy, decreases and this is of course why the system becomes superconducting. Now let us take a look at what happens in the cuprates. In figure 2.21 we display the optical spectral weight $W(\Omega_c, T)$ as a function of T^2 for Bi-2223. To compare this to the BCS kinetic energy we have plotted here $-W(\Omega_c, T)$. This result is contrary to the expectation for BCS theory: the kinetic energy decreases in the superconducting state. This experimental result, observed first by Molegraaf *et al.* [45], has sparked a lot of interest both experimentally [55, 56, 46, 47, 50] and theoretically [57, 58, 59, 60, 61, 62, 54, 63, 64, 35, 65, 66, 67, 68, 69, 70, 71]. At first it was believed that this observation indicated a lowering of kinetic energy at the superconducting transition. Roughly speaking

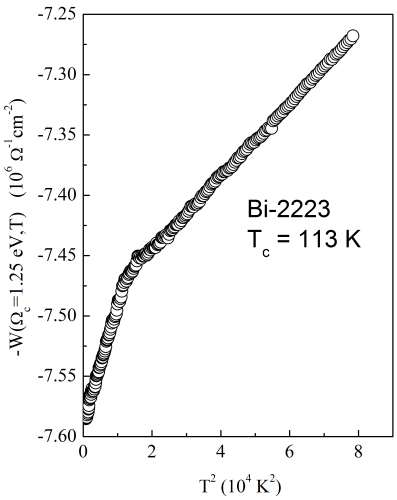

Figure 2.21: Temperature dependent spectral weight of Bi-2223. Data taken from ref. [47].

the effect arises due to the "strangeness" of the normal state (right panel figure 2.20). It is well known that the normal state of the cuprates shows non Fermi-liquid behavior. So if the distribution function in the normal state does not show the characteristic step at the Fermi energy but is rather a broadened function of momentum it is very well possible that the argument we made for the increase of the kinetic energy above is reversed. The spectral weight analysis has been carried out for several samples [45, 46, 47, 50]. In section 3.11 we will discuss this analysis in much more detail for Hg1201. Here we summarize the results for all samples studied in figure 2.22, where the superconductivity induced change in spectral weight is plotted. Underdoped and optimally doped samples generally show a kinetic energy change that points in the direction of kinetic energy saving, while overdoped samples show the opposite effect. DMFT calculations of the Hubbard model can reproduce the effect of a change of

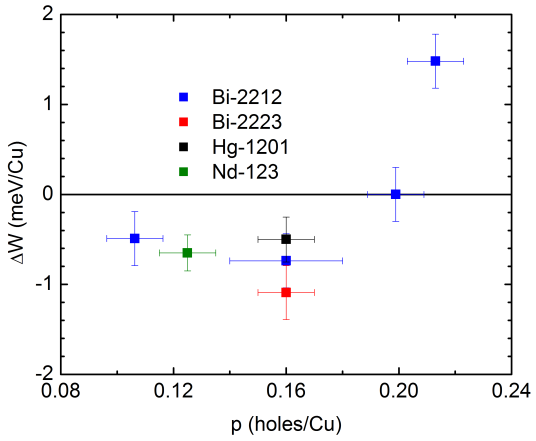

Figure 2.22: Doping dependence of spectral weight transfer at T_c .

spectral weight at the superconducting transition [64]. However, the temperature dependence of the spectral weight in these calculations is somewhat different from that observed in experiment (see fig 8a in Ref. [46]). In chapter 6 we will study the temperature dependence of the optical spectral weight in a model where the electrons interact through the exchange of bosons.

2.4.4 Extended Drude formalism

We have already encountered the Drude formula for the optical conductivity of a metal (see section 2.2.4). Even though this model is based on a classical gas of non-interacting particles it describes amazingly well the optical properties of a good metal. This is even more surprising if one realizes that in a metal electrons reside in bands and that the transitions we are making with photons are vertical due to the negligible photon momentum. So from the band picture point of view, when we consider a single band of electrons interacting with photons we should expect a single delta function at the origin. The reason that a broadened peak is observed, is because we have neglected the other interactions in

the system. Electrons in solids interact with impurities, the lattice vibrations and/or other collective modes. Due to the electron-phonon interaction for instance we can have processes where a photon creates an electron-hole pair in which the electron "shakes off" a phonon. In this process the phonon can carry away a much larger momentum then originally provided by the photon. Due to this effect we can have phonon-assisted transitions which give a width $1/\tau$ to the delta function. This width is called the scattering rate. If the interactions are inelastic, as in the interactions with impurities, this scattering rate is just a constant. Otherwise, this scattering rate can depend on frequency. However, if we define the scattering rate in Eq. (2.57) to be frequency dependent, $1/\tau \equiv 1/\tau(\omega)$, the KK-relations force us to introduce a frequency dependent effective mass as well. This leads to the generalized or extended Drude formalism [72]. The optical conductivity is written as,

$$\sigma\left(\omega\right) = \frac{ne^2/m}{\tau^{-1}(\omega) - \mathrm{i}\omega m*(\omega)/m}. \tag{2.125}$$

Having measured a conductivity spectrum we can invert these equations to calculate $1/\tau(\omega)$ or $m^*(\omega)/m$ via,

$$\tau^{-1}(\omega) \equiv \mathrm{Re}\frac{ne^2/m}{\sigma\left(\omega\right)} = \Sigma''_{opt}(\omega), \tag{2.126}$$

and

$$\frac{m^*(\omega)}{m} \equiv \mathrm{Im}\frac{-ne^2/m}{\omega\sigma\left(\omega\right)} = 1 + \frac{\Sigma'_{opt}(\omega)}{\omega}. \tag{2.127}$$

In the last equality of these equations we have defined an optical self-energy. Note that this quantity is *not* equivalent to the self-energy used in the context of Green's functions. We can rewrite the optical conductivity in terms of $\Sigma_{opt}(\omega)$ as,

$$\sigma\left(\omega\right) = \frac{\omega_p^2}{4\pi}\frac{i}{\omega + \Sigma_{opt}\left(\omega\right)}. \tag{2.128}$$

where we introduced the plasma frequency ω_p . In the absence of interactions of the electrons with impurities, the lattice or themselves the response of the electron gas to an applied alternating electric field is purely reactive and the real part of the conductivity is characterized by a zero frequency delta function. In the case of impurity scattering $\Sigma_{opt}(\omega)$ is simply given by

$$\Sigma_{opt}\left(\omega\right) = i/\tau_0, \tag{2.129}$$

so that $1/\tau(\omega) = 1/\tau_0$ and $m*(\omega)/m = 1$, retrieving the standard Drude result. If dissipation can occur by other interactions, like the electron-phonon interaction, $\Sigma_{opt}(\omega)$ can have more complicated frequency dependencies as we will see in chapter 5.

Although $\Sigma_{opt}(\omega)$ is simply related to the real and imaginary parts of $1/\sigma(\omega)$, there is a subtlety that one has to consider to reliably extract it from experimental data. This is best illustrated by expressing

$\Sigma_{opt}(\omega)$ in terms of the dielectric function $\epsilon(\omega) = \epsilon_1(\omega) + i\epsilon_2(\omega)$:

$$\Sigma'_{opt} = \frac{\omega_p^2}{\omega} \frac{\epsilon_{\infty,IR} - \epsilon_1(\omega)}{[\epsilon_{\infty,IR} - \epsilon_1(\omega)]^2 + \epsilon_2^2(\omega)} - \omega. \tag{2.130}$$

and

$$\Sigma''_{opt} = \frac{\omega_p^2}{\omega} \frac{\epsilon_2(\omega)}{[\epsilon_{\infty,IR} - \epsilon_1(\omega)]^2 + \epsilon_2^2(\omega)} \tag{2.131}$$

Here $\epsilon_{\infty,IR}$ is the contribution to the dielectric function in the infrared arising from interband transitions which should not be taken into account in the single component approach. The subtlety is therefore in the choice of $\epsilon_{\infty,IR}$ and ω_p. The choice of $\epsilon_{\infty,IR}$ is not so important at low energies where $|\epsilon_1| \gg \epsilon_{\infty,IR}$ but becomes important at higher energies. For example, early studies of the cuprates indicated that the scattering rate was linear in frequency up to energies as high as 1 eV [73], but if $\epsilon_{\infty,IR}$ is chosen as below the scattering rate starts to show signs of saturation already around 0.5 eV [74]. In our analysis we adopt the following convention: $\epsilon_{\infty,IR} = \epsilon_\infty + \sum_j S_j$ where the $S_j = \omega_{p,j}^2/\omega_{0,j}^2$ are the oscillator strengths of the interband transitions obtained from a Drude-Lorentz fit and ω_p is chosen such that $m^*(\omega)/m_b$ approaches unity at high energy ($\sim$1 eV). If we consider only the contribution of oxygen to the dielectric constant for the cuprates the polarizability is easily calculated using the Clausius-Mossotti relation,

$$\epsilon_{\infty,IR} \approx 1 + \frac{4\pi N\alpha/V}{1 - \frac{4\pi}{3}N\alpha/V} = 1 + \frac{\alpha_0}{1 - \gamma\alpha_0} \tag{2.132}$$

where N is the number of oxygens per unit cell, V is the unit cell volume and α is the polarizability of the oxygen atoms. In the second equality we have defined $\alpha_0 \equiv 4\pi N\alpha/V$. The factor $\gamma = 1/3$ appearing in the denominator is a geometrical factor for a cubic crystal structure which we keep for simplicity. For O^{2-} the ionic polarizability α $\approx$3.88·10^{-24} cm^3. Using unit cell parameters for $HgBa_2CuO_{4+\delta}$ of $a \times b \times c$ = 3.85 × 3.85 × 9.5 $\dot{A}$ and 4 oxygen atoms per unit cell we find $\epsilon_{\infty,IR} \approx 3.56$, which is fortuitously close to the estimate of 3.6 obtained from experiment in view of the lesser agreement for $Bi_2Sr_2CuO_{6+\delta}$, $Bi_2Sr_2CaCu_2O_{8+\delta}$ and$Bi_2Sr_2Ca_2Cu_3O_{10+\delta}$. For optimally doped Bi-2201, Bi-2212 and Bi-2223 we use $a \times b \times c$ = 5.4 × 5.4 × 24.6 $\dot{A}$, $a \times b \times c$ = 5.4 × 5.4 × 30.8 $\dot{A}$ and $a \times b \times c$ = 5.4 × 5.4 × 37.1 $\dot{A}$ respectively. These are the cell parameters corresponding to 4 formula units, i.e. $N = 24$, $N = 32$ and $N = 40$ oxygens respectively. This yields $\epsilon_{\infty,IR} \approx 4.58$, $\epsilon_{\infty,IR} \approx 5.16$ and $\epsilon_{\infty,IR} \approx 5.52$. As these values seem to anti-correlate with the estimated experimental values $\epsilon_{\infty,IR} \approx 4.9$ for Bi-2201, $\epsilon_{\infty,IR} \approx 4.5$ for Bi-2212 [74] and $\epsilon_{\infty,IR} \approx 4.1$ for Bi-2223 the above used picture is probably a bit too simplified. Nevertheless, both experiments and theory suggest $\epsilon_{\infty,IR} \approx 4$ - 5.

Chapter 3

Optical spectroscopy of high-T_c superconductors: $HgBa_2CuO_{4+\delta}$.

3.1 Introduction

We now focus on experimental results obtained from optical probes of high-T_c superconductors. The first section of this chapter discusses some general experimental details. The rest of the chapter discusses the optical and thermodynamic properties of Hg-1201. These results have been published in [50].

3.2 Experimental details

In the previous chapter we gave a broad overview of optical spectroscopic techniques, so we can suffice here with a brief summary of technical details concerning the experiments. Although the basic idea is simple, measuring optical spectra with a temperature interval of 2K with good statistics and reliable temperature dependencies is quite complicated. There are many factors that can influence the final results. As with all experimental techniques, experience and careful checking of results *while the experiments are in progress*, and sometimes a bit of luck, are requirements for success. In the following we discuss the equipment necessary for the experiments discussed in this thesis.

Temperature dependent experiments are performed in cryostats that are specially adapted to keep the sample position fixed during thermal cycling. Temperature is regulated by a controller with a fixed sweep rate to ensure that spectra are collected equidistant in temperature.

Far-infrared experiments are carried out at pressures of about $p \approx 10^{-6}$ mbar while the mid-infrared and ellipsometry experiments are carried out under ultra high vacuum conditions with $p \approx 10^{-9}$ mbar. Bi-2201 samples are freshly cleaved just before being inserted into the cryostat, while the

Hg-1201 sample was polished (see section 3.4. For each sample we collected reflectivity spectra and the dielectric function between 10 K and 300 K with a temperature interval of 2 K.

We use a Fourier Transform Infrared spectrometer for IR reflection experiments in the range 3 meV to 750 meV. The reference for the reflection measurements is taken on a gold film deposited *in-situ* on the sample. The infrared range is covered with three detectors. In the far infrared (FIR) we use a bolometer that covers two ranges : 20 - 80 cm^{-1} and 35 - 670 cm^{-1}. The first range can be accessed by pumping on the ^{4}He dewar that cools the detector element. At low enough pressure ^{4}He undergoes a transition into a superfluid state. The lower temperature increases the sensitivity in the very far IR as it reduces thermal excitation of charge carriers over the band gap in the silicon chip. The second range is the normal mode of operation of the bolometer. One typically uses a He - gas arc lamp as source in this frequency range although a Globar gives an equal intensity above 100 cm^{-1}. If properly prepared, a single filling with liquid ^{4}He allows one to take spectra for up to 14 hours while pumping or up to 26 hours when not pumping. An experiment in which we cool down slowly, followed by warming up slowly again while continuously acquiring spectra takes about 6 hours. So, in the best scenario we can make two runs while measuring spectra taken on the sample, followed by two runs taking spectra after depositing a gold film on the sample. This is preferred over a single measurement on either sample or gold since this allows us to detect whether there are problems related to drift in the detector. Drift can arise for several reasons. First, changes in room temperature and pressure in principle affect the performance of the entire spectrometer. Second, problems with the vacuum of the shielding dewar or electronics can cause additional drift in the detector. There are other issues that can cause systematic errors in the measured temperature dependence that are external to the detectors. When cooling down the copper piece connecting the cold finger of the cryostat to the sample can contract by as much as a few millimeters. In principle this contraction is absorbed by a flexible copper braid, while the sample itself is held in position by a steel wire. With to little tension on the steel wire the sample may move during thermal cycling. Another problem can occur when the vacuum at the sample position is to low. This can cause absorbtion of remaining gases in the cryostat on the sample surface which may affect the reflection coefficient of the sample. This caused particular problems in the experiments on Hg-1201 discussed below.

The second detector we use is an MCT detector that is cooled with liquid nitrogen. It covers the range 900 - 6000 cm^{-1} and is used in conjunction with a Globar source. The time during which the detector is cold (the lifetime) is much shorter: around 14 hours. The precise lifetime depends strongly on the vacuum of the shielding dewar. During the first two hours after filling the dewar the response of the detector is strongly time dependent and basically useless for experiments. It can be used if sample and reference measurement are taken quickly after one another. Otherwise, one has to wait for a period of 2.5 hours before starting experiments. This means that there is just enough time to do

one run on the sample and one on the deposited gold film. Since this is not very reliable and does not allow for testing the temperature dependence between several runs, a better method is to make only one run and then refill the dewar with nitrogen. We can take several measurements on the sample. If enough statistics is obtained on the temperature dependence of the sample, we take one final spectrum at room temperature, and then evaporate a layer of gold on the sample, followed by taking another spectrum. The spectrum before and after gold evaporation should be taken as quickly as possible to minimize drift. These two spectra will are used as reference for all the other measurements. If the vacuum shielding was well pumped and tight this is a very stable way to measure many runs as long as the detector is kept cold. The mid infrared data of Hg-1201 was obtained in this way. A total of 17 runs were made on sample and gold. This comprehensive set of experiments allowed us to determine the effect of absorption due to a thin layer of dirt that formed at low temperature on the sample surface (see also section 3.11).

Finally we used a DTGS detector in the range 400 - 6000 cm^{-1}. This detector is not cooled and therefore noisier than the other detectors. On the other hand, since there is no limit to the time one can take spectra one can make up for this by measuring for a longer time. In particular for larger samples this is a very powerful detector and preferable over the MCT. Moreover, it does not suffer from non-linearities in the response like the MCT.

Apart from the detectors each spectral range requires its own beamsplitter. The first is a multi-layer mylar beamsplitter which can be used in the range 35 - 670 cm^{-1}. The second beamsplitter consists of a thin Ge film supported by a KBr substrate. This one gives access to the range 370 - 7800 cm^{-1}.

We use a commercial Woolam spectrometer for ellipsometric measurements in the energy range 0.75 - 6 eV. This setup consists of a Xenon arc lamp followed by a monochromator. The light is then coupled into a fiber which ends at one arm of the ellipsometer. Here the light first passes through a polarizer that linearly polarizes the light. The ellipsometer itself consists of two rotatable arms with a central rotation axis. The sample is mounted on a holder or in a cryostat and has to be carefully mounted so that the sample surface coincides with the rotation axis of the two arms. If this is not the case, light will either not reach the detector or otherwise a mistake is made in the determination of the angle of incidence. The light reflected from the sample surface passes through a rotating polarizer (the analyzer) and then hits the detector.

The intensity is recorded as function of analyzer position. The resulting signals can be directly converted to the angles Ψ and Δ introduced in section 2.3.4.

3.3 $HgBa_2CuO_{4+\delta}$

The determination of the generic properties of high T_c superconductors has often been complicated by material and crystallographic issues. Examples are the structural distortion in Bi-2201, bi-layer split-

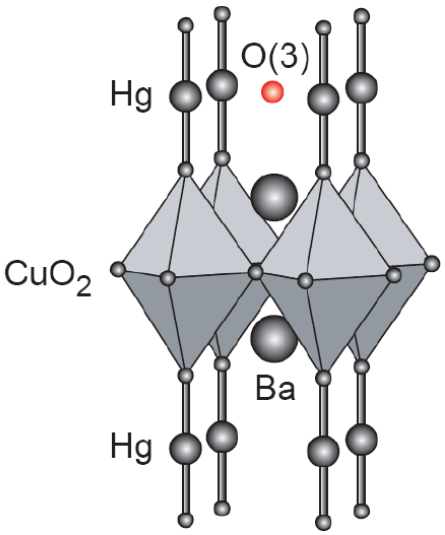

Figure 3.1: Crystal structure of $HgBa_2CuO_{4+\delta}$. The red atom indicates the position of the O(3) atom that acts as dopant. Adapted from [75].

ting of the electronic bands due to multiple copper-oxygen sheets per unit cell and the copper-oxygen chains present in YBCO. In order to obtain information on the phenomenon of superconductivity in the high T_c cuprates that is free from these complications one would like to study the simplest possible structure. The mercury based cuprates with their simple tetragonal structure (see Fig. 3.1) and in particular Hg1201, with only one copper-oxygen sheet per unit cell and the highest T_c (≈97 K) of the single layer compounds, seem to be good candidates to achieve this goal. Moreover the critical temperatures of these compounds are the highest obtained to date. There are however some indications for intrinsic disorder in the Hg-O layer due to oxygen and mercury deficiencies [76, 75]. These systems have not been as extensively studied as other families because until recently sizeable single crystals were lacking. The group of Greven at Stanford has succeeded in growing large single crystals [76]. As grown samples are underdoped with a critical temperature of $T_c \approx 78$ K. Subsequently annealing these crystals in an oxygen atmosphere allows one to cover a wide doping range from strongly underdoped to overdoped. Typical susceptibility measurements of an as-grown and an annealed sample are shown in figure 3.2a.

Figure 3.2b shows the resistivity for these samples scaled to room temperature. The absolute value of the resistivity is difficult to determine due to the irregular sample shape. The as-grown sample is underdoped and indicates a pseudogap temperature around 280 K. This pseudogap temperature is determined as the temperature where the resistivity departs from linear behavior. This is more clearly visible from the resistivity measurements up to 400 K, see [75]. The optimally doped sample does not show an indication for a pseudogap temperature scale. These crystals have subsequently been studied with resonant inelastic x-ray scattering [77], ARPES [78] and recently inelastic neutron scattering [28].

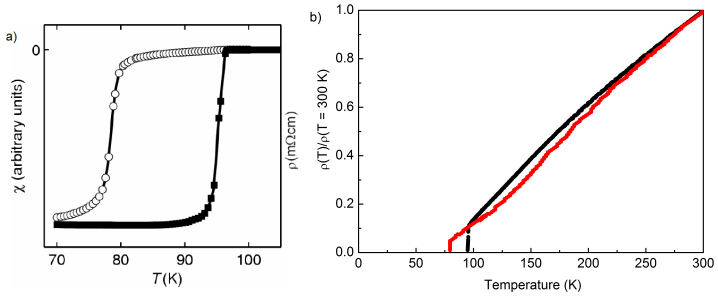

Figure 3.2: (a): Magnetic susceptibility and (b): resistivity measurements on as grown and annealed samples of Hg1201. Fig. (a) is adapted from [76]. The data in figure (b) was courteously provided by Barisic and Greven [75].

Before showing the results from these studies we now first discuss the optical experiments.

3.4 Sample

The sample used for the in-plane measurements is oriented with its largest surface along the a-b plane with dimensions of $1.1 \times 1.4 \times 0.5$ mm^3. Magnetic susceptibility measurements give a critical temperature $T_c \approx 97$ K with a somewhat broadened transition width of 5 K. The misorientation of crystallites is about 0.04° [76]. Hg-1201 is highly hygroscopic and does not cleave naturally along the ab-plane. Therefore we polished the sample with a 0.1 μm diamond abrasive in a pure nitrogen atmosphere before inserting it into the cryostat.

3.5 Reflectivity experiments

Figure 3.3 shows the in-plane reflectivity R$_{ab}(\omega)$ for selected temperatures. The reflectivity curves above 6000 cm^{-1} have been calculated from the dielectric function. Also shown is the reflectivity calculated from the pseudo dielectric function (see below). In addition, the c-axis reflectivity R$_c(\omega)$ was measured on the ac-plane of a different sample from 30 to 20000 cm^{-1} by C.C. Homes. Figure 3.4a shows the c-axis reflectivity for selected temperatures. The c-axis optical conductivity is obtained from a Kramers-Kronig (KK) transformation and is shown in figure 3.4b. In table 3.1 the oscillator parameters for the 5 phonon lines are summarized. From a simple counting of atoms 8 phonon modes are expected of which only four should be infrared active. Comparing with other cuprates we attribute the first two phonon lines to Hg and Ba vibrations, the mode at 355 cm^{-1} to vibration of the in-plane oxygens and the highest mode at 622 cm^{-1} with the vibration of the apical oxygen mode. The fact that this mode is split indicates that there is some oxygen disorder present. The additional weak structure seen between 200 cm^{-1} and 300 cm^{-1} is probably also due to disorder. Below T_c a Josephson plasma

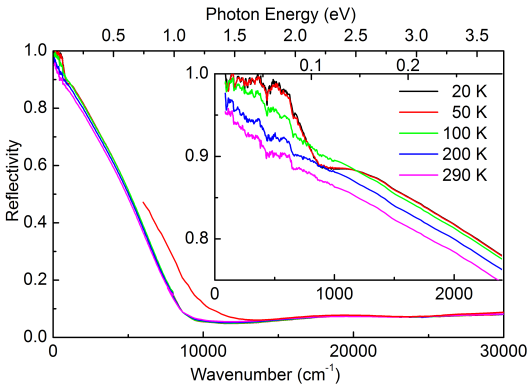

Figure 3.3: In-plane reflectivity for selected temperatures. The reflectivity above 6000 cm^{-1} has been calculated from the measured dielectric function. The thin red curve is the reflectivity at room temperature calculated from the pseudo dielectric function. The inset shows the far infrared reflectivity.

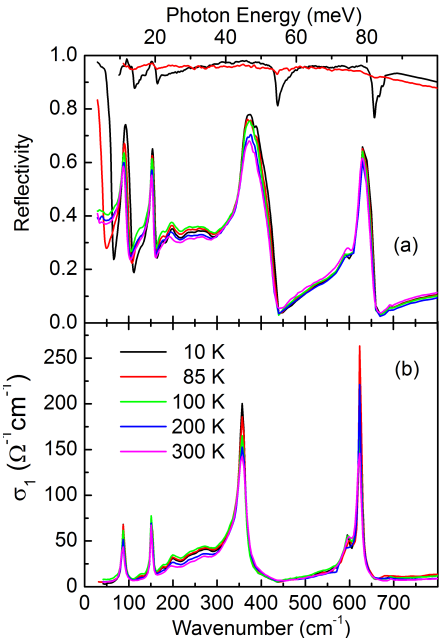

Figure 3.4: (a): Far infrared c-axis reflectivity at selected temperatures. Also shown is the in-plane reflectivity at 20 K measured with (red) and without polarizer (black). (b): The c-axis optical conductivity $\sigma_1(\omega)$. The temperatures are the same in all panels and are indicated in the inset in fig 3.4b.

edge appears that shifts with temperature to a maximum of around 70 cm^{-1} for the lowest measured temperature of 10 K.

A disadvantage of using a cut and polished surface as compared to a naturally cleaved one is the possible occurrence of a misorientation of the crystal axes relative to the sample surface. This results in the appearance of c-axis spectral features in the in-plane reflectivity spectra [79]. In figure 3.4a, R_{ab} measured with unpolarized light is shown. A comparison with R_c suggests that these features correspond to c-axis phonons. Also shown is a spectrum where a polarizer was oriented such that the spectral features observed in the first spectrum are minimized. Using the model of Ref. [79] the misorientation is estimated to be of the order of 3°. In order to suppress the c-axis phonon features in $R_{ab}(\omega)$, light polarized along the intersection of sample surface and ab-plane is used for the in-plane measurements. The features are not completely suppressed however, likely due to the finite angle of incidence (8°). This shows up in the optical conductivity and the extended Drude analysis below.

Another experimental issue is related to the absolute value of the in-plane reflectivity at low frequencies. In a metal for frequencies $\omega \ll 1/\tau$ one can use the Hagen-Rubens approximation [41] to describe the reflectance:

$$R(\omega) \simeq 1 - 2\left(\frac{2\omega}{\pi\sigma_0}\right)^{1/2}. \tag{3.1}$$

Here σ_0 is the dc conductivity. This is also expected to approximately hold for cuprates in the normal state and this approximation is frequently used to perform KK transformations of reflectivity spectra. In figure 3.5 the in-plane reflectivity plotted versus $(\omega/2\pi c)^{1/2}$ is shown for four different temperatures

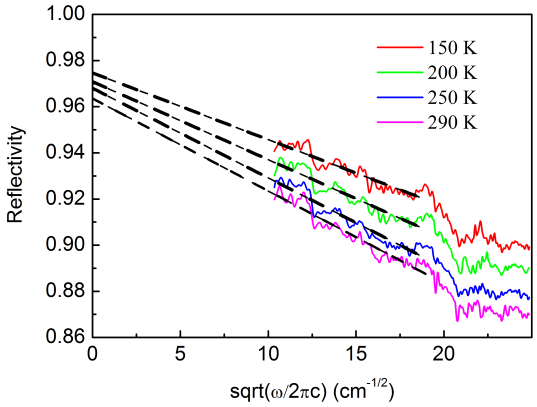

Figure 3.5: Reflectivity plotted versus $(\omega/2\pi c)^{1/2}$ and the fitted extrapolations (dashed) to zero frequency.

in the normal state. The extrapolations have been obtained by fitting Eq. 3.1 to the spectra between 100 cm^{-1} and 300 cm^{-1}. One can see that the reflectivity extrapolates to ≈ 0.97 instead of 1 for $\omega \to 0$. Since the curves all extrapolate to approximately the same value the difference is presumably due to the presence of a non-conducting secondary phase. From the fits we extracted the dc conductivity and compared the temperature dependence to resistivity measurements [75]. These two measurements correspond in absolute value and follow the same temperature dependence. However a problem arises when we try to model R$_{ab}$ with a Drude-lorentz model. For temperatures below T_c the fits show no sign of superconductivity. Instead of a delta function or very narrow Drude like contribution we find a rather broad Drude peak. Moreover the temperature dependence of the dc conductivity obtained from the model does not correspond with the resistivity measurements. We find that if we scale the in-plane reflectivity measurements upwards by 3% for all temperatures the dc conductivity extracted from the model closely follows the dc resistivity measurements and the Drude peak below T_c is replaced by a delta function.

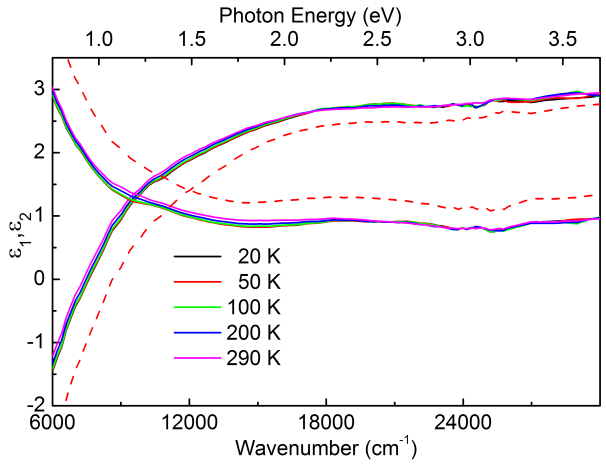

Figure 3.6: Dielectric function at selected temperatures corrected for the c-axis contribution using the method explained in the text. The pseudo dielectric function at room temperature is indicated by the broken thin red curves.

3.6 Ellipsometry

The ellipsometric measurements were performed with an angle of incidence of $60°$. Due to the large angle of incidence the measured pseudo dielectric function has an admixture of the c-axis component. The c-axis dielectric function derived from the c-axis reflectivity measurements was used to obtain the true in-plane dielectric function $\epsilon_{ab}(\omega)$, by an inversion of the Fresnel equations. The uncorrected dielectric function at room temperature and corrected dielectric function for several temperatures are shown in figure 3.6. Measurements were also performed for angles of incidence of $65°$, $70°$ and $80°$ and no dependence of the corrected $\epsilon_{ab}(\omega)$ on the angle was found showing the consistency of this procedure.

3.7 Optical conductivity

To extract the optical conductivity from the measured in-plane reflectivity and dielectric function a KK constrained variational analysis is used [80]. First, $R_{ab}(\omega)$ and $\epsilon_{ab}(\omega)$ are fitted simultaneously to a standard Drude-Lorentz model of which the parameters are given in table 3.1 for the room temperature spectra. Note that the last oscillator falls outside the measured spectral range. In a second step this model is then refined using multi-oscillator variational dielectric functions that fit all spectral details of $R_{ab}(\omega)$ and $\epsilon_{ab}(\omega)$. This approach improves the determination of the high frequency optical conductivity because the measured dielectric function in the visible light region is used to anchor the unknown phase of the reflectivity. The in-plane reflectivity measurements have been scaled upwards by 3% as explained above.

ϵ_∞	ω_o	ω_p	Γ	ω_o	ω_p	Γ
2.53	0	1.5	0.13	86	150	10
	0.48	1.34	0.9	151	140	5
	1.41	0.44	0.67	355	475	22
	2.51	1.54	1.78	595	300	35
	3.36	0.23	0.24	622	305	10
	4.87	3.92	2.21			

Table 3.1: Left: Oscillator parameters of the in-plane room temperature Drude-Lorentz model in eV (except ϵ_∞ which is dimensionless). Right: c-axis phonon parameters in cm^{-1}

In figure 3.7 the optical conductivity is shown for selected temperatures. It displays many of the features common to cuprates. At room temperature the low frequency spectrum is dominated by a Drude like peak that narrows when temperature is decreased. Below T_c a partial gap opens up followed by an onset in absorption that starts around 500 - 600 cm^{-1}. This value for the onset is comparable to optimally doped Bi-2212, YBCO and Tl-2201 [81] which all have approximately the same critical temperature but very different crystal structures indicating that this onset originates in the CuO_2 planes. Above 0.5 eV the optical conductivity is only weakly temperature dependent. We find evidence for at least three interband transitions with resonance energies of 1.41 eV, 2.51 eV and 3.36 eV. The latter two transitions have resonance energies close to resonances observed in the RIXS study of Ref. [77]. Unfortunately, the c-axis contamination of the in-plane spectra prevents us from making rigorous statements about any in-plane phonon features.

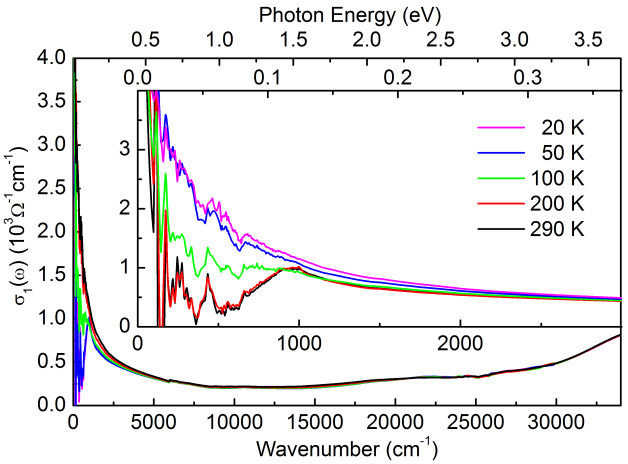

Figure 3.7: In-plane optical conductivity $\sigma_1(\omega)$ for selected temperatures. The inset shows the low frequency part on an expanded scale. Some sharp structures in the region below 700 cm^{-1} are due to the remnants of the c-axis phonons.

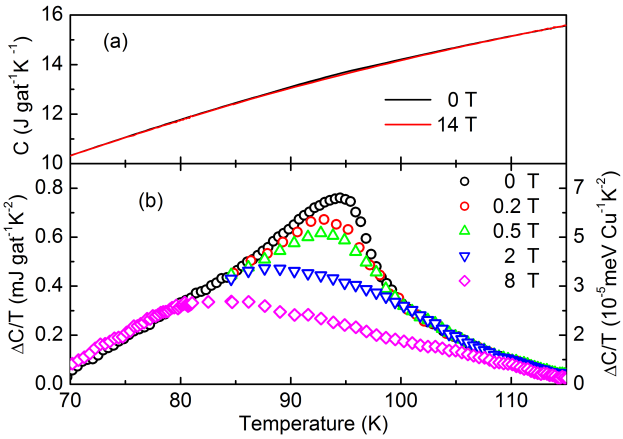

Figure 3.8: Difference of the specific heat data $\Delta C/T = (C(B,\mathrm{T}) - C(14T,\mathrm{T}))/T$ for a number of magnetic fields B showing the anomaly at the superconducting transition.

3.8 Specific heat measurements

Specific-heat measurements have been performed in magnetic fields up to 14 T on a small piece broken from the crystal used for the optical measurements with a mass of $\sim$700 μg. The magnetic fields used in these measurements are oriented perpendicular to the Cu-O planes. Since the specific heat is a probe of bulk thermodynamic properties the measurements confirm the bulk nature of the superconducting transition. It also gives an estimate of the strength of thermal fluctuations and of the superconducting condensation energy. A micro-relaxation calorimeter adapted to the small size of the crystal was used. Data has been taken using a generalized long relaxation method as described elsewhere [82]. This method gives a high precision in the determination of absolute values and a sensitivity comparable to that of standard AC methods as used in previous publications on Hg-1201 [83]. The absolute error is estimated as 5 % due to the mass of the thermal compound used to mount the small sample. This does not enter into relative measurements when data taken in a magnetic field is used as a background. In figure 3.8a we show two representative specific heat curves measured in fields of 0 T and 14 T. Figure 3.8b shows the difference $\Delta C/T$ between measurements taken in a field B and that taken in a field of 14 T in C/T. Due to the much higher upper critical field, subtracting data taken in a 14 T field does not provide the exact compensation of the phonon background but helps to investigate the shape and size of the anomaly. Note that the anomaly is only 0.4 % of the total specific heat and thus particularly small as compared to other cuprate superconductors.

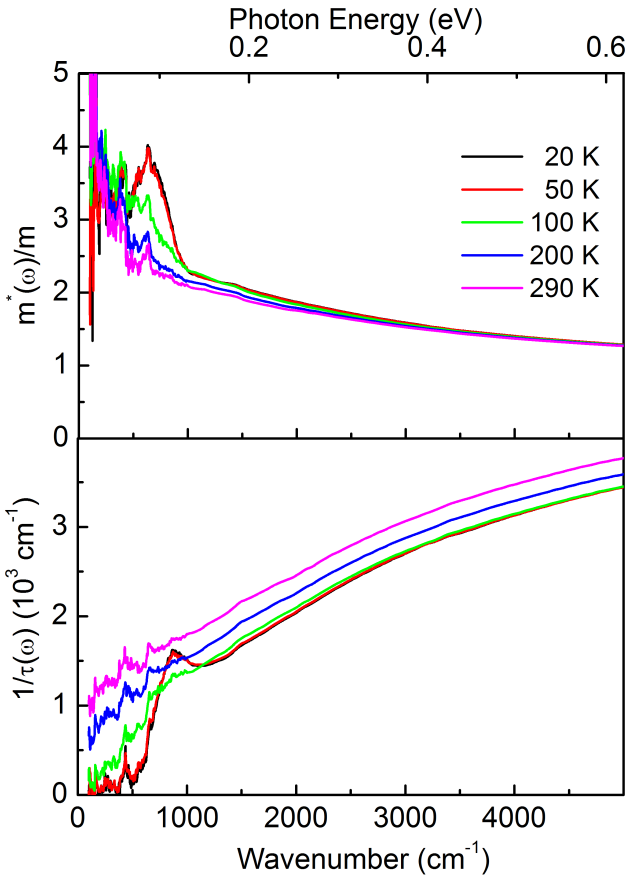

Figure 3.9: The frequency dependent scattering rate and effective mass of Hg-1201. The small peak in $m^*(\omega, T)/m_b$ at ≈ 620 cm^{-1} for temperatures above T_c is due to the remnant phonon structure.

3.9 Extended Drude analysis

Figure 3.9 shows $1/\tau(\omega)$ and $m^*(\omega)/m_b$ for selected temperatures derived from the optical conductivity as discussed in chapter 2.4.4. The scattering rate is strongly suppressed below 600 cm^{-1} for temperatures below T_c indicative of the opening of a gap. ARPES measurements on Hg-1201 show a maximum gap value of 30 meV, but there is some uncertainty in this value because no quasiparticle peak is observed around the anti-nodal direction [78]. From the optical measurements it is difficult to extract the gap value: simple s-wave BCS superconductors in the dirty limit show an onset in absorption associated with the superconducting gap at 2Δ. This onset is shifted to $2\Delta + \Omega_{ph}$, with Ω_{ph} a phonon resonance energy, if the coupling to phonons is included. It has been suggested that the onset seen in cuprates is shifted due to the interaction of the electrons with the magnetic resonance mode [84] by Ω_{mr} to $2\Delta + \Omega_{mr}$. The onset here is defined as the point where the rise in $1/\tau(\omega)$ is steepest. This corresponds by KK relations to a maximum in $m^*(\omega)/m_b$. Using the values $\Omega_{mr} \approx 52 \pm 20$ meV [76] and $\Delta_0 \approx 30 \pm 10$ meV [78] we find $2\Delta + \Omega_{mr} \approx 110 \pm 30$ meV (900 ± 240 cm^{-1}), which is

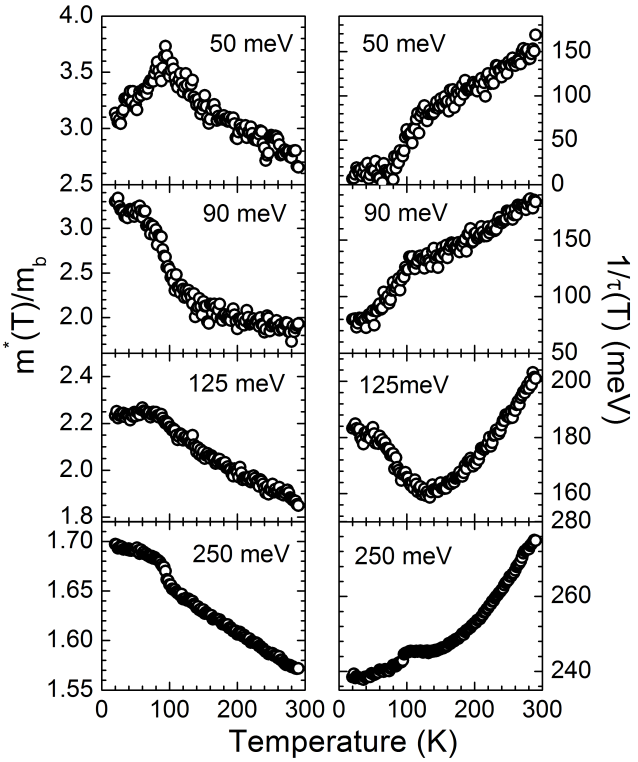

Figure 3.10: Temperature dependence of $1/\tau(\omega, T)$ and $m^*(\omega, T)/m_b$ for selected energies. Both quantities show a clear departure from the normal state trend at T_c.

of the same order of magnitude as our experimental value of 80 ± 5 meV.

In figure 3.10 the temperature dependence of $1/\tau(\omega, T)$ and $m^*(\omega, T)/m_b$ is shown for selected photon energies. In the normal state, the temperature dependence of $1/\tau(\omega, T)$ for small photon energies is linear in temperature but this linearity is lost for photon energies larger than $\hbar\omega > 0.1$ eV. The scattering rate shows a sharp drop at T_c for all photon energies except in a narrow window between 95 and 140 meV where the scattering rate increases below T_c. It has a maximum increase around 110 meV. The temperature dependence of $m^*(\omega, T)/m_b$ becomes roughly linear above $\hbar\omega > 0.1$ eV and shows an increase when the system becomes superconducting over most of the frequency range, except below 55 meV where it decreases.

3.10 Superfluid density

The in-plane condensate strength $\rho_s = \omega_{p,s}^2$ is determined in two ways. The first method is to fit the low temperature spectrum with a Drude-Lorentz model. In such a model the superfluid density is represented by a δ-peak at zero frequency with strength $\omega_{p,s}^2$. The value obtained from this method is $\omega_{p,s}$ = 9600 $\pm$ 400 cm^{-1} (1.2 ± 0.05 eV). The error bar on this quantity is determined by shifting the reflec-

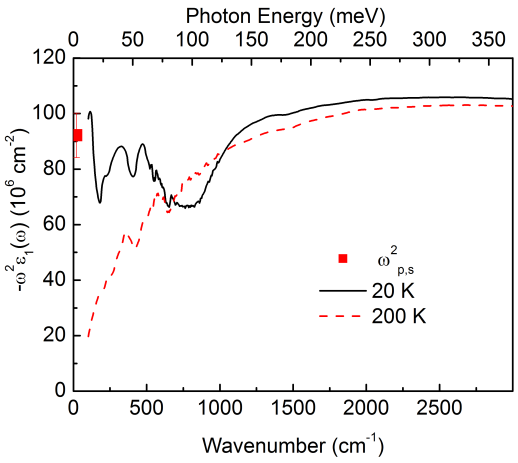

Figure 3.11: $-\omega^2\epsilon_1(\omega)$ plotted at 20 K and 200 K . Extrapolating the 20 K curve to $\omega = 0$ agrees with the value $\omega_{p,s}$ = 9600 $\pm$ 400 cm^{-1} found from the Drude-Lorentz fit of the spectrum indicated by the square at ω= 0.

tivity up and down by 1 % and observing the subsequent change in $\omega_{p,s}$. The corresponding values for Bi-2212 [45] and Bi-2223 [47] are $\omega_{p,s}$ = 9500 cm^{-1} and $\omega_{p,s}$ = 10300 cm^{-1} respectively. The second method relies on the assumption that the real part of the dielectric function in the superconducting state is dominated at low frequencies by the superfluid density,

$$\epsilon_1(\omega) \approx -\frac{\omega_{p,s}^2}{\omega^2} \tag{3.2}$$

Since $\epsilon_1(\omega)$ has been determined in a model independent way this result is more reliable. In figure 3.11 the function $-\omega^2\epsilon_1(\omega)$ is shown. The extrapolation to zero frequency of this function matches well with the value obtained with the Drude-Lorentz fit. It is interesting to use the value for $\omega_{p,s}$ extracted from the in-plane measurements and from c-axis measurements to check the scaling relation $\rho_s \propto \sigma_{dc}T_c$ [85]. This has already been done for the c-axis measurements in Ref. [85]. From a Drude-Lorentz fit to the c-axis data a value of $\omega_{p,s} \approx 290 \pm 10$ cm^{-2} is found, more than a factor of 30 different from the in-plane value. At the same time from an extrapolation $\omega \rightarrow 0$ we find $\sigma_{1,c}(\omega \rightarrow 0, T \simeq T_c) \approx 7\ \Omega^{-1}$cm^{-1} for the c-axis and $\sigma_{1,ab}(\omega \rightarrow 0, T \simeq T_c)$ ≈8300 Ω^{-1}cm^{-1}. Put together we find $N_c \simeq 4.6\sigma_{dc}T_c$ and $N_{ab} \simeq 4.3\sigma_{dc}T_c$ in good agreement with the scaling trend observed in Ref. [85].

3.11 Low frequency spectral weight

In recent years there has been a lot of interest in the temperature dependence of the low frequency integrated spectral weight,

$$W(\Omega_c, T) = \int_0^{\Omega_c} \sigma_1(\omega, T) d\omega \approx \frac{\pi e^2 a^2}{2\hbar^2 V} < -\widehat{T} >, \tag{3.3}$$

where *a* is the in-plane lattice constant, *V* the unit cell volume and $\widehat{T}$ the kinetic energy operator. Ω_c is a cut off frequency chosen to approximately separate the intraband and interband transitions. In a nearest neighbor tight binding model the relation between W(Ω_c,T) and $< -\widehat{T} >$ is exact. More recently it has been shown that this relation still holds approximately in the doping range under consideration [86]. As discussed in section 2.4.3, the observation that in the cuprates there is a superconductivity induced increase of spectral weight contrary to expectations from BCS theory has sparked a lot of interest. A qualitative indication of the superconductivity induced changes of low frequency spectral weight can be obtained from the dielectric function measured directly with ellipsometry. This can be done by monitoring the shift of the screened plasma frequency $\omega_p^* = \omega_p/\sqrt{\epsilon_\infty}$, *i.e* the frequency for which $\epsilon_1(\omega) = 0$, with temperature. Although it gives a first indication, it does not give a definite answer since ω_p^* can be influenced by other factors, for instance the temperature dependence of the interband transitions. In figure 3.12, ω_p^* is plotted versus T^2. The screened plasma frequency shows an extra blueshift below T_c, suggesting an increase of the low frequency spectral weight. Note that the absolute value of ω_p^*($\approx$ 7300 cm^{-1} at room temperature) is smaller than the one observed for optimally doped Bi-2212 [45] ($\approx$ 7600 cm^{-1}) and Bi-2223 [47] ($\approx$ 8100 cm^{-1}) which can be related to a smaller volume density of CuO_2 planes. In contrast to earlier observations ω_p^* shows a deviation from the T^2 behavior already in the normal state.

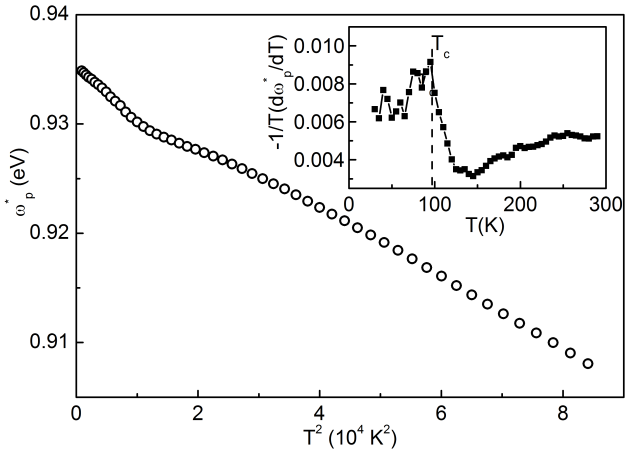

Figure 3.12: Screened plasma frequency ω_p^* versus T^2. The relative error bars on this quantity are comparable to the size of the points. The inset shows the derivative.

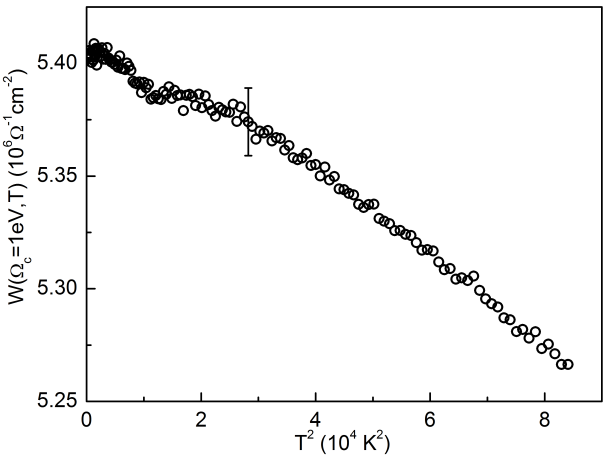

Figure 3.13: Integrated spectral weight for a cut off Ω_c = 1 eV. The error bar indicates the estimated error due to the extrapolations used.

To calculate the integral in Eq. 3.3 one formally has to integrate from $\omega = 0$. Therefore to do the integration one has to rely on an extrapolation of the reflectivity to zero frequency. It has recently been shown that the superconductivity induced increase of spectral weight and absolute value of $W(\Omega_c, T)$ are rather insensitive to this extrapolation, provided one also uses the information contained in $\sigma_2(\omega, T)$ [47, 87]. Figure 3.13 shows the integrated spectral weight using Eq. 3.3 with the cut off Ω_c = 1 eV. One would like to choose Ω_c such that it separates the free carrier response from the bound charge response. This is strictly speaking not possible because in most cuprates the two regions overlap. Therefore the cut off is chosen in a region where the superconductivity induced change of spectral weight is more or less constant (figure 3.15c). In chapter 6 we will have more to say on the temperature dependence introduced by choosing a finite cutoff. By extrapolating the normal state trend to $T = 0$, the superconductivity induced increase of spectral weight is estimated to be $\Delta W \approx 1.5 \pm 1 \cdot 10^4\ \Omega^{-1}$ cm^{-2} which is 0.5 $\%$ of the total spectral weight. A remark has to be made here on the temperature dependence of $W(\Omega_c, T)$. The temperature dependent reflectivity measurements show a hysteresis between curves measured cooling down and curves measured warming up for frequencies between 3000 cm^{-1} and 7000 cm^{-1}. This hysteresis is probably caused by a small amount of gas absorption on the sample surface. This has the effect of suppressing the reflectivity in this range below 150 K with a maximum suppression at 20 K of about 0.5 $\%$. This trend was not observed in the ellipsometric data in the region of overlap. The upward kink at T_c is not affected by this, but the deviation from T^2 behavior below 150 K could be a result of this. Note that $W(\Omega_c, T)$ closely follows $\omega_p^*(T)$, so the temperature dependence of $W(\Omega_c, T)$ is probably not too much affected. In several other cuprates the temperature dependence of the normal state optical spectral weight is quadratic. Here we observe this quadratic temperature dependence only for temperatures higher than 170 K. The coefficient of this quadratic part

has been observed to be unexpectedly large and was initially believed to be due to correlation effects [65]. In chapter 6 we show that this coefficient can be understood to arise from a cutoff effect. There we also show that within the same model the quadratic temperature dependence is only approximate. To compare the superconductivity induced increase of $W(\Omega_c, T)$ to other compounds we express ΔW in meV/Cu. We find ΔW ≈0.5 meV/Cu. This is a factor of 2 smaller than observed for Bi-2212 [45] and a factor of 4 smaller than the one for Bi-2223 [47].

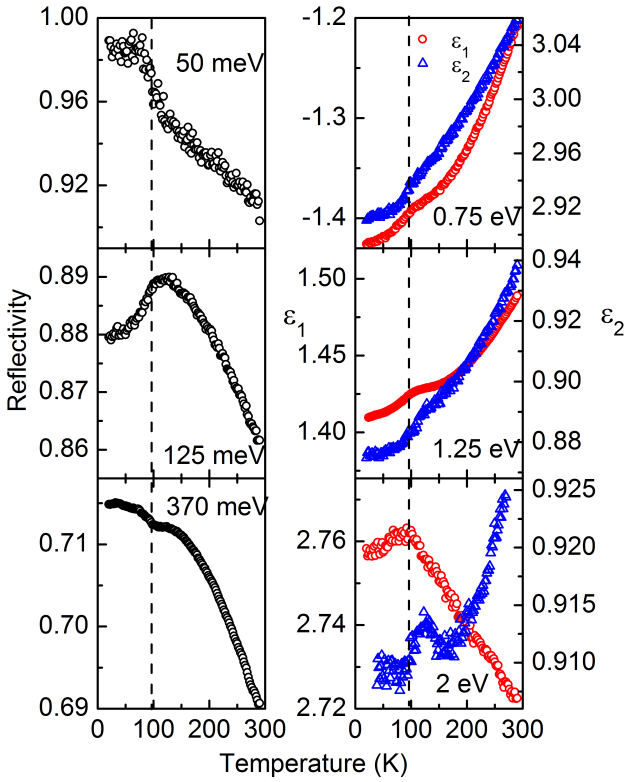

Figure 3.14: Temperature dependencies of the in-plane reflectivity and dielectric function for selected energies. The dashed lines indicate T_c.

In order to separate the superconductivity induced changes from the temperature dependence of the normal state it is necessary to measure the changes in the optical constants as a function of temperature. Because the superconducting transition is second order, the superconductivity induced changes appear as a kink at T_c as can be seen in figure 3.14. A determination of the superconductivity induced spectral weight transfer by analysis of slope changes at T_c is more reliable since this method is much less sensitive to systematic errors in the absolute value of reflectivity. The details of this analysis are explained in Ref. [56]. The slope change at T_c for any optical quantity *f(ω,T)* is defined as [56],

$$\Delta_s f(\omega) = \left(\frac{\partial f(\omega,T)}{\partial T}\right)_{T_c+\delta} - \left(\frac{\partial f(\omega,T)}{\partial T}\right)_{T_c-\delta}. \tag{3.4}$$

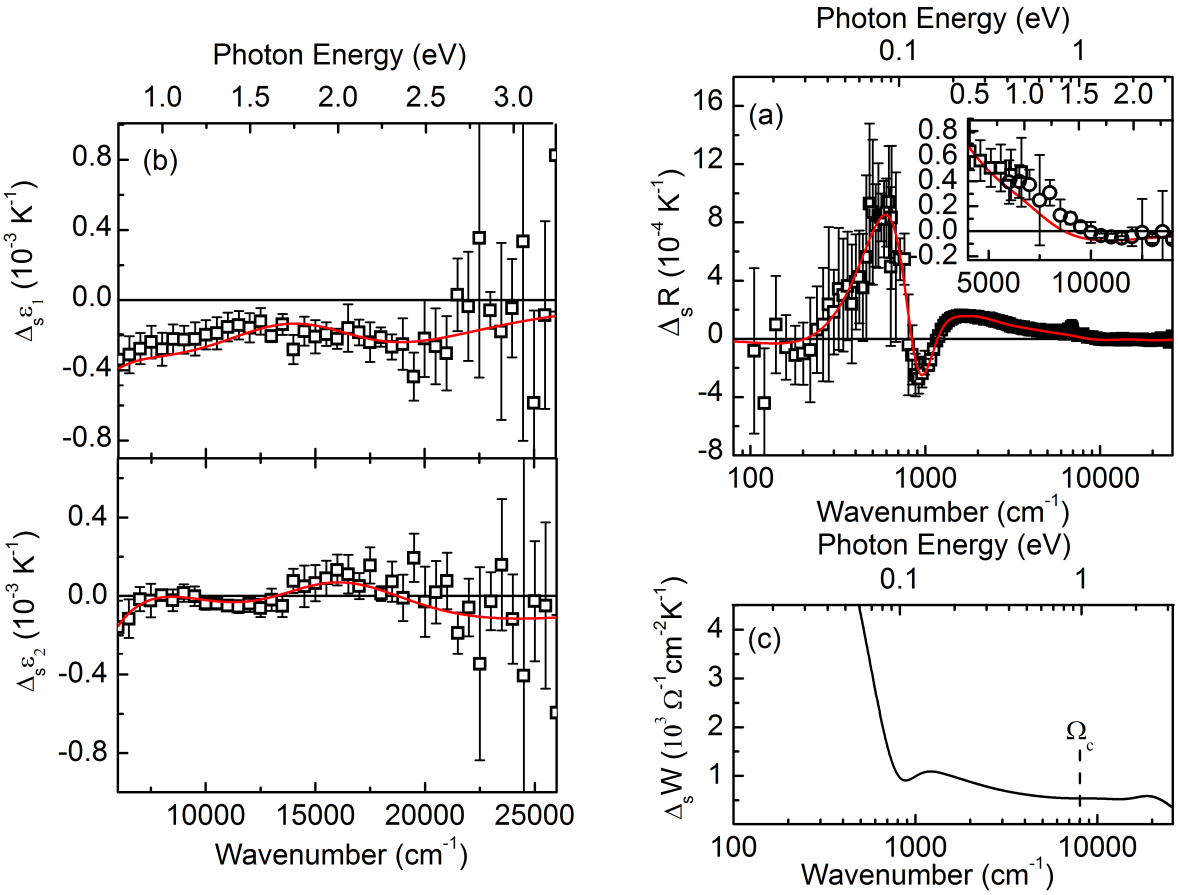

Figure 3.15: Spectral dependence of (a): $\Delta_s R$ (squares), (b): $\Delta_s \epsilon_{1,2}$ (squares). Solid lines in (a) and (b) are the fits of the $\Delta_s R$ and $\Delta_s \epsilon_{1,2}$ spectra. The inset in (a) shows the excellent match between the directly measured $\Delta_s R$ (squares) and the $\Delta_s R$ calculated from $\Delta_s \epsilon_{1,2}$ (circles). (c): $\Delta_s W$ calculated from the best fit to $\Delta_s R$ and $\Delta_s \epsilon_{1,2}$ using Eq. 3.6. The observed spectral weight increase is $\Delta_s W(\Omega_c) = +540$ $\Omega^{-1}\text{cm}^{-2}K^{-1}$. The dashed line indicates the cut off frequency used to calculate W(Ω_c,T).

Since the slope changes are smeared due to fluctuations, the derivatives correspond to average values in certain regions δ above and below T_c. For this analysis one needs temperature dependencies with a dense sampling in temperatures. Figure 3.14 shows the measured temperature dependencies for selected photon energies. From these temperature dependencies the slope change at T_c can be estimated. Since numerical derivatives of the data are very noisy, the temperature dependencies are fitted above and below T_c to a second order polynomial [56]. The derivatives are then simply calculated from the analytical expressions. Figure 3.15 shows the slope change of the reflectivity and the dielectric function at T_c. The functions $\Delta_s R(\omega)$, $\Delta_s \epsilon_1(\omega)$ and $\Delta_s \epsilon_2(\omega)$ were obtained by fitting the data (figure 3.14) between 40 K and T_c (= 97 K) and between T_c and 200 K. The error bars were estimated by varying the upper and lower limits for both the high and low temperature fits.

From the inset of figure 3.15a one can see the good agreement between the slope change estimated

from reflectivity and ellipsometric measurements. Spectra of $\Delta_s\epsilon_1$ and $\Delta_s\epsilon_2$ satisfy KK relations, therefore $\Delta_s\epsilon$ can be modeled with an oscillator model that has the same functional form as a Drude-Lorentz model,

$$\Delta_s\epsilon = \Delta_s\epsilon_\infty + \sum_{i=0}^{N} \frac{A_i}{\omega_i^2 - \omega^2 - i\gamma_i\omega} \tag{3.5}$$

where $\Delta_s\epsilon_\infty$ is the change in the high energy contribution, ω_i is the center frequency of the *i*th oscillator, γ_i is its width and A_i is the oscillator strength. The difference with a normal Drude-Lorentz model is that the oscillator strength can take on both positive and negative values corresponding to the addition or removal of spectral weight. $\Delta_s\sigma(\omega)$ is easily calculated from $\Delta_s\epsilon$ and the slope difference integrated spectral weight is then defined as,

$$\Delta_s W(\Omega_c) = \frac{A_0}{8} + \int_{0+}^{\Omega_c} \Delta_s\sigma_1(\omega)d\omega \tag{3.6}$$

with A_0 the condensate strength. This quantity is displayed in figure 3.15c. The result gives $\Delta_s W(\Omega_c) = +540\ \Omega^{-1}\text{cm}^{-2}K^{-1}$ for a cut off $\Omega_c \approx 1$ eV. This result is somewhat lower than that for Bi-2212 ($\Delta_s W(\Omega_c) = +770\ \Omega^{-1}\text{cm}^{-2}K^{-1}$) [56] and Bi-2223 ($\Delta_s W(\Omega_c) = +1100\ \Omega^{-1}\text{cm}^{-2}K^{-1}$) [47] but has the same sign and order of magnitude. It is also possible to calculate $\Delta_s W(\Omega_c)$ directly from the measured temperature dependence of $W(\Omega_c, T)$, by fitting $W(\Omega_c, T)$ in exactly the same way as is done for the other optical quantities. The result obtained in this way is $\Delta_{s,direct} W(\Omega_c) = +420\pm150$ $\Omega^{-1}\text{cm}^{-2}K^{-1}$ which is a little bit lower but consistent with the result obtained using the temperature modulation analysis.

3.12 Specific heat anomaly

Figure 3.8b shows specific-heat data taken in different magnetic fields after subtracting the 14 Tesla data as a background. The specific heat in zero field clearly shows an asymmetric lambda shape typical for a superconducting transition governed by thermal fluctuations of the anisotropic 3D-XY universality class [88, 89]. The shape of the anomaly shows more resemblance to that of optimally doped YBCO [90] than to that of the more two dimensional Bi-2212 which shows a symmetric anomaly [91]. As in YBCO [90], the peak is clearly shifted to lower temperatures in a magnetic field. This shift is well described in the framework of 3D-XY fluctuations [89]. A contribution due to fluctuations can be seen up to $\sim$15 K above T_c. Since a 14 T field is by far not enough to suppress all pair correlations above T_c, there probably also is a contribution at higher temperatures which can not be observed with this method [88, 92]. The influence of a magnetic field on the fluctuations is to introduce a magnetic length $l = (\Phi_0/B)^{1/2}$ closely related to the vortex-vortex distance which reduces the effective dimensionality [92, 89]. In the critical 3D-XY regime, the correlation length diverges upon

approaching T_c following a power law of the form $\xi \sim \xi_0(1-t)^{-\nu}$ with $t = T/T_c$ and ν=0.67 for the 3D-XY universality class. The presence of a magnetic length scale cuts off this divergence within a certain temperature window and thus broadens the transition in a field as seen in the specific heat data. The superconducting transition is thus far from being a BCS type transition where the transition temperature is reduced in a field because the Cooper pairs are broken up. Here T_c is rather a phase-ordering transition comparable to that of superfluid 4He, albeit with a clear anisotropy. Due to the lack of the exact phonon background it is not possible to estimate up to which temperatures fluctuations due to phase correlations of preformed Cooper pairs exist. However, it should be noted here that no anomaly at higher temperatures is visible, suggesting a rather continuous evolution of pair correlations at higher temperatures with a continuous opening of a superconducting gap far above T_c, whereas the lifetime of phase fluctuations is finite [34]. An interesting point is that a field of 14 T has a clear influence on the fluctuations above T_c (between 100 K and 115 K), while no effect of an applied field has been reported for YBCO [90]. This suggests a stronger pair breaking effect by a magnetic field and thus points to a smaller upper critical field in this compound. In a BCS type superconductor the specific heat in the normal and the superconducting state is used to evaluate the thermodynamic critical field $H_c(T)$ which is a measure of the condensation energy. In the presence of fluctuation contributions it has been argued that fluctuation contributions above T_c have to be considered to calculate the real condensation energy [93]. As the true phonon background is unknown here this calculation cannot be performed. Information can be obtained by comparing the size of the specific heat anomaly with that of other cuprate superconductors having a similar T_c. Nevertheless the specific heat jump $\Delta C = 0.052$ J gat^{-1} K^{-1} can be compared to $\Delta C = 0.2$ J gat^{-1} K^{-1} found for optimally doped Bi-2212 [91] and $\Delta C = 0.46$ J gat^{-1} K^{-1} for overdoped YBCO [90] (the abbreviation gat stands for gramatom). The large difference to the value found in YBCO can be explained by the larger contribution of fluctuation above T_c in Hg-1201 (and Bi-2212) which appears to have a larger anisotropy and thus more 2D correlations above T_c. A large part of the condensation energy can thus be attributed to the smooth onset of 2D correlations of Cooper pairs far above T_c. The anomaly which is visible at T_c represents thus only a small part of the condensation energy [93]. If the units eV/K and data normalized per Cu-atom are used, the single layer compound can be compared to the 2-layer compound Bi-2212. This leads to ΔC=4.3·10^{-3} meV K^{-1} per copper for Hg-1201 which is 3.5 times smaller than the value found for optimally doped Bi-2212 ΔC=1.5·10^{-2} meV K^{-1} per copper.

From the specific heat we estimate the change in internal energy by integrating,

$$\Delta U(T) = \int_0^T [C(0T, T') - C(14T, T')]dT' \tag{3.7}$$

Figure 3.16 shows a comparison between the internal energy relative to 60 K and the kinetic energy relative to 20 K defined as $\delta W(T) = W(\Omega_c, T = 20K) - W(\Omega_c, T)$. We find that $\delta W(T)$ is about

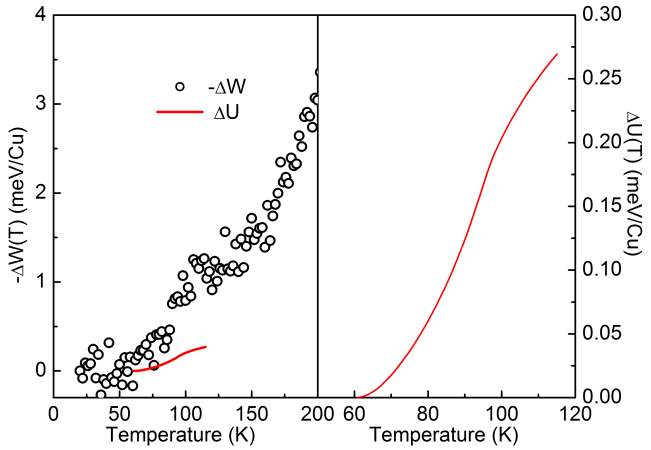

Figure 3.16: Comparison between the kinetic energy relative to 20 K, $\delta W(T) = W(\Omega_c, T = 20K) - W(\Omega_c, T)$ on the left and the internal energy $\Delta U(T)$ relative to 60 K on the right. The red line in the left panel is $\Delta U(T)$ plotted on the same scale as $\delta W(T)$.

3 times larger than the $\Delta U(T)$, so in principle $\delta W(T)$ is large enough to account for the condensation energy. We note again that the change in internal energy is probably only a small part of the condensation energy because the fields used here are by far not enough to completely suppress superconductivity. The temperature dependence of δW around T_c is much more gradual than the one for ΔU. Because of the better signal-to-noise ratio of the specific heat data it is possible to observe the change in internal energy due to the phase ordering transition as a rather sharp step at T_c. Superimposed on this is the much more gradual change due to the 2d fluctuations. Since the phase ordering transition occurs in a narrow window around T_c and contributes only a small part of the change in internal energy, we are probably not able to observe this change in $\delta W(T)$.

Chapter 4

Doping dependent optical properties of $Bi_2Sr_2CuO_{6+\delta}$.

4.1 Introduction

While $HgBa_2CuO_{4+\delta}$ is a prototypical high T_c superconductor, $Bi_2Sr_2CuO_{6+\delta}$ is probably the exact opposite. The pure compound has a strong structural modulation due to the lattice mismatch between the rocksalt and Cu-O layers. This modulation can be reduced by substituting Sr with La. Further substitution of Bi by Pb almost completely removes the modulation. However the introduction of Pb and La occurs at random sites and this introduces another form of disorder. The critical temperature is raised by this process from $T_c \approx 11$ K to $T_c \approx 41$ K for optimally doped samples. This critical temperature is similar to $La_{2-x}Sr_xCuO_{4+\delta}$ that also shows strong disorder on the La site. In contrast $HgBa_2CuO_{4+\delta}$ has only a weak disorder on the Hg site and a two times higher critical temperature. This is an indication that disorder in the rocksalt layers plays an important role in determining the critical temperature of these materials. The interest in these materials has been small because of the low critical temperature and presence of the structural modulation mentioned above. The improvements in crystal quality have pushed several groups to investigate these compounds. Recently there have been several reports including ARPES experiments [94, 95, 96], inelastic x-ray scattering [97] and μSR experiments [98]. Optical properties of Bi2201 have been published before [99, 100]. In this section I will discuss the optical experiments for four Pb and La substituted Bi2201 samples. They cover a broad doping range and the optical properties show a strong doping dependence.

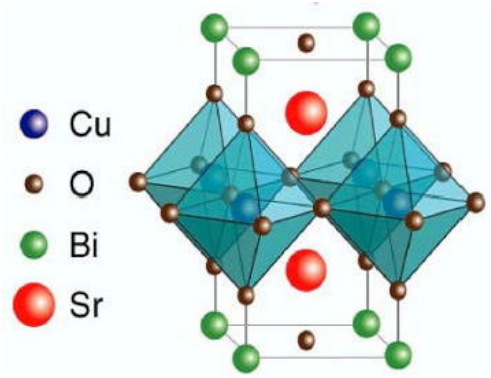

Figure 4.1: Crystal structure of Bi2201. The Pb atoms predominantly substitute on the Bi site while the La replaces Sr. Figure adapted from H. Eisaki.

4.2 Samples

he properties of four samples of Pb and La substituted Bi2201 are studied: $Bi_2Sr_{1.25}La_{0.75}CuO_{6+\delta}$ (UD0, $T_c = 0$ K), $Pb_{0.5}Bi_{1.55}Sr_{1.2}La_{0.8}CuO_{6+\delta}$ (UD10, $T_c = 10$ K), $Pb_{0.55}Bi_{1.5}Sr_{1.6}La_{0.4}CuO_{6+\delta}$ (OpD35, $T_c = 35$ K) and $Pb_{0.38}Bi_{1.74}Sr_{1.88}CuO_{6+\delta}$ (OD0, $T_c = 0$ K). The crystal structure of these materials is shown in figure 4.1.

4.3 Normal incidence reflectivity.

Reflectivity spectra are shown in Fig. 4.2 for all four samples at three temperatures: T =10 K, 100 K and 290 K. The reflectivity data is characteristic of a bad metal and shows a strong doping dependence. With increasing doping the metallicity increases and the reflectivity increases accordingly. As a result the sharp phonon structures that can be clearly seen in the UD0 sample (top right panel) become progressively more screened and are hardly visible in the OD0 spectra. The metallicity manifests itself in a dependence on frequency that follows the Hagen-Rubens trend $R(\omega) = 1 - 2\sqrt{2\rho_{dc}\omega/\pi}$ for frequencies below 200 cm^{-1}. We made fits to the low frequency reflectivity using the Hagen-Rubens expression to estimate the d.c. resistivity. The values obtained in this way are in agreement with those reported in the literature for similar doping values [101, 102] and the fits extrapolate to $R(\omega \rightarrow 0)$ = 1 within our experimental uncertainty ($\pm$ 0.5 %). The exception is the UD0 sample. On a qualitative level the reflectivity looks similar to that of a disordered metal (for an example see Ref. [103]). The temperature dependence is also somewhat different from the other samples: the reflectivity increases with decreasing temperature but below 10 meV the reflectivity first shows a small increase and then starts to decrease for temperatures below about 100 K.

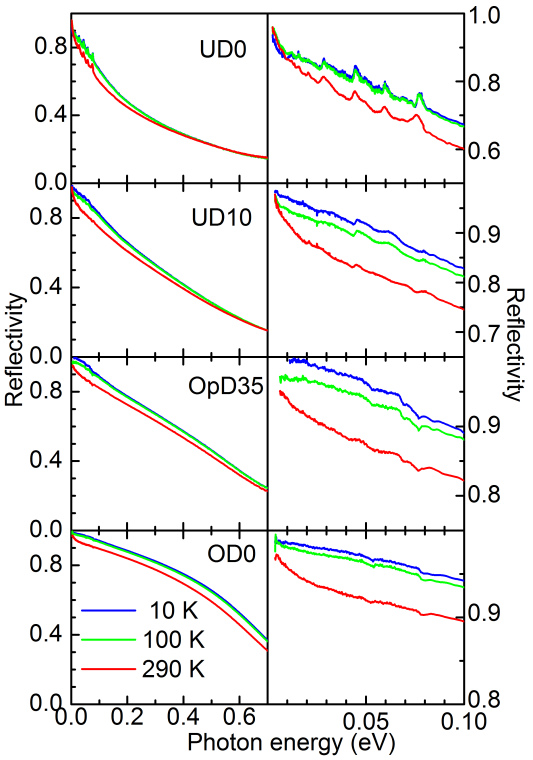

Figure 4.2: Reflectivity for 4 different dopings of Bi-2201 at T = 10, 100 and 290 K. From top to bottom UD0, UD10, OpD35 and OD0 samples. The left hand panels show the reflectivity on a large scale while the right hand panels show the FIR range on an enlarged scale.

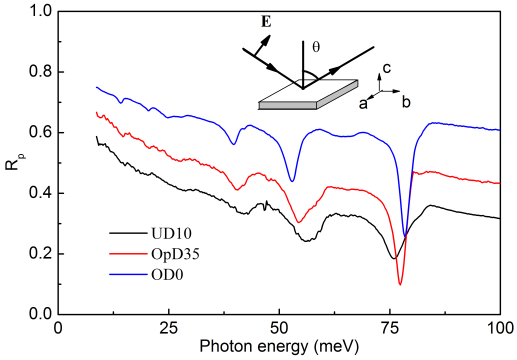

Figure 4.3: Grazing incidence reflectivity for the UD10, OpD35 and OD0 samples at room temperature. The inset shows the experimental configuration for the grazing incidence experiment.

4.4 Grazing incidence reflectivity

The grazing incidence reflectivity, $R_p(\omega)$, is measured using polarized light with the polarization parallel (p-polarized light) to the plane of incidence (see inset of figure 4.3). This orientation of the polarization gives a finite projection of the electric field along the c-axis depending on the angle of incidence and this gives us the information about the c-axis optical properties. The angle of incidence in our case is 79 degrees. Combining this experiment with the normal incidence experiment described above we can solve the Fresnel equations for anisotropic media to obtain the c-axis loss-function [104, 100]. An important aspect of the grazing incidence technique is that the required reference measurement on an *in-situ* evaporated gold layer is also measured under grazing incidence. $R_{p,gold}(\omega)$ is significantly different from the normal incidence reflectivity of gold. In order to get the correct absolute value of $R_p(\omega)$ for the sample we determined the optical constants of the gold layer using ellipsometry between 0.6 and 4 eV. Since gold is a simple metal we can extrapolate $R_{p,gold}(\omega)$ to

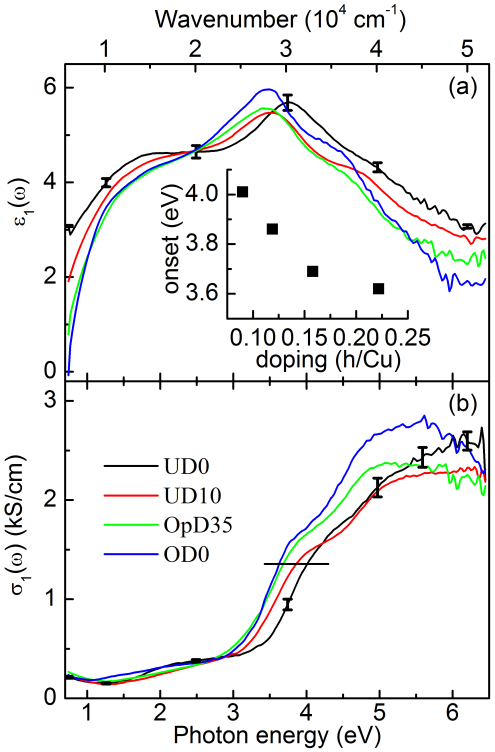

Figure 4.4: (a): Real part of the dielectric function, $\varepsilon_1(\omega)$. The inset shows the doping dependence of the energy of the interband transition. (b) Imaginary part of the dielectric function, $\varepsilon_2(\omega)$. We only display room temperature spectra, since the temperature dependence for these frequencies is too weak to be discernable at this scale. The error bars shown for the UD sample are systematic error bars and are representable for all three samples. The inset shown in the top panel shows the strong doping dependence of the 4 eV peak in $\sigma_1(\omega)$. The points correspond to the energy where the experimental curves intersect the horizontal line in the lower panel.

the far infrared region with the knowledge of the plasma frequency and scattering rate obtained from this experiment. The grazing incidence reflectance for the sample is then given by $R_{p,sample}(\omega) = R_{p,meas.}(\omega) \cdot R_{p,gold}(\omega)$, where $R_{p,meas}(\omega)$ is the measured grazing reflectance.

Figure 4.3 shows $R_p(\omega)$ for the UD10, OpD35 and OD0 samples. The doping dependence in the absolute value of $R_p(\omega)$ can be shown to arise from the doping trend of the in-plane dielectric function (section 4.7). The large structures are c-axis optical phonons.

4.5 Ellipsometry

Ellipsometric measurements give direct access to the complex pseudo-dielectric function, $\hat{\varepsilon}_{pseudo}(\omega)$, that corresponds closely to $\hat{\varepsilon}_{ab}(\omega)$ with a weak admixture of the c-axis component. Correspondingly, the transformation from $\hat{\varepsilon}_{pseudo}(\omega)$ to $\hat{\varepsilon}_{ab}(\omega)$ using the Fresnel equations gives rise to a small cor-

rection for the c-axis admixture in this frequency range. This has been verified for several high T_c cuprates with roughly the same optical constants [47, 50]. The c-axis dielectric function is almost constant between 1.25 eV and 3 eV and equals roughly 4.1 for Bi2223 and 4.0 for Hg-1201. The analysis of the grazing reflectivity data indicates a c-axis dielectric constant for Bi2201 $\hat{\varepsilon}_c \approx 4.4$, which we use to correct $\hat{\varepsilon}_{pseudo}(\omega)$. A systematic error for this procedure was determined by varying the value of $\hat{\varepsilon}_c$ between 4 and 4.5.

The c-axis corrected functions obtained from the ellipsometric measurements, $\varepsilon_{1,ab}(\omega)$ and $\sigma_{1,ab}(\omega)$, are displayed in Fig. 4.4. We observe a series of interband transitions starting around 2 eV. At this energy there is a weak onset, most clearly pronounced for the UD0 sample, which has been associated with the onset of charge transfer excitations [105]. We observe three more transitions at higher energy which show a significant doping dependence. The doping dependence of the peak onset of the transition at 3.8 - 4.2 eV is shown in the inset of figure 4.4a.

4.6 In-plane conductivity

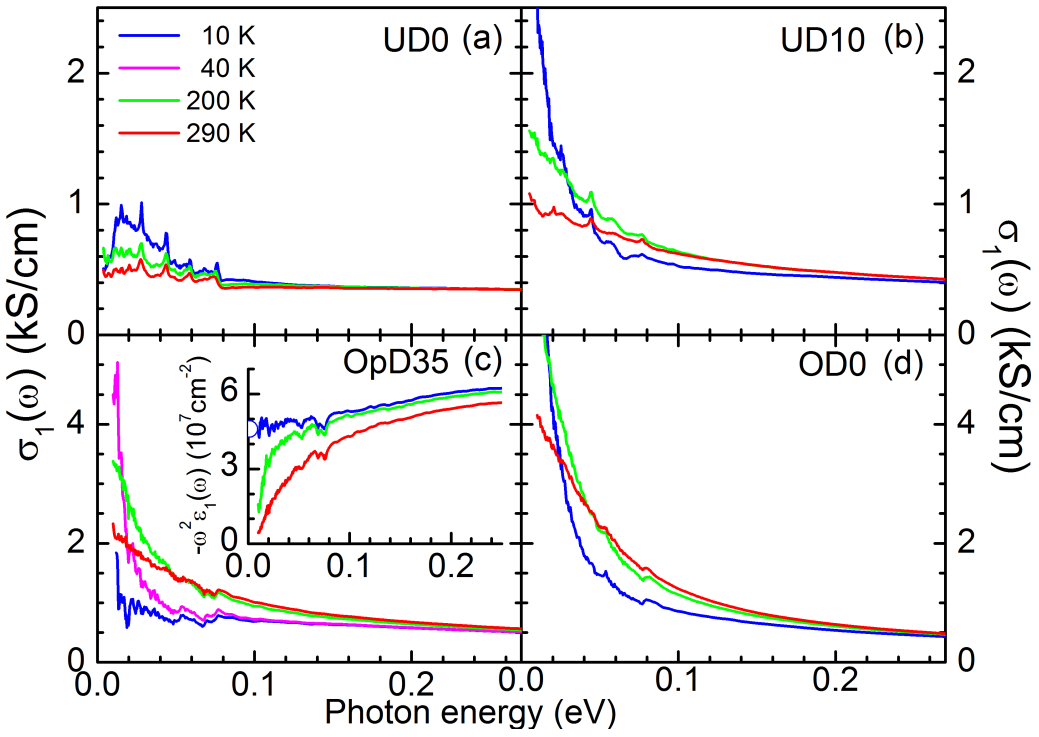

Figure 4.5: Optical conductivities for (a): UD0, (b): UD10, (c): OpD35 and (d): OD0 samples. Note the difference in scale between the upper and lower panels. For the OpD35 sample an extra curve is shown just above T_c. The inset in panel (c) shows an estimate of the superfluid density for the OpD35 sample. The open semi circle corresponds to the estimate found from a Drude-Lorentz fit of the data.

We display the optical conductivity $\sigma_1(\omega)$ in Fig. 4.5 at several temperatures. As expected the low frequency conductivity increases strongly with doping (note the factor of two difference in scale between the upper and lower panels). With exception of the UD0 sample, the conductivities show a metallic Drude response. The UD0 sample shows a broad incoherent response with an interesting temperature dependence: with decreasing temperature an asymmetric peak develops with a maximum at 16 meV. A similar structure and temperature trend has also been observed for YBCO [106]. The pronounced mid-infrared structure observed in Ref. [106] is less visible here. The optical conductivity of the OpD35 sample at T = 10 K does not show a clear signature of the superconducting gap, but the conductivity is strongly suppressed as compared with $\sigma_1(\omega)$ at T = 40 K. A signature of superconductivity is the presence of a superfluid density, which can be modeled by adding a $\delta(\omega)$-function to $\sigma_1(\omega)$ with strength $\omega_{p,s}$. $\omega_{p,s}^2$ is directly proportional to the superfluid density and can be estimated from a Drude-Lorentz fit. We find $\omega_{p,s} \approx 6800$ cm^{-1}. As a double check we use the fact that, due to causality, the delta function in $\sigma_1(\omega)$ gives rise to a contribution to $\varepsilon_1(\omega) \approx -\omega_{p,s}^2/\omega^2$. The inset in Fig.4.5c shows the estimate of the superfluid density obtained in this way together with the one obtained from the Drude-Lorentz fit as a semi circle. The two estimates are in good agreement. The superfluid density is substantially smaller compared to optimally doped Bi2212 [45] ($\omega_{p,s} \approx 9500$ cm^{-1}) and Bi2223 [47] ($\omega_{p,s} \approx 10300$ cm^{-1}) but T_c is correspondingly lower. This correlation between T_c and the superfluid density was first observed by Uemura *et al.* [48].

4.7 c-axis conductivity

The out-of plane optical constants can in principle be extracted using the following expression for the p-polarized complex reflectance,

$$\hat{r}_{\mathrm{p}} = \frac{\sqrt{\hat{\varepsilon}_{ab}}\cos\theta - \sqrt{1-\sin^2\theta/\hat{\varepsilon}_c}}{\sqrt{\hat{\varepsilon}_{ab}}\cos\theta + \sqrt{1-\sin^2\theta/\hat{\varepsilon}_c}}. \tag{4.1}$$

In this expression θ is the angle of incidence (θ = 79 deg. in our experiments), $\hat{\varepsilon}_{ab}(\omega)$ is the in-plane dielectric function determined from the normal incidence reflectivity and ellipsometric measurements and $\hat{\varepsilon}_c(\omega)$ is the dielectric function that we are looking for. We use a standard Drude - Lorentz model for the c-axis dielectric function and optimize its parameters to obtain a good fit to the measured grazing incidence reflectivity. This model gives us access to all the optical properties but the error bars we obtain on the complex conductivity are relatively large due to an unfavorable propagation of error bars of the absolute value of $R_p(\omega)$, in particular at low frequencies. The optical conductivities are shown in figure 4.6. The error bars are determined by shifting $R_p(\omega)$ by 1 percent up and down and repeating the analysis. We use the changes in the conductivities as a measure of the systematic error bar.

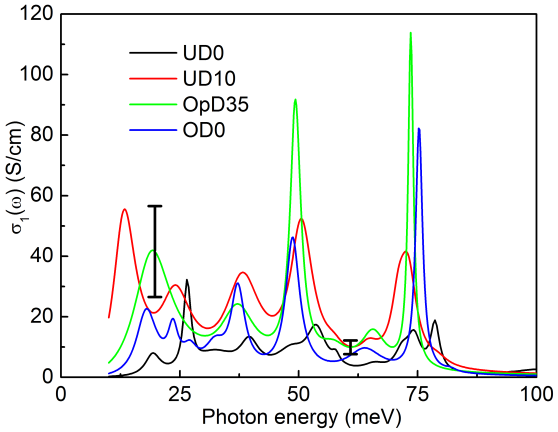

Figure 4.6: Out-of-plane conductivity extracted using the method explained in the text. The error bar shown is representative for the range below 25 meV. Above this range the error bars are smaller, as indicated by the error bar at 60 meV.

The conductivity is determined by a series of phonon modes on top of a weak electronic background. From a factor group analysis for the space group $I4/mmm$ one expects 5 IR active c-axis phonon modes [100], but usually more modes are resolved. This can be due to disorder or a superlattice in the crystal which reduces the symmetry making forbidden transitions allowed. The substitution of Sr by La may also explain the splitting of some phonon modes: the resonance frequencies scale with the reduced mass of the ions involved in the vibration. Hence, a partial substitution will give two distinct resonance frequencies corresponding to the difference in ionic mass of the substituted elements.

In figure 4.7a and 4.7b we show two different loss-functions. The first is a "pseudo loss-function" [104, 100],

$$L(\omega) \equiv Ime^{i\phi}\sqrt{1-\frac{\sin^2\theta}{\hat{\varepsilon}_c}} \approx \frac{(1-R_p)\,|n_{ab}|cos(\theta)}{2\,(1+R_p)}, \tag{4.2}$$

in which $\phi \equiv \pi/2 - arg(n_{ab})$, θ is again the angle of incidence in the experiment and n_{ab} is the in-plane complex refractive index. This approximative loss-function does not involve modeling of the grazing incidence reflectivity and separates the doping trend of the in-plane response from that of the c-axis response as illustrated in figure 4.7a. We see that the large change in absolute value of $R_p(\omega)$ in figure 4.3 derives mainly from changes in the in-plane optical properties, while the c-axis response does not change much with doping. Figure 4.7b shows the loss-function $Im(-1/\hat{varepsilon}_c(\omega))$ as determined from the Drude-Lorentz model obtained in the analysis discussed above. The error bars shown in figure 4.7b are determined in the same way as the one for $\hat{\sigma}_c(\omega)$ above.

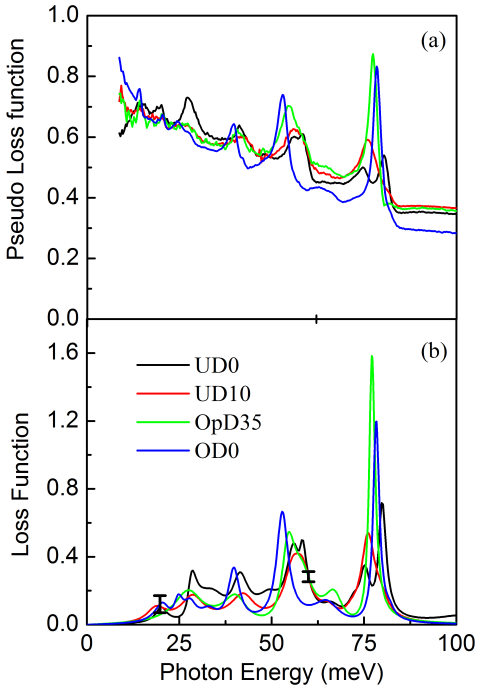

Figure 4.7: (a): Pseudo loss-function calculated using Eq. 4.2. Note the small doping dependence compared to figure 4.3, which shows that most of the variation seen in $R_p(\omega)$ is due to changes in in-plane properties. (b): loss-function obtained from the Drude-Lorentz modeling.

4.8 Extended Drude analysis

The Drude model describes the optical conductivity of a gas of non-interacting electrons with a single, energy independent channel of dissipation: $4\pi\hat{\sigma}(\omega) = \omega_p^2/(1 - i\omega\tau)$. This model is insufficient to describe the situation where the dissipation in the electron system arises from the electron-phonon or electron-electron interactions. To deal with these situations we can generalize the Drude model by introducing an optical self-energy [72],

$$\hat{\sigma}(\omega) \equiv \frac{\omega_p^2}{4\pi} \frac{i}{(\omega + \hat{\Sigma}_{opt})}. \tag{4.3}$$

Two related quantities are the effective mass, $m^*(\omega)/m = \Sigma_{opt,1}/\omega + 1$ and scattering rate, $1/\tau(\omega) = \Sigma_{opt,2}$. These quantities are useful because they are more easily interpreted physically. Eq. (4.3) is easily inverted to obtain the scattering rate $1/\tau(\omega)$ and effective mass $m^*(\omega)/m_b$ directly from the measured conductivity, provided one has an estimate for the plasma frequency, ω_p and the contribution due to interband transitions ε_∞ [74, 50].

$1/\tau(\omega)$ and $m^*(\omega)/m_b$ are shown in Fig. 4.8 at T =10 K. The UD0 sample has the highest scattering rate and strongest frequency dependence. However, $1/\tau(\omega)$ shows an upturn at low frequency and a corresponding negative effective mass in the same frequency range. The implication of this is

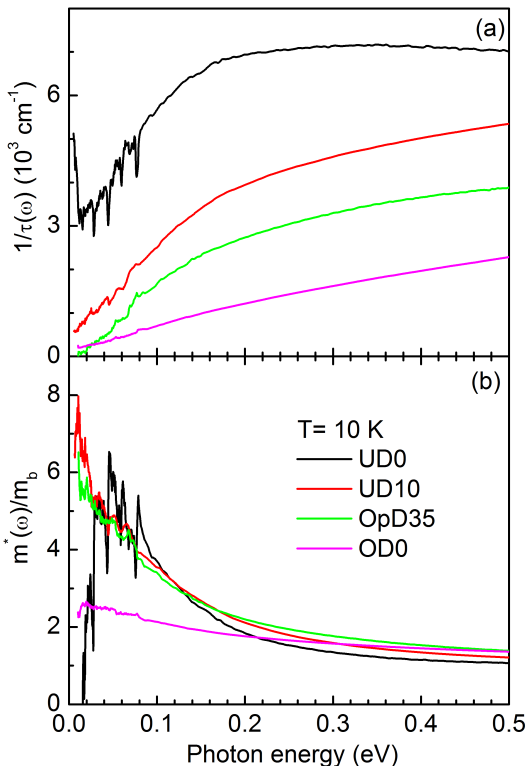

Figure 4.8: Scattering rate, $1/\tau(\omega)$ and effective mass, $m^*(\omega)/m_b$ at T = 10 K. Note the upturn in the UD0 scattering rate which indicates that the data cannot be described within this formalism.

that the low temperature, low frequency properties cannot be described in terms of an interacting gas of electrons and thus invalidates the extended Drude analysis. A similar observation was made in Ref. [106] for heavily underdoped YBCO samples. However the scattering rate reported there shows a peak structure around 150 meV which is not found here, although $1/\tau(\omega)$ shows a slight decrease at high energy. This difference reflects the fact that in YBCO the MIR peak is more pronounced than in these Bi-2201 samples.

The other three samples show monotonically increasing scattering rates, except in the vicinity of direct optical phonon absorptions. The overall scattering rate as well as the strength of the frequency dependence strongly decreases with increasing doping. This can be related to a decreasing coupling to low energy bosonic excitations. A measure of this coupling strength can be obtained from the relation $m^*/m_b(\omega \rightarrow 0) = \lambda + 1$. Therefore λ can be read of directly from Fig. 4.8b which shows that λ decreases from $\lambda \approx 6.5$ for UD10 to $\lambda \approx 1.3$ for the OD0 sample. The room temperature values for the three samples are $\lambda_{UD10} \approx 4.4$, $\lambda_{OpD35} \approx 2.8$ and $\lambda_{OD0} \approx 1.3$. The determination of these coupling strengths from experimental quantities will serve as an important consistency check in chapter 5.

Chapter 5

Analysis of optical spectra and the strong coupling formalism.

5.1 Introduction

This chapter deals with several aspects of the analysis of optical spectra in terms of electron-boson coupling. It gives a short introduction to the theory based on the Holstein model generalized by Allen. We then consider several descriptions of the bosonic spectral density. In the second part we analyze the optical properties of Hg1201 and Bi2201. We show that this formalism allows us to describe both the frequency and temperature dependence of these materials.

5.2 Strong coupling theory

The absorption of radiation in clean metals (i.e. without impurities) can only occur by the excitation of bosons in the material. Examples of such bosons are phonons, electron-hole pairs, spin waves etcetera. Since the photon momentum is negligible compared to typical momenta of excitations in the solid, absorption occurs in processes where pairs of excitations are created with momenta +**q** and -**q**. The optical self-energy introduced in section 2.4.4 arises from these processes. The static interaction with the lattice and impurities gives rise to the standard Drude behavior discussed in section 2.2.4. If one considers interactions between the electrons with phonons or collective excitations $\Sigma_{opt}(\omega)$ acquires a frequency dependence. Allen showed in 1971 that the far infrared optical properties of metals have information about these interactions encoded in their frequency dependence [107]. This turned out to be quite important for establishing that some features seen in the optical conductivity of superconducting Pb where directly related to structures in the phonon density of states [108]. The derivation of the optical conductivity from microscopic principles is complex and involves some assumptions and ap-

proximations. Here we will only outline a few points that will facilitate the discussion in later chapters. An extensive discussion is given in the book of Mahan [38]. The problem to solve is simply stated: it is to evaluate the current-current correlation function that appears in the Kubo formula,

$$\hat{\sigma}(\omega) = \frac{i}{\omega}\left\{ i\int_0^\infty dt e^{i\omega t}\langle [j(t), j(0)]\rangle + \frac{ne^2}{m}\right\} \tag{5.1}$$

The problem is that doing so, requires the evaluation of an infinity of diagrams. The approach, which is used most often, is based on the Holstein theory for normal metals [109]. One uses a diagrammatic perturbation expansion to calculate the current-current correlation function. This expansion becomes tractable by ignoring classes of diagrams. We separate the problem into two steps. Firstly the optical conductivity can be related to electron and hole self-energies [107, 110],

$$\hat{\sigma}(\omega, T) = \frac{\omega_p^2}{i4\pi\omega}\int_{-\infty}^{+\infty} \frac{(n_F(\omega+\varepsilon, T) - n_F(\varepsilon, T))}{\omega - \Sigma(\varepsilon+\omega, T) + \Sigma^*(\varepsilon, T) + i\Gamma_{imp}} d\varepsilon, \tag{5.2}$$

where ω_p is the plasma frequency, $n_F(x) = (exp(\beta x)+1)^{-1}$ is the Fermi-Dirac distribution function, $\beta = (k_b T)^{-1}$ and we have included the impurity scattering rate Γ_{imp}. It follows (see Eq. 2.128) that $\Sigma_{opt}(\omega)$ can be expressed in terms of $\Sigma(\omega)$ as,

$$\frac{\Sigma_{opt}(\omega)}{\omega} = \left\{ \int \frac{n_F(\xi) - n_F(\xi+\omega)}{\omega - \Sigma(\xi+\omega) + \Sigma^*(\xi) + i\Gamma_{imp}} d\xi \right\}^{-1} - 1 \tag{5.3}$$

Qualitatively this expression shows that the optical self-energy arises due to the creation of an electron-hole pair dressed by interactions. The next step then is to calculate the single particle self-energies using some approximations that suit the problem at hand.

The single particle self energy is given by,

$$\Sigma(\omega, T) = \int d\varepsilon \int d\omega' \tilde{\Pi}(\omega') \left[\frac{n_B(\omega') + n_F(\varepsilon)}{\omega - \varepsilon + \omega' + i\delta} + \frac{n_B(\omega') + 1 - n_F(\varepsilon)}{\omega - \varepsilon - \omega' - i\delta} \right] \tag{5.4}$$

where $n_B(x) = (exp(\beta x) - 1)^{-1}$ is the Bose-Einstein distribution function. The function $\tilde{\Pi}(\omega)$ is known as the *bosonic spectral function*. It is a measure for the spectrum of bosons through which the electrons interact. Some features of the optical spectra, like for example the opening of a gap, are not captured by Eq. 5.2 and 5.4. This is why we distinguish the functions obtained from experimental data with a tilde. It means that part of the spectrum or its temperature dependence may contain spurious features. The integral over ε can be performed analytically,

$$\Sigma(\omega, T) = \int d\omega' \tilde{\Pi}(\omega') L\left(\omega, \omega', T\right). \tag{5.5}$$

with

$$L(\omega, \omega', T) = -i\pi \coth\left(\frac{\omega}{2T}\right) + \Psi\left(\frac{1}{2} + i\frac{\omega - \omega'}{2\pi T}\right) - \Psi\left(\frac{1}{2} - i\frac{\omega + \omega'}{2\pi T}\right). \tag{5.6}$$

The $\Psi(x)$ in this last expression are digamma functions. Equations (5.2-5.6) together with the standard Fresnel equations allow us to calculate *any* optical property. In the electron-phonon theory the bosonic spectral density is taken to be proportional to the phonon density of states (DOS).
In a diagrammatic language, the self-energy is defined by the Dyson equation,

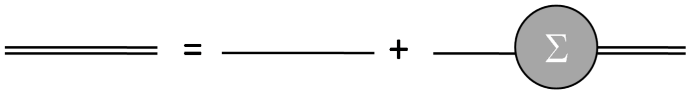

Here we use the standard notation for Feynman diagrams where full lines represent bare electron propagators, or Green's functions, while double lines represent dressed propagators. Since the dressed propagator appears on both sides of the expression, this equation implies a self-consistency problem. Part of the self energy that we consider in Eq. 5.4 contains all diagrams arising from the interactions between electrons and phonons. For example the electron interacts with itself by emitting and subsequently absorbing one or more phonons (represented by the dashed lines),

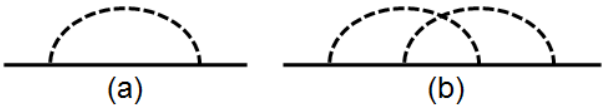

Diagram (b) is known as a vertex diagram and is usually ignored as it is of higher order than the diagram where the phonon interacts with electron-hole pair excitations of the "vacuum". The lowest order contribution of which is given by,

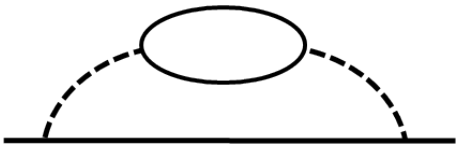

Due to this interaction one has to consider the dressed phonon propagator. Since it is difficult, if not impossible, to treat this problem exactly one uses measured phonon dispersions from inelastic neutron scattering experiments to construct the function $\alpha^2F(\omega)$. In this way one includes all the important renormalizations of the phonon propagator in the function $\alpha^2F(\omega)$. Eq. 5.4 then tells us how to calculate the electron self energy. A good introduction to the electron - phonon problem and the underlying assumptions is given in [21].

A second part of the self-energy comes from the Coulomb interaction. This part is even more complicated to determine exactly, even for simplified model Hamiltonians. Approximate expressions for several models have been derived and will be considered in the next section.

There are a few approximations underlying the theory that could be of influence when it is applied to anisotropic and more importantly, strongly correlated systems like the cuprates:

5. ANALYSIS OF OPTICAL SPECTRA AND THE STRONG COUPLING FORMALISM.

- We ignore the momentum dependence of the self-energy.
- Vertex corrections are assumed to be small (Migdal's approximation).
- The density of states is assumed to be energy independent.
- The unperturbed state is a Fermi liquid.

The formalism discussed in this section applies to the normal state of metals. The function $\alpha^2F(\omega)$ also appears in the Migdal-Eliashberg-Nambu theory of superconductivity. Within this framework $\alpha^2F(\omega)$ determines the properties of the superconductor like the size of the gap and the value of T_c. The deviations from the BCS ratio $2\Delta/k_BT_c$ = 3.52 in real superconductors can only be understood within this framework. Several issues concerning high T_c superconductors are (i) can we interpret the important interactions in terms of a retarded electron-electron interaction, (ii) if it exists, is this interaction mediated through phonon exchange alone or do other bosons contribute as well, (iii) can one apply the approximations made for ordinary metals to the cuprates and (iv) does a d-wave generalization of the Eliashberg theory describe the superconducting properties. In other words, is there a function $\tilde{\Pi}(\omega)$ that replaces $\alpha^2F(\omega)$ in the theory of ordinary metals, and that can be used to describe the properties of the high temperature superconductors? An important problem to solve therefore, is to find a way of determining the function $\tilde{\Pi}(\omega)$. Since we do not know the minimal model describing the high T_c cuprates, we need to find a way of experimentally determining $\tilde{\Pi}(\omega)$. This is where optical spectroscopy may play an important role. From the conventional superconductors we know that the Eliashberg function $\alpha^2F(\omega)$ can be determined accurately from the optical conductivity. So, as a starting point, we can use the formalism as described above to extract $\tilde{\Pi}(\omega)$ from optical spectra. Once we have these spectra we can check for the consistency of the formalism by comparing results to those obtained from other experimental techniques. Another way of checking the consistency of the method is by comparing the coupling constant extracted from experiment to the one calculated from the $\tilde{\Pi}(\omega)$ function. The extended Drude formalism of section 2.4.4 gives us access to the effective mass, which is related to an effective coupling constant λ as, m^*/m=1+λ. The effective coupling is related to the $\tilde{\Pi}(\omega)$ function through,

$$\lambda(\omega) = 2\int_0^{\omega} d\Omega \frac{\Pi(\Omega)}{\Omega}. \tag{5.7}$$

The reason why λ is called an "effective coupling" is, that it is not the same coupling constant that appears in the Hamiltonian of the problem. It is the coupling constant that enters the McMillan formula for T_c,

$$T_c = 0.83\tilde{\omega}e^{-1.04\frac{1+\lambda}{\lambda}} \tag{5.8}$$

The logarithmic average of $\tilde{\Pi}(\omega)$, $\tilde{\omega}$ is defined as,

$$\tilde{\omega} = e^{\frac{2}{\lambda}\int_0^{\infty} ln(\Omega)\frac{\Pi(\Omega)}{\Omega}d\Omega} \tag{5.9}$$

In the weak coupling limit one can use Eq. 5.8 to calculate T_c, but for couplings larger then $\lambda \approx 1$ - 2, one should resort to a solution of the Eliashberg equations. When applied to the cuprates, one has to wonder if this class of materials still falls in the range of validity of the Migdal-Eliashberg formalism. As alluded to in the introduction, the theory developed by Eliashberg rests on the assumption that one can ignore vertex corrections. In certain models one can show that vertex corrections can be ignored even at large couplings, but in general this is probably not the case. It is therefore crucial to check the internal consistency between values of $lambda$ extracted directly from experiment and from theory. The experimental determination of the value of λ is an important assets of the optical conductivity. It cannot be extracted easily from other transport experiments, nor from spectroscopies like ARPES. In principle one can estimate λ from ARPES, but with a large uncertainty due to the fact that the bare dispersion is not known.

5.3 The bosonic spectral function $\tilde{\Pi}(\omega)$

The inversion of Eq's 5.2 and 5.4 allows to extract $\tilde{\Pi}(\omega)$ from experimental data of the optical conductivity, or related optical spectra. The accuracy of the resulting $\tilde{\Pi}(\omega)$ spectrum is in practice limited by the convolution with thermal factors expressed by Eq's 1 and 2 (see also section 7.4) [111]. Different microscopic models can have similar $\tilde{\Pi}(\omega)$ spectra, which leads to slightly differing frequency dependencies of the optical conductivity. Our method is based on fitting optical spectra. It is therefore of crucial importance to test the 'robustness' of each fit with regard to the spectral shape of the $\tilde{\Pi}(\omega)$ function imposed by different models. This robustness can be tested by including in the fit-routine one or several 'oscillators' superimposed on the model function. When the model glue function provides a complete description, adding extra oscillators will not result in an improvement of the quality of the fit. We have used this approach to test functional forms commonly used in the literature, in particular the marginal Fermi liquid (MFL) model [112] and the Millis-Monien-Pines (MMP) representation of the spin fluctuation spectrum [113].

5.3.1 Marginal Fermi liquid.

The Marginal Fermi Liquid (MFL) phenomenology [112, 114] is based on the hypothesis that "there exists charge and spin density excitations with the absorptive part of the polarizability at low frequencies ω proportional to ω/T and constant otherwise." It predicts that $\tilde{\Pi}(\omega)$ is given by,

$$P_{MFL}(\omega) = \Lambda \tanh(\frac{\omega}{2T}) f(\omega, \omega_c, \Delta) \tag{5.10}$$

where Λ is an overall coupling constant, T is the temperature and $f(\omega, \omega_c, \Delta)$ is a high energy cutoff function the precise shape of which is unimportant. We have used $f(\omega, \omega_c, \Delta) = 1/(1 + exp(\frac{(\omega-\omega_c)}{\Delta}))$

as proposed by Varma [112]. An important feature of this spectrum is that it only depends on ω/T. It is easy to see using Eq.'s 5.2-5.6 that in this case one retrieves the linear temperature dependence of the resistivity seen in many experiments. It would also give rise to a conductivity that scales as $\sigma(\omega, T) = T^{-1}g(\omega/T)$ as observed in experiments [115]. More recently [114] a microscopic model was derived that gives rise to the form proposed in [112].

5.3.2 Spin fluctuation theory.

Several other theoretical models are based on the notion that spin fluctuations play an important role in understanding the physics of the (underdoped) cuprates [39, 113, 116]. In these models one uses the imaginary part of the dynamic spin susceptibility $\chi''(\omega, \vec{q} = 0)$ as a measure for the bosonic spectral density which in the ungapped state is given by [113],

$$\Pi_{MMP}(\omega) = \frac{\Gamma\omega}{\gamma^2 + \omega^2} \quad \omega \leq \Omega_c \tag{5.11}$$

Here Γ is a coupling strength and Ω_c a cutoff. The spectrum has a maximum at $\omega = \gamma$. We refer to this model as the Millis-Monien-Pines (MMP) model [113]. Note that this form is valid only if there is no (pseudo)gap. Although the temperature dependence is not explicitly mentioned in Eq. 5.11 the parameters γ and Γ depend on temperature. $\Pi_{MMP}(\omega)$ does not scale as ω/T unless both γ and Γ are depending linearly on temperature. The temperature dependence of the MFL and MMP models are an important point of contrast with the EP interaction. In the latter case $\alpha^2F(\omega)$ is temperature independent. The fact that most experimental studies find that for the cuprates $\tilde{\Pi}(\omega)$ has to be made temperature dependent is one of the arguments against the interpretation of $\tilde{\Pi}(\omega)$ in terms of phonons alone .

5.3.3 MFL and MMP + phonon models

Finally we allow for a Lorentzian oscillator (in addition to the MFL and MMP model) given by,

$$\Pi_{Lor}(\omega) = \frac{f_1^2\Gamma_1\omega}{(\omega\Gamma_1)^2 + (\omega_1^2 - \omega^2)^2} \tag{5.12}$$

Here f_1 is the oscillator strength, Γ_1 is the width and ω_1 is the center frequency. Such a peak can be used to describe the coupling of electrons to a well defined mode like phonons or to the spin resonance.

5.3.4 Histogram representation.

We will also use a more general function that does not depend on a microscopic description. It consists of a histogram representation of $\tilde{\Pi}(\omega)$ using N blocks with flexible widths and heights,

$$\tilde{\Pi}(\omega) = f_i \quad \omega_{i-1} \leq \omega \leq \omega_i \tag{5.13}$$

where i runs from 1 to N, ω_0 = 0 and f_i is the height of the ith block. For $\omega_0 \leq \omega \leq \omega_1$ we use $\tilde{\Pi}(\omega) = f_1\omega$ to circumvent the divergence of the integral in Eq. 5.4. The $2N$ parameters of this model are optimized using a standard Levenberg-Marquardt routine. The resulting histogram gives an indication of the important features in the $\tilde{\Pi}(\omega)$ spectrum. We find that the detail of $\tilde{\Pi}(\omega)$ that can be extracted from the experimental data is best represented with N = 6 blocks. For cuprates the function $\tilde{\Pi}(\omega)$ consists of two main features: a peak with an energy in the range 50 - 60 meV and a broad spectrum extending up to 400 meV.

5.4 The method

Starting from a $\tilde{\Pi}(\omega)$ function we can calculate the optical conductivity, Eq. 5.2, which in turn is fed into standard Fresnel expressions to calculate the experimentally measured quantities, *i.e.* reflectivity and ellipsometric parameters (see chapter 2). The fitting routine is based on the Levenberg-Marquardt algorithm and uses analytical expressions for the partial derivatives of the reflectivity coefficient $R(\omega)$, and the ellipsometric parameters ψ and Δ relative to the parameters describing the $\tilde{\Pi}(\omega)$ function. The algorithm is based around minimizing the mean square deviation, χ^2, which is given by,

$$\chi^2 = \sum_{i=1}^{N} \left(\frac{y(\omega_i) - f(\omega_i, p_1, ..., p_n)}{\sigma_i} \right)^2 \tag{5.14}$$

where $y(\omega_i)$ is an experimentally measured datapoint, $f(\omega_i, p_1, ..., p_n)$ is the calculated value in this point based on parameters $p_1, ..., p_n$ and the difference between these two is weighed by the errorbar σ_i determined for $y(\omega_i)$. For a given set of reflectivity and ellipsometry data at one particular temperature, using a standard PC, the iteration takes about 3 hours until convergence is reached. Although the Levenberg-Marquardt least squares method is an extremely powerful method to find the minimum of χ^2 in a multidimensional parameter space it has difficulties with finding the best solution to the non-linear problem Eq's 5.2 and 5.4. For each individual sample and temperature several tests have been performed where in each test the optimization process was started from a different set of starting parameters to ensure that χ^2 has converged to the global minimum in parameter space. Examples of experimental reflectivity data together with the fits are shown below (Fig. 5.1 and Fig. 5.3) for data sets spanning a broad doping and temperature range. As the fitted curves are within the limits of the experimental noise, further reduction of χ^2, while in principle possible by fitting the statistical noise of the data, can not improve the accuracy of the $\tilde{\Pi}(\omega)$ functions. In the next section we apply this method to the optical spectra of Hg-1201 discussed in chapter 3.

5.5 Analysis of optical spectra: $HgBa_2CuO_{4+\delta}$

We first analyze optical spectra of optimally doped $HgBa_2CuO_{4+\delta}$ (Hg-1201). We do not take into account the opening of a (pseudo-)gap in our analysis so we can only apply it to temperatures of 100 K and higher. Recent neutron scattering experiments [28] show that at optimal doping the pseudogap temperature is smaller or equal to the critical temperature for these materials at optimal doping, although specific heat measurements on the particular sample used in this study show an onset of the specific heat jump at slightly elevated temperatures [50]. In figure 5.1 we show the reflectivity for Hg-1201 together with the optimized model curves obtained with Eq.'s (5.10), (5.11) and (5.13). Figure 5.1a shows the results for the MFL model. At 290 K we can make a reasonable fit to the reflectivity but with decreasing temperature the fit becomes progressively worse. Note that we try to fit the overall frequency dependence of $R(\omega)$ and not the sharper phonon structures below 80 meV. It is important to note that in order to optimize χ^2 we have to make the coupling constant λ in Eq. 5.10 temperature dependent. This means that already at this level the ω/T scaling is lost even for the MFL model. Our result obtained at room temperature is similar to that obtained in an earlier study [117]. As was found in that study we find that if we add an extra scattering channel to the MFL model the fit is greatly improved (see below). $\Pi_{MMP}(\omega)$ (panel 5.1b) shows a similar trend as seen for $\Pi_{MFL}(\omega)$: a reasonable fit at room temperature but less good at low temperature. Finally, figure 5.1c shows the result obtained with $\Pi_{HG}(\omega)$ that gives the best description of the optical data.

In figure 5.2(a),5.2(b) and 5.2(f) we display the spectral functions corresponding to the fits in figure 5.1. Also shown are the models that are obtained when an extra oscillator is added to the MFL and MMP models. The panels of figure 5.2 give a lot of information on the structure of $\tilde{\Pi}(\omega)$. It shows three important features: (i) $\tilde{\Pi}(\omega)$ has to be made temperature dependent. (ii) there is a high energy scale that is determined by the cutoff in $\tilde{\Pi}(\omega)$ around 300 meV. (iii) there is a low energy scale determined by a maximum in $\tilde{\Pi}(\omega)$ around 55 meV. We do not find evidence for ω/T scaling of the function $\tilde{\Pi}(\omega)$ from the model calculations.

Table 5.1: χ^2 defined by Eq. 5.14 for the three different models. The values in parenthesis are obtained when a Lorentzian peak (Eq. 5.12) is added to the MFL and MMP spectral functions.

Model	290 K	200 K	100 K
MFL	117 (13)	127 (21)	163 (22)
MMP	23 (15)	37 (21)	74 (18)
HG	12	19	13

The models are evaluated based on the minimum found for the χ^2. A comparison of the values of

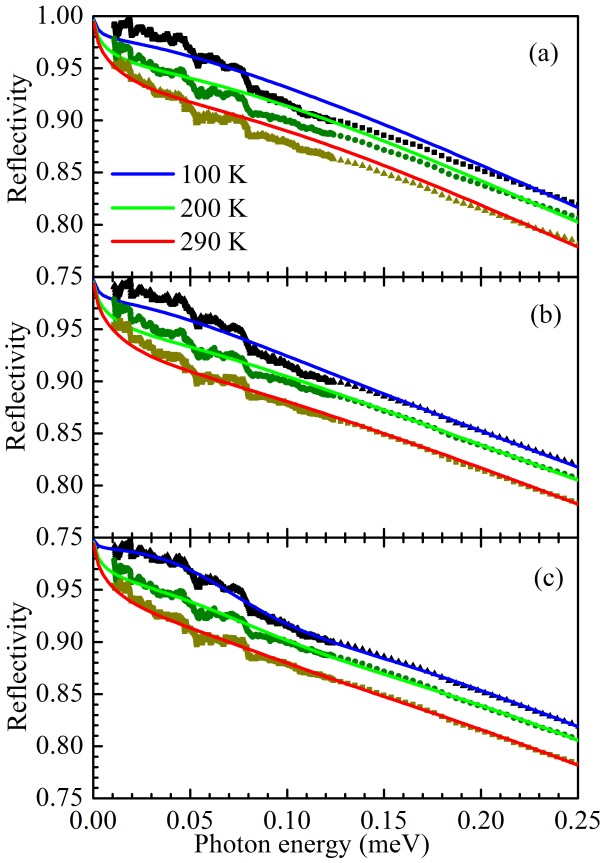

Figure 5.1: Reflectivity of Hg-1201 together with fits for three different models. (a): MFL model, (b): MMP model and (c): histogram.

χ^2, indicated for the room temperature results in Fig. 5.2, and at lower temperatures in table 5.1, shows that the MMP model better describes the optical data than the MFL model. However, they give similar results if we add an extra oscillator to these models. Panels 5.2(e-f) show the model independent results, based on two oscillators and the histogram representation, and are very similar to the modified MMP and MFL model. The models in these last two panels have the same χ^2 and the comparison in Fig. 5.2g shows that the histogram representation realistically expresses the uncertainty in the position of the low energy peak, while the correspondence between the features in both models remains excellent. Comparing panels 5.2(e-f) to 5.2(a-b) it becomes clear why the MMP model performs better than the MFL model: the MMP model has a maximum around 55 meV similar to the peak seen in the histogram representation. The MFL model in contrast has a broad maximum around 150 meV. The model with two oscillators is described by 6 parameters, while the histogram representation uses 12 parameters. The fact that the fit-routine adjusts the latter 12 parameters in such a manner as to produce in essence the two oscillator lineshape, shows a good convergence of the fit.

The comparison of the panels in figure 5.2 suggests that we may get a better fit if we add a narrow

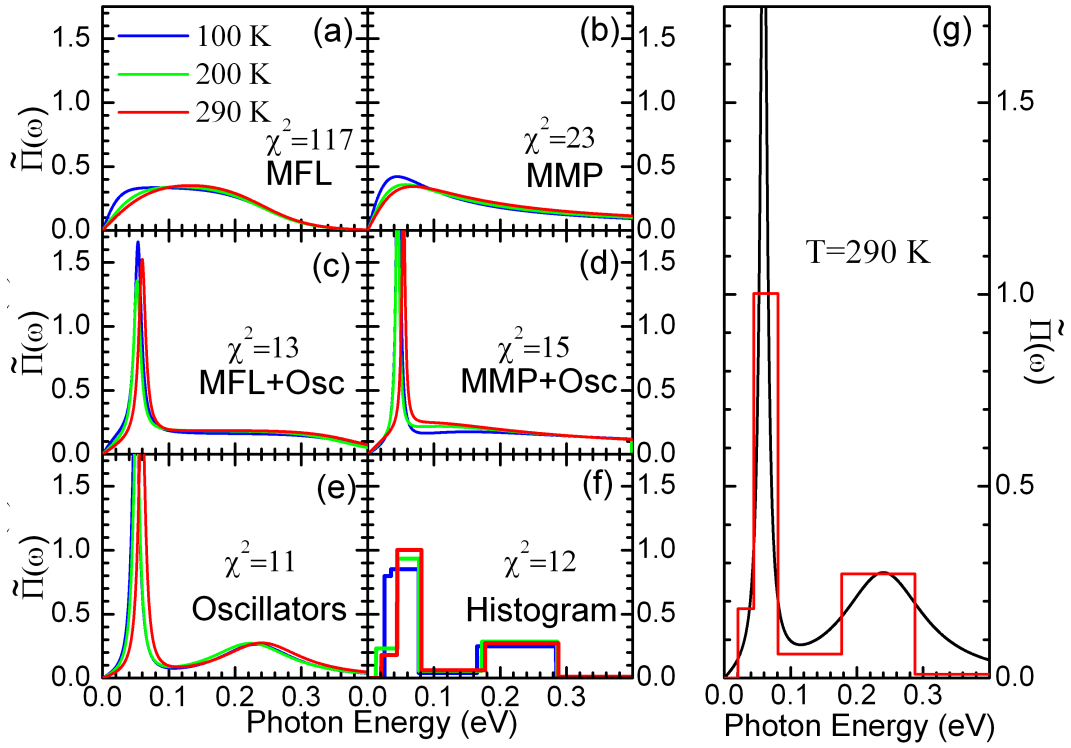

Figure 5.2: Comparison of several models. The number of data points over which χ_j^2 is summed (see Eq. 1) is $N = 400$. The quoted values of χ^2 are those for the room temperature spectra. At 100 K these values increase by a factor 1.5 (MFL) and 3.5 (MMP). In contrast, in the oscillator and the histogram model the χ^2 was found to be independent of temperature.

peak to the MFL or MMP model. As shown in table 5.1 the addition of this peak dramatically improves the quality of the fit. In such a model we can easily separate the contribution due to the peak and the one due to the continuum which is not possible for the histogram representation. For each spectrum we can calculate the coupling constant given by Eq. 5.7, and separate the contribution from the 55 meV peak and the continuum. The total coupling constant at T = 290 K from the histogram method is λ_{HG} = 1.85 while λ_{MFL} = 1.9 and λ_{MMP} = 1.8. In the latter two cases the peak contributions are $\lambda_{peak,MFL}$ = 0.88 and $\lambda_{peak,MMP}$ = 0.65 respectively. The peak energy is somewhat lower in energy than the low energy dispersion kink seen in ARPES experiments [78]. The coupling constants obtained by ARPES are of the order $\lambda \approx 0.3$ - 0.8 [118, 119, 120, 121, 95] as are the coupling constants derived from LDA [122, 123]. The remaining coupling constant $\lambda_{cont} \approx 1.2$ for the MMP contribution also corresponds well with earlier estimates [124]. When the temperature is decreased the total coupling constant increases: λ_{200K} = 2.0 and λ_{100K} = 2.3. Figure 5.2f indicates that this increase arises not simply from an increase in coupling to the mode, as expected in a model describing an effective interaction with spin fluctuations, but rather from an increase in intensity in the energy range below 50 meV. Since we cannot exclude pseudogap effects to play a role here we refrain from separating the contributions due

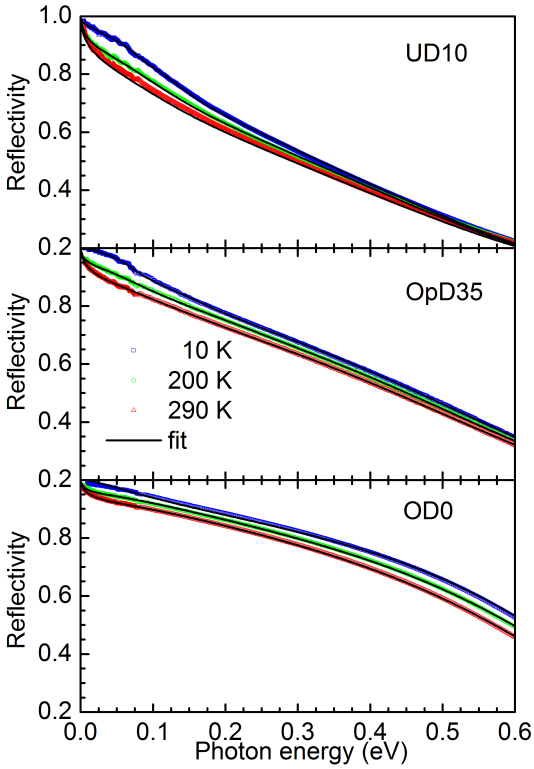

Figure 5.3: Reflectivity of Bi2201 together with fits for three different dopings.

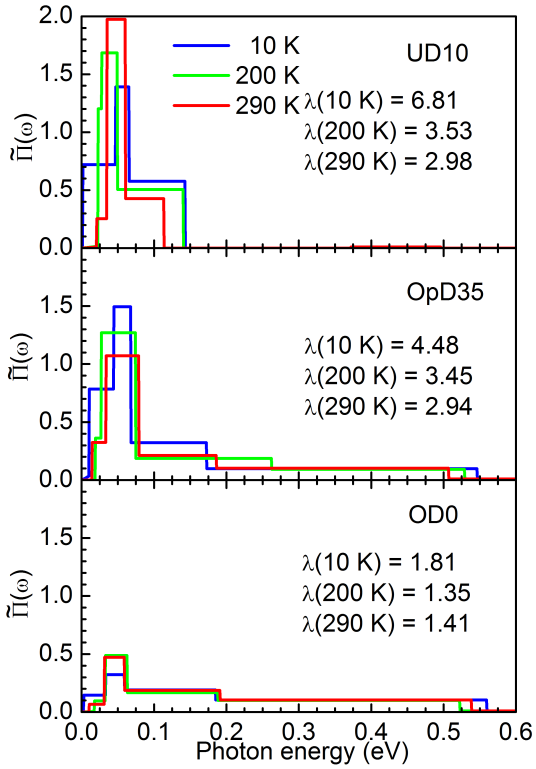

Figure 5.4: $\tilde{\Pi}(\omega)$ functions corresponding to the fits in the left panels. Indicated in each panel are the total coupling constants (see Eq. 5.7).

to the mode and the background.

5.6 $Bi_2Sr_2CuO_{6+\delta}$: comparison between ARPES and optics.

We now turn to the the optical data of Bi2201 presented in chapter 4. Fig. 5.3 shows the reflectivity of three Bi2201 samples together with the calculated curves obtained with the $\tilde{\Pi}(\omega)$ functions in the right panels. As discussed in section 4.8 the UD0 sample cannot be described within the strong coupling formalism, and is therefore not shown. The $\tilde{\Pi}(\omega)$ functions show a strong doping and temperature dependence: the underdoped $\tilde{\Pi}(\omega)$ function is narrow, strongly peaked and shows a large temperature dependence. The optimally doped $\tilde{\Pi}(\omega)$ function has a much broader spectrum resembling more that of Hg1201 but has a less pronounced structure in the mid infrared. The overdoped sample has the smallest low energy peak of the three and at the same time the weakest temperature dependence. The coupling constants for these spectra are indicated in the figure. We come back to a discussion of the coupling constants in chapter 7.

We have used the analysis of optical spectra to extract information on $\tilde{\Pi}(\omega)$. This can of course also be done using other techniques like ARPES and STM. ARPES experiments have been performed on pieces from the same OpD35 and OD0 samples presented in this work [95, 125, 126]. We now make a comparison between these two techniques but before doing so we summarize some experimental results obtained from ARPES.

The experimental results from ARPES indicate two distinct structures in the electron energy dispersion. Along the nodal direction one observes a kink at low energy $\sim$ 50 - 70 meV [127, 119, 128, 95] followed by a "waterfall" around 350 meV [129, 130]. The interpretation of these two features is still under debate. Along the anti-nodal direction only the low energy feature is observed since the band bottom occurs around 100 meV. The kink has a smaller energy $\approx$ 40 meV in the normal state and is shifted to $\approx$ 70 meV in the superconducting state as a result of the opening of the superconducting gap [131, 132, 120, 133].

If we ignore for the moment the momentum anisotropy, the self energies calculated with $\tilde{\Pi}(\omega)$ can be compared to $\Sigma(\omega)$ extracted from ARPES. ARPES experiments have been performed on crystals taken from the same batch as used in this study [95, 126]. The self-energy along the nodal direction has been determined using a full 2D analysis of the spectral function using the LDA band structure as bare band dispersion [126].

The self energies of the OpD35 and OD10 samples are shown in figure 5.5a and 5.5b respectively by open circles. The self energies calculated from the optical $\tilde{\Pi}(\omega)$ function are shown in the same figure in red. At first glance these self energies appear to be quite different but a closer examination shows that many features correspond quite well. Both experiments show structure in the 50 -60 meV range and find a maximum in $\Sigma(\omega)$ in the 200 - 300 meV range. Note that in order to determine the experimental $\Sigma(\omega)$ from ARPES, an assumption has to be made for the bare band dispersion. The fact that both the experimental and calculated self-energy have almost parallel slope in the zero-frequency limit, suggests that at least the low energy properties determined by optical spectroscopy and ARPES are compatible.

The ARPES self-energy can be further analyzed using our histogram model for $\tilde{\Pi}(\omega)$. The fit to the ARPES $\Sigma(\omega)$ is shown in blue in Fig. 5.5a and Fig. 5.5b. The $\tilde{\Pi}(\omega)$ functions obtained from optics and ARPES are compared in panels 5.5c and 5.5d. The similarities in magnitude and structure of the optical and ARPES glue-functions are striking and show that the self-energies obtained from ARPES and optics are closer than suggested by the comparison of the self-energies in the left panels of Fig. 5.5. We note that the low energy kink in the ARPES data gives rise to a peak in $\tilde{\Pi}(\omega)$ at the same energy as the optical data. The total coupling constants, indicated in figure 5.5c and 5.5d, are somewhat larger for the optical $\tilde{\Pi}(\omega)$ function. The same trend is seen in figure 5.7 where we compared λ obtained from ARPES and optics for several samples. Since the optical conductivity has

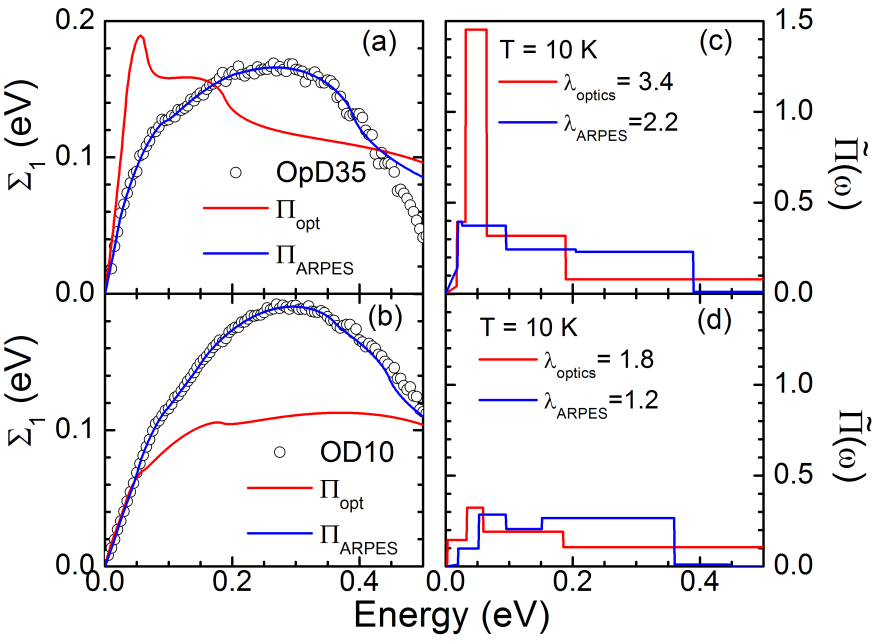

Figure 5.5: (a): Comparison between experimental $\Sigma(\omega)$ (open circles), calculated $\Sigma(\omega)$ from the 10 K $\tilde{\Pi}(\omega)$ spectra (red lines) and $\Sigma(\omega)$ obtained from a direct fit to the ARPES data (blue lines) for the OpD35 sample. (b): Same as in (a) but for the OD10 sample. (c,d): The $\tilde{\Pi}(\omega)$ functions corresponding to the calculated $\Sigma(\omega)$'s in the left panels. Also indicated are the total coupling constants corresponding to these spectra.

contributions from all of k-space one may expect that this explains the difference between optical and ARPES results. According to Stojkovic and Pines the optical conductivity is a linear superposition of contributions along the Fermi surface where the self-energies are k-dependent quantities [134],

$$\hat{\sigma}(\omega) = \frac{e^2}{8\pi^2}\int_{FS}\frac{dk}{|v_f|}\int_{-\infty}^{+\infty}\frac{d\varepsilon[f(\omega+\varepsilon,T)-f(\varepsilon,T)]}{i\omega}\times \frac{v_f^2(k)}{\omega-\Sigma_k(\varepsilon+\omega,T)+\Sigma_k^*(\varepsilon,T)}, \tag{5.15}$$

We can estimate the effect of anisotropy using our knowledge of the electronic structure from ARPES. As summarized above, the kink disperses from 70 meV at the nodal direction to 40 meV at the anti-nodal direction [24]. We also assume that along the ani-nodal direction $\Sigma(\omega)$ is zero for energies below the band bottom. The second ingredient needed is the *bare* Fermi velocity, v_F. Estimates for the k-dependence of v_F are available for Bi-2212 from Kaminski *et al.* [135]. The effect of anisotropy on $\tilde{\Pi}(\omega)$ can now be estimated by assuming that $\hat{\sigma}(\omega)$ has two contributions: one from the nodal direction and one from the anti-nodal direction.

We separately calculate the conductivity arising from the nodal and anti-nodal directions using the $\tilde{\Pi}(\omega)$ functions given in Fig. 5.6a and 5.6c. These functions are chosen such that they are compatible

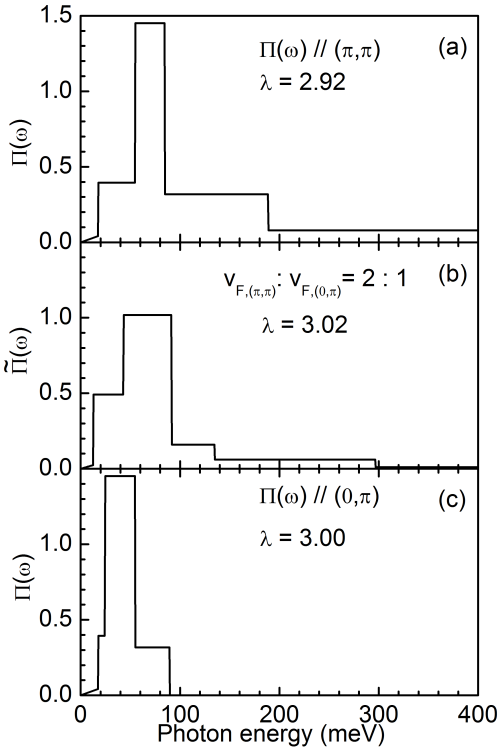

Figure 5.6: Estimate of the effect of k-space anisotropy on the optical conductivity. (a): Assumed $\tilde{\Pi}(\omega)$ for the nodal direction. The main peak is situated at 70 meV as determined by ARPES [119]. (b) $\tilde{\Pi}(\omega)$ determined by analyzing the optical conductivity assuming contributions to $\sigma_1(\omega)$ from panels (a) and (c) weighted with a ratio of the nodal to antinodal Fermi velocity 2 : 1. (c) Assumed $\tilde{\Pi}(\omega)$ for the anti-nodal direction. The main peak is situated at 40 meV as determined by ARPES [131]. Also indicated is the integrated coupling constant λ for each spectrum.

with the ARPES experiments discussed above. The resulting conductivities are weighted with the Fermi velocity ratio $v_{F,(\pi,\pi)} : v_{F,(0,\pi)} = 2 : 1$. The resulting optical conductivity is then analyzed using the same method as in section 5.4. The $\tilde{\Pi}(\omega)$ function shown in Fig 5.6b shows that the momentum anisotropy in $\Sigma(\omega)$ gives rise to an increased coupling strength and a mode energy that is a weighted average of the nodal and antinodal direction. A comparison of these results with the $\tilde{\Pi}(\omega)$ functions from Fig. 5.5c and 5.5d shows that, (i) the low energy kink seen by optics has an energy somewhat smaller than the nodal kink energy seen by ARPES and (ii) there is less intensity in the high energy range seen by optics compared with the nodal self-energy determined from ARPES. Both effects arise because the optical $\tilde{\Pi}(\omega)$ function is an effective function that contains contributions from all points around the Fermi surface.

Equation 5.4 shows that $\Sigma(\omega)$ is additive: it can be separated into contributions coming from different modes. Meevasana *et al.* showed that if a smooth continuum is subtracted from the full $\Sigma_1(\omega)$ the remaining self-energy can be shown to arise from the coupling to several bosonic modes with energies falling in the phonon frequency range [95]. They showed that the c-axis loss-function could be used as representation for the bosonic spectral density for the OpD35 sample [125]. By comparison to LSCO they assumed that the weaker coupling strength in the OD10 sample arises due to stronger screening of the electron-phonon coupling. In LSCO the broad incoherent c-axis response at optimal doping becomes more coherent in the overdoped regime and this effectively screens out the

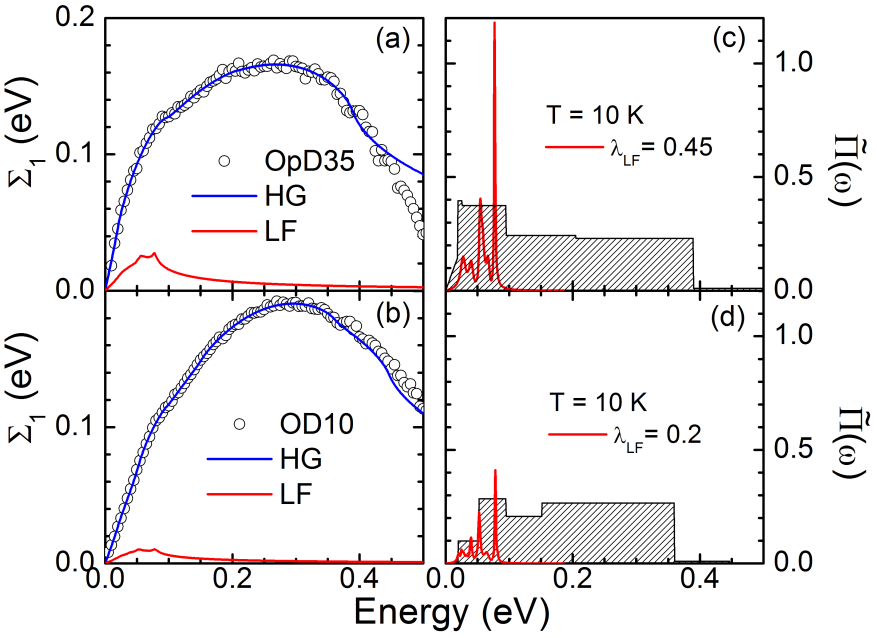

Figure 5.7: Experimental ARPES self-energy (open circles) and the self-energy calculated from the c-axis loss-function for (a): the OpD35 sample and (b): the OD10 sample. The right panels show the corresponding $\tilde{\Pi}(\omega)$ functions. The loss-functions have been scaled by an overall factor of b = 0.74 (OpD35) and b = 0.34 (OD10) as explained in the text.

low frequency phonons. The loss-functions in Fig. 4.7 show that in Bi-2201 this screening effect does not occur.

In Fig. 5.7a we compare the self-energy obtained using $Im(-1/\hat{\varepsilon}_c)$ as model for the full self-energy. Panel 5.7c shows the loss-function scaled by a factor b (b only contains numerical factors from momentum integrations, see Ref. [125]) and the $\tilde{\Pi}(\omega)$ function obtained from the fit of the full $\Sigma(\omega)$. The parameter b is determined by a fit to the partial self-energy as in Ref. [95]. For the OpD35 sample we find b = 0.74. The coupling constant $\lambda \approx 0.45 \pm 0.1$ in this case. A similar analysis for the OD10 sample gives b = 0.34 and $\lambda \approx 0.2 \pm 0.15$. This is about one quarter of the total coupling constant and compares well with estimates of the electron-phonon coupling constant obtained from LDA calculations [122]. A comparison between the loss-function and the $\tilde{\Pi}(\omega)$ function in panels 5.7c and 5.7d suggests that there could be a contribution to $\tilde{\Pi}(\omega)$ arising from the coupling to phonons. However, there is much more intensity in $\tilde{\Pi}(\omega)$ than can be explained by the loss-function alone.

We finally compare our results to tunneling experiments. The analysis of tunneling data for the cuprates turns out to be more complicated than for conventional superconductors. Several groups have found evidence for coupling to bosonic modes. Two groups report coupling to a mode around 40 meV [136, 137, 138]. This is significantly lower than our result. We note however that the tunneling experiments are mainly sensitive to the anti-nodal region of k-space due to the presence of the van

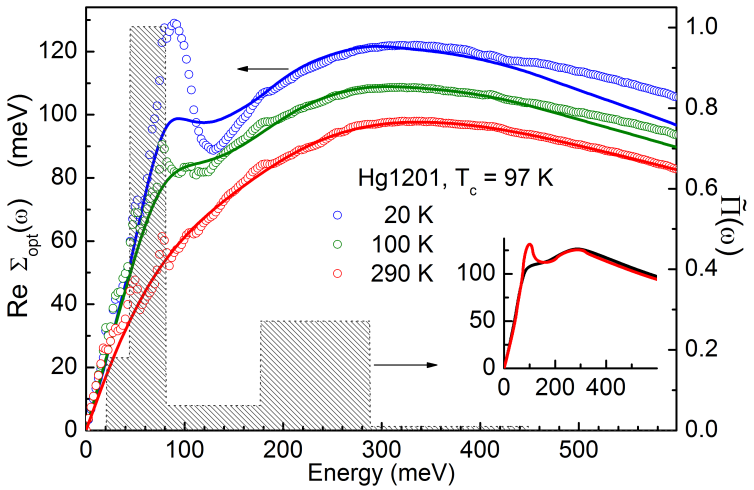

Figure 5.8: Experimental optical self-energy of Hg1201 for 3 selected temperatures (open circles). The solid curve at 290 Kelvin, 100 K and 20 K are calculated with the same $\tilde{\Pi}(\omega)$ function corresponding to 290 Kelvin. This shows that the self-energy feature between 80 and 100 meV (a shoulder at 100 K and a peak at 20 K) is caused by the prominent peak in $\tilde{\Pi}(\omega)$ at approximately 50 - 60 meV. The sharpening of this feature at low temperature is due to the superconducting gap, an aspect not captured by Eq. 5.2 and therefore not reproduced in the calculated solid curves. In the lower right panel the gap-induced sharpening is illustrated by the optical self-energy without (black) and with (red) a 15 meV superconducting gap, calculated using Allen's relation [107]. Figure adapted from [139].

Hove singularity. As we have seen above ARPES experiments indicate that in the antinodal region the mode energy is indeed close to 40 meV. As we have seen above the optical conductivity has structure at somewhat higher energy due to the momentum anisotropy, so these results are not inconsistent with ours.

5.7 Temperature dependence in the strong coupling formalism.

We have seen that the $\tilde{\Pi}(\omega)$ functions of Hg-1201 and Bi-2201 are temperature dependent, but this should in principle be folded out by the thermal factors in Eq. 5.2 and 5.4. Here we pose the question wether this temperature dependence of $\tilde{\Pi}(\omega)$ invalidates the strong coupling formalism.

Fig. 5.8 shows the $\tilde{\Pi}(\omega)$ function for $T = 290$ K (shaded area), together with the optical self-energies calculated with this function at three different temperatures. For 290 K the theoretical curve runs through the data points, reflecting the full convergence of the numerical fitting routine. The theoretical curves at $T = 100$ K and $T = 20$ K are calculated with the same $\tilde{\Pi}(\omega)$ as for $T = 290$ K, but with the temperature changed corresponding to the actual temperature in Eq.'s 5.2 and 5.4. In other words, the strong temperature dependence of the experimental optical spectra is mainly due to

the Fermi and Bose factors of Eq.'s 5.2 and 5.4. The small differences between experimental and theoretical curves reflect the temperature dependence of $\tilde{\Pi}(\omega)$, indicating that the deviations from the conventional strong coupling formalism are in fact quite small. It is interesting to notice, that the shoulder in the experimental data at 100 K is reproduced by the same $\tilde{\Pi}(\omega)$ function as the one used to fit the 290 K data. It can be excluded that this shoulder is due to the pseudo-gap, since a gap is certainly absent for temperatures as high as 290 K. The shoulder is therefore due to coupling of the electrons to the 50 - 60 meV feature in $\tilde{\Pi}(\omega)$. On the other hand, the considerable sharpening of this feature for temperatures lower than 100 K finds a natural explanation in the opening of a gap, as illustrated in the inset of Fig. 5.8. The black curve in the inset shows $\Sigma_{opt}(\omega)$ calculated using an expression due to Allen [107] valid at $T = 0$ K. The red curve is calculated in the same approximation but taking into account the opening of a superconducting gap. We emphasize that the peaks of $\tilde{\Pi}(\omega)$ have a one-to-one correspondence with features visible in the experimental $\Sigma_{opt}(\omega)$ data. In particular the broad maximum in $\Sigma_{opt}(\omega)$ has its counterpart in the high amplitude region of $\tilde{\Pi}(\omega)$ terminating at 290 meV as first noted by Norman and Chubukov [140].

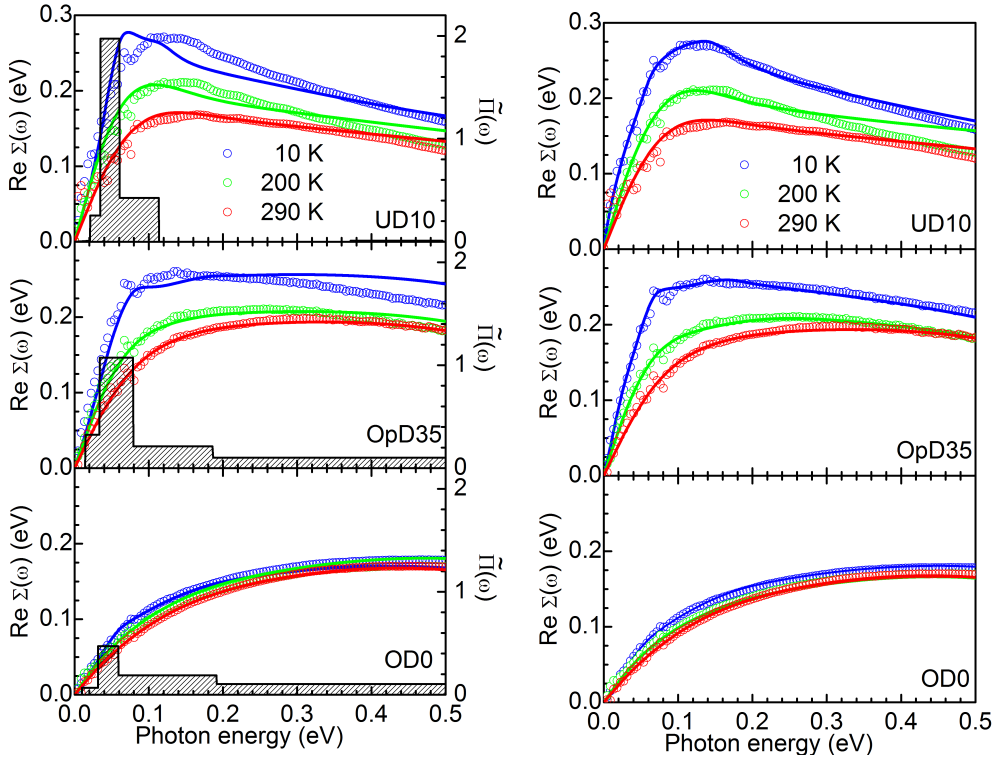

Figure 5.9: Left: Optical self-energy $\Sigma_{opt}(\omega)$ (symbols) together with calculated quantities (solid lines). The shaded area corresponds to the room temperature $\tilde{\Pi}(\omega)$ function used in the calculations. Right: $\Sigma_{opt}(\omega)$ corresponding to glue functions from figure 5.4 compared to experiments. Symbols are experiments and full lines calculations.

In Fig. 5.9 the room temperature $\tilde{\Pi}(\omega)$ spectra are reproduced together with experimental and

calculated optical self energies. The experimental $\Sigma_{opt}(\omega)$ has been determined using the methods of the previous section. We use the $\tilde{\Pi}(\omega)$ spectrum that gives the best fit to the room temperature optical spectra to calculate the optical self-energy at several temperatures. At room temperature the calculated $\Sigma_{opt}(\omega)$ is therefore the best fit to the experimental one based on Eq's 5.2 and 5.4. The reason for choosing the room temperature $\tilde{\Pi}(\omega)$ is that at lower temperatures the spectra might contain features related to the pseudogap. $\Sigma_{opt}(\omega)$ is calculated at 10 K and 200 K by correspondingly changing temperature in Eq's 5.2 and 5.4 but using the same $\tilde{\Pi}(\omega)$ as for 290 K. It is clear from Fig. 5.9 that most of the temperature dependence of the optical spectra can indeed be explained within the strong coupling formalism. The remaining differences (for example, at high energies) can be removed by optimizing the parameters of the histogram at lower temperatures. These results are shown in the right hand panels of Fig. 5.9 where the optical self energies are calculated from $\tilde{\Pi}(\omega)$ functions at corresponding temperatures (displayed in figure 5.4). The temperature dependence of $\tilde{\Pi}(\omega)$ is weak for the OD sample but becomes stronger with decreasing doping.

5.8 Summary

Taken together, our results indicate that the main temperature and frequency dependence of the intra-band response in the cuprates can be understood within the framework of the strong coupling formalism. The only exception we have found is the UD0, Bi2201 sample. Nevertheless, it appears that a significant portion of the high T_c phase diagram can be understood using the analysis presented above. In the next chapter we show that the same formalism can be used to explain the anomalous optical spectral weight transfer in both the normal and superconducting states. A comparison with ARPES experiments gives similar results. We will come back to a discussion of the nature of the $\tilde{\Pi}(\omega)$ functions in chapter 7 but we have already seen that the electron-phonon coupling is not the only contribution to $\tilde{\Pi}(\omega)$. In particular a model that uses the c-axis optical loss function as measure for $\tilde{\Pi}(\omega)$, gives coupling strengths that are three times to small compared to experiments. Another problem with the electron-phonon picture is that the phonon spectrum only extends up to 100 meV, while both ARPES and optical experiments indicate that the electrons couple to bosons with energy up to 400 meV. An interesting question is, whether our observations could be explained by a strongly enhanced electron-phonon coupling due to a strong interaction of the phonons with spin degrees of freedom. Such models have recently been considered in this context [141, 142], and our results may point in this direction as well.

Chapter 6

Temperature dependence of the single band sum rule.

6.1 Introduction

In this chapter we will discuss some implications of the formalism introduced in the previous chapter with regard to the optical spectral weight. The work described in this chapter was published in Ref. [70] and [71].

6.2 Kinetic energy and cut off effects on the optical sum rule

The formalism described in chapter 5 allows us to model the temperature dependence of the optical spectral weight discussed in chapter 2 and 3. The normal state temperature dependence of $W(\omega_c, T)$ increases with decreasing temperature. At the critical temperature there is a sudden change in the temperature dependence of the spectral weight. For overdoped samples $W(\omega_c, T)$ decreases below T_c while the opposite effect happens for optimally and underdoped samples. As we discussed in chapter 2, one interpretation of this effect is that the superconducting transition in the cuprates is driven by kinetic energy saving rather than potential energy as in ordinary BCS theory. However, two studies [143, 46] of the doping dependence of this effect found that above optimal doping the effect changes sign, making this interpretation somewhat unlikely. This makes a second scenario in which the normal state changes as a function of doping more likely [144]. However it can also arise from the finite cutoff frequency ω_c that we have to choose in the experiment. Therefore we have,

$$W(\omega_c, T) = \int_0^{\omega_c} Re\sigma(\omega) d\omega = f(\omega_c) \frac{\omega_{pl}^2}{8} \equiv f(\omega_c) \frac{\pi e^2 a^2}{2\hbar^2 V} E_K \tag{6.1}$$

Here a is the in-plane lattice constant, V the unit cell volume, ω_c an ultraviolet cut-off, ω_{pl} the bare plasma frequency, and

$$E_K = \frac{2}{a^2 N} \sum_k \frac{\partial^2 \epsilon_k}{\partial k_x^2} n_k \tag{6.2}$$

with N the number of k vectors, ϵ_k the bare dispersion as defined by the effective single band Hamiltonian, and n_k the momentum distribution function. The function $f(\omega_c) \leq 1$ accounts for the Drude weight above ω_c. $f(\omega_c)$ equals one if we set the cutoff frequency to infinity. In general, optical integral changes due to E_K (i.e., ω_{pl}) and $f(\omega_c)$ are both present, and the difference of optical integrals at two different temperatures, $\Delta W = W(T_1) - W(T_2)$, goes as

$$\Delta W = \alpha \Delta E_K + \beta \Delta f(\omega_c) \tag{6.3}$$

where α and β are constants. The issue then is which term contributes more to the sum rule violation at a given ω_c. If the variation predominantly comes from E_K, it would be a true sum rule violation, related to the variation of the kinetic energy. If the change of W comes from $f(\omega_c)$, the sum-rule 'violation' would be a cut-off effect, unrelated to the behavior of the kinetic energy. In the next sections we calculate the size of $\beta \Delta f(\omega_c)$ in the formalism described in the previous chapter. We will first consider the case of Einstein modes which is a simplification of the electron-phonon interaction. Then we will consider the case were the electrons interact with a broad spectrum of bosons. Both of these cases can be used to describe the temperature dependence in the normal state. The superconductivity induced transfer of spectral weight will be discussed in the last section.

6.3 Einstein phonons

We want to use Eq. 5.2 to calculate,

$$W(\omega_c, T) = \frac{2}{\pi} \int_0^{\omega_c} d\omega \, \frac{\sigma_1(\omega)}{\omega_P^2/(4\pi)} = 1 - \frac{2}{\pi} \int_{\omega_c}^{\infty} d\omega \, \frac{\sigma_1(\omega)}{\omega_P^2/(4\pi)}. \tag{6.4}$$

Note that Eq. 6.1 implies a temperature independent sum rule for $\omega_c \to \infty$. This is because the derivation of Eq. 5.2 assumes a quadratic dispersion leading to a constant on the right hand side of Eq. 6.2 and hence Eq. 6.1. If the cutoff frequency is much larger then the upper limit of the boson spectrum we can suffice by calculating the conductivity at high energy accurately and use the second equality in Eq. 6.4. Karakozov *et al.* [145, 146] noted that a simple expression for the high energy conductivity could be obtained if one assumed an Einstein phonon spectrum with Debye frequency much smaller than the cutoff. They find,

$$\sigma(\omega) \approx \frac{\omega_p^2/(4\pi)}{1/\tau_\infty - i\omega}, \tag{6.5}$$

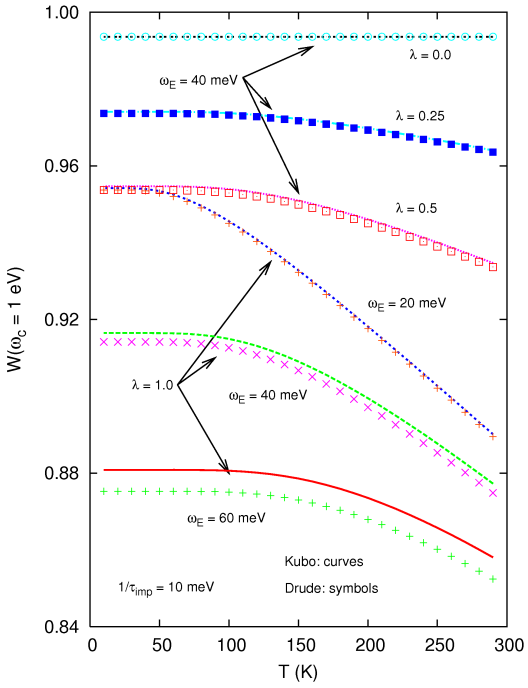

Figure 6.1: The optical spectral weight, integrated up to 1 eV, vs. temperature, for a variety of model parameters. Curves are for results using the Kubo formula, Eq. (5.2), while symbols are for the Drude approximation, Eq. (6.7). The lowest three curves and symbols explore the dependence with boson frequency (fixed coupling strength). Starting from the 2nd lowest curve (indicated to have $\omega_E = 40$ meV), the top three curves explore the dependence on coupling strength. As the coupling strength decreases the temperature dependence diminishes, until there is no temperature dependence (top curve, λ = 0 but finite elastic scattering). That two of the curves merge at low temperature is not a coincidence; they have the same $\lambda\omega_E$ product, and therefore have the same low temperature sum rule result (see Eq. (6.6) with an Einstein spectrum substituted for $\alpha^2F(\Omega)$). Figure taken from Ref. [71].

where

$$1/\tau_\infty(T) \equiv 1/\tau_{\rm imp} + 2\pi \int_0^\infty d\Omega \Pi(\Omega) \coth\left(\frac{\beta\Omega}{2}\right). \tag{6.6}$$

The partial sum rule, Eq. 6.4 can then be integrated analytically, and one obtains

$$W_{\rm Dr}(\omega_c) \approx (2/\pi)\tan^{-1}\left(\frac{\omega_c}{1/\tau_\infty(T)}\right). \tag{6.7}$$

This approximation turns out to be accurate enough if one wants to calculate the optical conductivity at high energy [71]. In Fig. 6.1 we show $W(\omega_c = 1 \text{ eV}, T)$ as a function of temperature calculated using the full Kubo expression and the approximation Eq. 6.7. We used $\Pi(\omega) = \frac{\lambda\omega_0}{2}\delta(\Omega - \omega_0)$ and a finite impurity scattering rate $1/\tau_{\rm imp} = 10$ meV. Note that in *all* cases the integral shown approaches unity for $\omega_c \to \infty$. We observe from Fig 6.1 that in the absence of inelastic scattering (λ = 0) there is no temperature dependence. The full sum rule is not completely fulfilled, due to the non-zero elastic scattering rate. The other curves show the effect of increasing λ with fixed ω_0. The overall

spectral weight decreases with increasing coupling, while the temperature dependence also increases. Moreover, the Drude approximation (shown with symbols) is less accurate as boson coupling increases. Keeping the coupling strength fixed while increasing the boson frequency (lower three curves), the sum rule violation becomes larger and the temperature dependence diminishes. For boson frequencies larger than roughly 50 meV the Drude result becomes less accurate as can be seen from the difference between the symbols and full curves. The most important point to be taken away from Fig. 6.1 is that the temperature dependence introduced by taking a finite cutoff frequency is large enough to explain the temperature dependence seen in experiments.

6.4 Gapped MFL and MMP models

Shulga *et al.* derived a finite temperature expression for the frequency dependent scattering rate [147],

$$1/\tau(\omega) = 2\Gamma_i + \frac{1}{\omega}\int_0^\infty d\Omega\Pi(\Omega)[2\omega\coth(\frac{\Omega}{2T}) \\ -(\omega+\Omega)\coth(\frac{\omega+\Omega}{2T}) + (\omega-\Omega)\coth(\frac{\omega-\Omega}{2T})]. \tag{6.8}$$

This expression allows us to calculate $W(\omega_c, T)$ analytically for the MFL and MMP models discussed above. We again write the sumrule as,

$$W(\omega_c, T) = W(\infty) - \int_{\omega_c}^\infty Re\sigma(\omega, T)d\omega \tag{6.9}$$

where $W(\infty) = \omega_{pl}^2/8$. The optical conductivity that we use here is the extended Drude expression Eq. 2.125 together with Eq. 6.8. The effective mass is calculated from Eq. 6.8 by Kramers - Kronig transform. The derivation of the analytical results follows that of Ref. [70]. We first consider a modified version of the MFL expression,

$$\Pi(\Omega)_{GMFL} = \frac{\Gamma}{\omega_2-\omega_1}\Theta(\Omega-\omega_1)\Theta(\omega_2-\Omega) \tag{6.10}$$

with a lower cut-off ω_1 put in by hand to prevent divergencies and a spectrum that is flat in frequency up to an upper cut-off ω_2. Γ determines the overall size of the self-energy. Note that for ω larger than the upper cut-off ω_2 of the gapped marginal Fermi liquid model [140],

$$1/\tau = 1/\tau_{high} = 2\Gamma_i + \frac{\Gamma}{\omega_2-\omega_1}(4T\ln\frac{\sinh\frac{\omega_2}{2T}}{\sinh\frac{\omega_1}{2T}} - \frac{\omega_2^2-\omega_1^2}{\omega}) \tag{6.11}$$

For $T << \omega_2$ and $\omega_1 << \omega_2$, this reduces to

$$1/\tau_{high} = 1/\tau_0 - \frac{4\Gamma T}{\omega_2}\ln(1-e^{-\omega_1/T}) \tag{6.12}$$

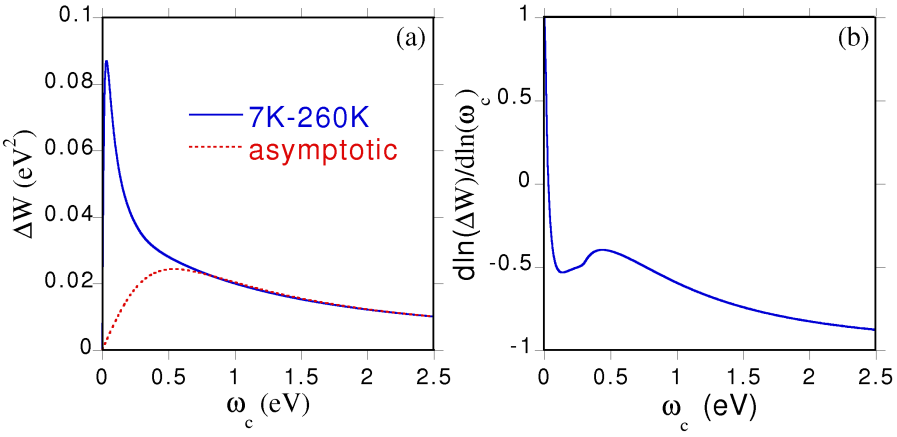

Figure 6.2: (a) Optical integral difference calculated numerically from Eq. 6.8 versus ω_c as compared to the asymptotic result Eq. 6.13. (b) Logarithmic derivative of ΔW versus the cut-off. Figure adapted from [70].

where $1/\tau_0 = 2\Gamma_i + 2\Gamma - \Gamma\omega_2/\omega$. Ignoring the frequency dependence of $1/\tau_0$, and setting m^* to 1 ($\omega_c >> \omega_2$)[1], we then obtain $\Delta W(\omega_c) = \frac{\omega_{pl}^2}{4\pi}\Delta(\tan^{-1}(\omega_c\tau_{high}))$ where again $\Delta W(\omega_c) = W(\omega_c, T_1) - W(\omega_c, T_2)$. Expanding in ΔT, we obtain

$$\Delta W(\omega_c) = \frac{\omega_{pl}^2}{2\pi\omega_2}\frac{\omega_c^*}{1+(\omega_c^*)^2}\Delta\left(T\ln(1-e^{-\omega_1/T})\right) \tag{6.13}$$

where $\omega_c^* = \omega_c/(2\Gamma)$. In Fig. 6.2, we plot Eq. 6.13 together with the calculated optical integral difference from Eq. 6.8, and see that they match for cut-offs that are typical for experiments. Experiments typically show a quadratic temperature dependence but the dependence from Eq. 6.13 is $T\ln(1-e^{-\omega_1/T})$, however this is close to T^2 over a wide range of temperatures.

For the MMP model we find the temperature dependence of the scattering rate to be,

$$1/\tau(T) = 1/\tau_0 + 4\Gamma\int_0^\infty \frac{xdx}{x^2+1}\frac{1}{e^{x/T^*}-1} \tag{6.14}$$

where $1/\tau_0 = 2\Gamma\ln\frac{\sqrt{\Omega_c^2+\gamma^2}}{\gamma}$ with $T^* = T/\gamma$, and Ω_c is the upper cut-off for Π_{MMP}. Assuming that $\Omega_c >> \gamma$, we have $\Delta W(\omega_c) = \frac{\omega_{pl}^2}{4\pi}\Delta(\tan^{-1}(\omega_c\tau))$. Expanding around $T = 0$, we obtain

$$W(\omega_c, T) \approx W(\omega_c, T=0) - \frac{\omega_{pl}^2}{4\pi}\,C\,(T^*)^2 \tag{6.15}$$

where

$$C = \frac{\pi^2}{6}\frac{\omega_c}{\Gamma\ln^2(\Omega_c/\gamma)}\frac{1}{1+\left(\frac{\omega_c}{2\Gamma\ln(\Omega_c/\gamma)}\right)^2} \tag{6.16}$$

1. Corrections from the optical mass lead to higher order terms in W of the form $\ln(\omega_c)/\omega_c^3$.

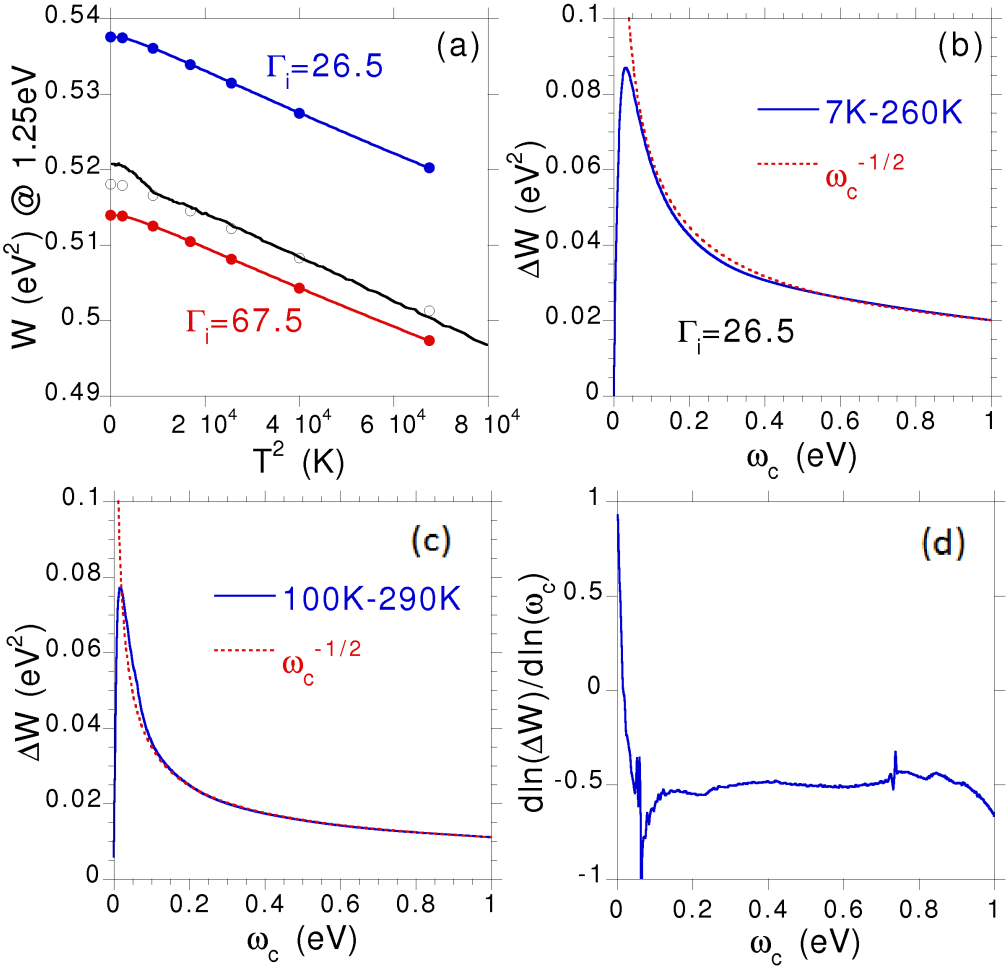

Figure 6.3: (a) Temperature dependence of Bi2212 from Ref. [45] vs. T^2 (black line). The other solid curves are calculated from Eq. 6.8 while the circles are from Eq. 6.13, using Π_{MFL} with Γ = 270.5 meV, ω_1 = 15.5 meV, ω_2 = 301 meV. We consider two cases one with and the other with Γ_i = 67.5 meV but both with the same overall ω_p = 2.4 eV. The open circles correspond to Γ_i = 26.5 meV and ω_p = 2.4 eV. (b,c) ω_c dependence of ΔW for the calculation with (b): Γ_i = 26.5 meV and for (c): Hg-1201. In both cases the dashed line represents a $1/\sqrt{\omega_c}$ dependence. (d) Logarithmic derivative of ΔW for Hg-1201 from panel (c). Figure adapted from [70].

This time, we find a truly quadratic behavior in T [1], which is a consequence of the fact that Π_{MMP} is linear in ω at small ω.

In figure 6.3 we display calculations and experimental results for Bi2212 and Hg1201 [45, 50, 70]. Figure 6.3a shows a comparison between temperature dependencies calculated with Eq. 6.8 (lines) and the analytic result from Eq. 6.13 (symbols) for two values of the impurity scattering rate. The experimental temperature dependence of the spectral weight can be reproduced (note ΔE_k = 0) by

1. This T^2 behavior holds for $T^* < 1/3$. For higher T, the behavior of $W(\omega_c, T)$ crosses over to a linear T behavior.

slightly adjusting the plasma frequency in the calculation. Panel (b) shows the temperature difference between 260 K and 7 K for the calculated spectral weight. Also shown is a $1/\sqrt{\omega_c}$ dependence, which matches the calculated one over a reasonable frequency range. Note that in the simple Drude result one expects a $1/\omega_c$ behavior instead. Panel (c) shows the experimental ΔW behavior for Hg1201. Together with the logarithmic derivative in panel (d) we see that the experimental data is also very close to a $1/\sqrt{\omega_c}$ behavior. From these observations, we conclude that the dominant contribution to the T dependence of the optical integral in the normal state can be attributed to the finite cut-off. The true sum rule 'violation' term ΔE_K is estimated to be no larger than $\sim 20\%$ of ΔW, as noted above. Although we do not expect our analysis to be the entire story, in light of the evidence that $\tilde{\Pi}(\omega)$ is T dependent, even though this dependence is weak in the normal state, still, based on the good agreement of the calculations with experiment, we would argue that the bulk of the observed T dependence in the normal state is related to the finite cut-off.

6.5 The superconducting state

The question that remains is which term dominates when the system enters the superconducting (SC) state. This question is much harder to answer. The change at the superconducting transition is small: there is only a 1 % difference between the extrapolated normal state and superconducting spectral weight. We focus on the T = 0 limit since this will give the largest difference between normal and superconducting state. Karakozov *et al.* [145] considered the Mattis-Bardeen limit [148]. In this limit analytic expressions for the conductivity are available. The high frequency limit of the conductivity is given by,

$$\frac{\sigma_S(\omega)}{\sigma_0} \approx 1 - \left(\frac{\Delta_0}{\omega}\right)^2 \big[1 + 2\log\frac{2\omega}{\Delta_0}\big]. \tag{6.17}$$

We are interested in calculating,

$$\Delta W(\omega_c) = -\int_{\omega_c}^{\infty} d\omega\ (\sigma_S(\omega) - \sigma_N(\omega)), \tag{6.18}$$

which together with Eq. 6.17 gives,

$$\frac{\Delta W(\omega_c)}{W_N(\omega_c)} \approx \left(\frac{\Delta_0}{\omega_c}\right)^2 \big[3 + 2\log\frac{2\omega_c}{\Delta_0}\big]. \tag{6.19}$$

This result suggests that in the Mattis-Bardeen limit $W(\omega_c, T)$ *increases* in the SC state. The effect is of the same order of magnitude and even somewhat larger as observed in experiments [71]. This suggests that non of the experimental observations are anomalous, but it turns out that the dirty limit is not the generic case for for what happens in the SC state.

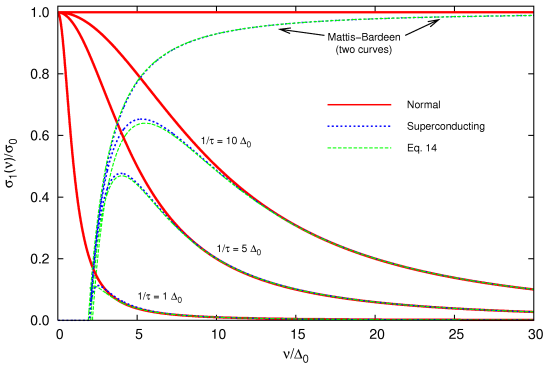

Figure 6.4: Optical conductivity normalized to $\sigma_0 \equiv \frac{\omega_p^2}{4\pi}\tau$. Solid red curves are normal state results for a Drude model with varying values of the scattering rate. Blue dotted lines are from Eq. 6.20 while green dashed curves are from Eq. 6.21. Also shown is the Mattis-Bardeen result. Remarkably, the approximate result is very close to the numerical result. Figure adapted from Ref. [71].

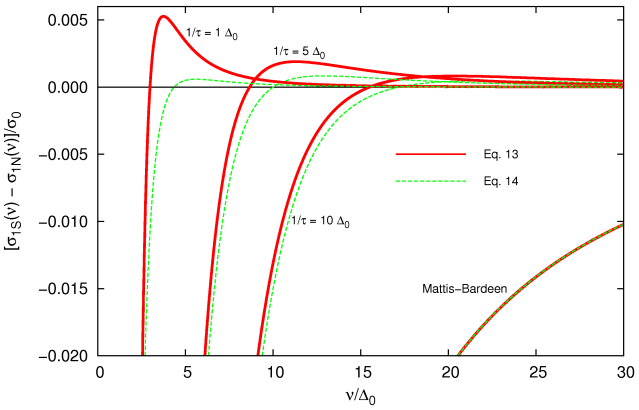

Figure 6.5: Difference between superconducting and normal state conductivity normalized to σ_0. We see that while the Mattis-Bardeen result is always negative, for finite scattering rate there is a zero crossing of the difference. This effect was first observed by Chubukov *et al.* . [149]. Figure adapted from Ref. [71].

If we consider a non infinite scattering rate the result turns out to be somewhat different. We will consider the following (T = 0) expression valid for any scattering rate [150, 151, 152],

$$\sigma_1(\omega) = \frac{ne^2}{m}\frac{1}{2\omega}\mathrm{Im}\int_{\Delta_0}^{\omega-\Delta_0} d\omega \quad \left\{\frac{1+N(\omega)N(\omega-\omega)-P(\omega)P(\omega-\omega)}{\epsilon(\omega-\omega)+\epsilon(\omega)-i/\tau} - \frac{1-N(\omega)N(\omega-\omega)+P(\omega)P(\omega-\omega)}{\epsilon(\omega-\omega)-\epsilon(\omega)-i/\tau}\right\}, \tag{6.20}$$

where we have used $\epsilon(\omega) \equiv \sqrt{\omega^2-\Delta_0^2}$, and $N(\omega) = \omega/\epsilon(\omega)$ and $P(\omega) = \Delta_0/\epsilon(\omega)$, and all quantities in Eq. (6.20) are real except for the explicit imaginary i/τ in the denominators. For high frequency we can obtain an approximate expression by expanding to second order in Δ_0/ω,

$$\frac{\sigma_{1S}(\omega)}{\sigma_0} \approx \frac{(1/\tau)^2}{\omega^2+(1/\tau)^2}\left(1-2\left(\frac{\Delta_0}{\omega}\right)^2\left[1+\log\frac{2\omega}{\Delta_0}\right]-2\frac{\Delta_0^2}{\omega^2+(1/\tau)^2}\left[1-2\log\frac{2\omega}{\Delta_0}\right]\right). \tag{6.21}$$

In figures 6.4 and 6.5 we compare the numerical and approximate results. We see that the approximate result is very close to the full numerical result down to low frequency. The Mattis-Bardeen result is also shown in these graphs. In this case the normal state result is always higher than the superconducting result as expected. For a finite scattering rate the conductivity is lower than the normal state conductivity, up to a frequency close to the value of the scattering rate where the SC state conductivity becomes larger than the normal state. This result was first obtained by Chubukov *et al.* [149]. The effect is small as emphasized by the vertical scale of figure 6.5 but comparable to what is seen in experiments. We are now in a position to estimate the effect of opening a superconducting gap on the spectral weight.

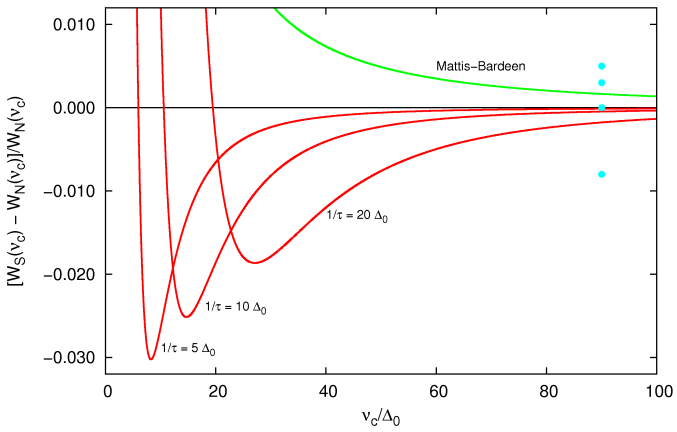

Figure 6.6: Normalized difference of the spectral weight. The red curves show the finite scattering rate result while the Mattis-Bardeen limit is indicated by the green curve. Also shown are the experimental results for Bi2212 from [46] (blue symbols). Figure adapted from Ref. [71].

The result is shown in figure 6.6. We see that for finite scattering rate the effect is to decrease the spectral weight compared to the normal state trend. This is in most cases opposite to what is observed in experiments as indicated by the blue symbols. There is one exception: the overdoped Bi2212 sample which shows a decrease of $W(\omega_c, T)$ at T_c consistent with the BCS prediction [143, 46].

To summarize, we have investigated the effect of a finite cutoff on the calculation of the optical spectral weight in both the normal and superconducting state. In the normal state we find that the strong temperature dependence of $W(\omega_c, T)$ indicates that the cutoff effect dominates for electrons coupled to a broad spectrum of bosons. The opposite is true for the superconducting state where the results from BCS theory in the clean limit indicate that the spectral weight decreases when the system enters the superconducting state.

Chapter 7

A minimal model of high temperature superconductivity.

7.1 Introduction

In this final chapter I present a comprehensive analysis of the optical properties of hole doped high T_c superconductors. I extend the analysis of previous chapters to Bi2212 [45, 46] and Bi2223 [47]. From the comparison I derive a minimal model for the bosonic spectral density $\tilde{\Pi}(\omega)$ and show that this model can explain most of the experimental observations including the high critical temperature of these compounds.

7.2 Electron-boson coupling in other cuprates

The analysis of optical spectra belonging to different families of cuprates, *i.e.* $Bi_2Sr_2Ca_2Cu_3O_{10+\delta}$ (Bi-2223) [47], as well as four $Bi_2Sr_2CaCu_2O_{8+\delta}$ (Bi-2212) crystals [45, 46] with different hole concentrations, has been repeated along the same lines as discussed in chapter 5 for Hg1201 and Bi2201. In figure 7.1 we show a comparison of the reflectivity for optimally doped Bi2201 (T_c = 35 K), Bi2212 (T_c = 88 K) and Bi2223 (T_c = 110 K). The right hand panels show the reflectivity in the far infrared (IR) region of the spectrum. For all three compounds the room temperature reflectivity follows the Hagen-Rubens behavior at low frequency. At the lowest temperatures all three compounds are in the superconducting state and the reflectivity is very close to unity at low frequency. The point where $R(\omega)$ departs from unity clearly shifts to higher frequency with increasing critical temperature, which reflects the increase in the superconducting gap size. Using the point where $R(\omega)$ departs from unity as a rough measure for 2Δ, we find a ratio of $2\Delta/k_bT_c \approx$ 5 - 6 in all three cases. Another feature that becomes more pronounced with increasing number of layers is the "dip" just above the the point

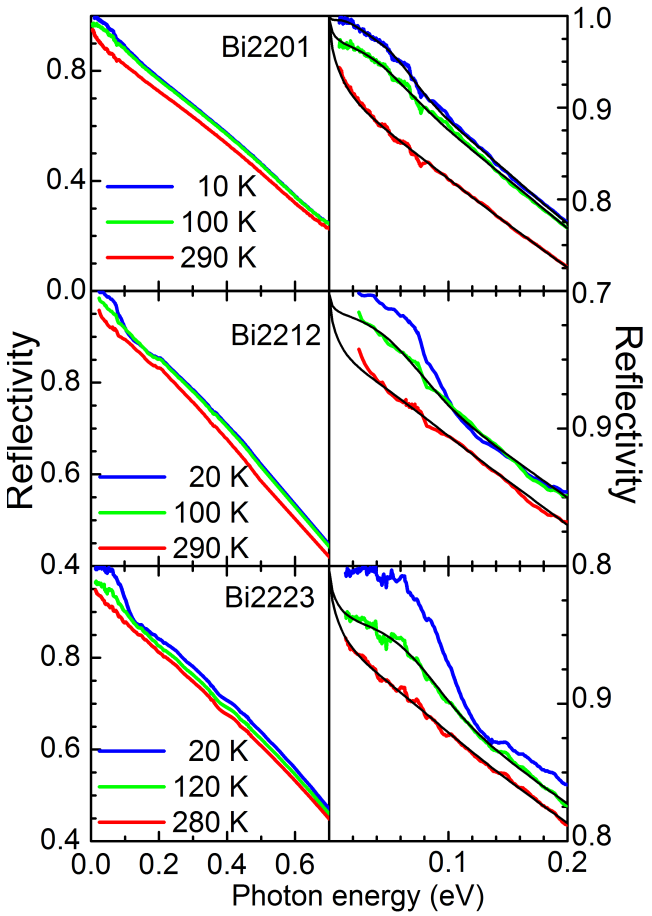

Figure 7.1: Left: Reflectivity for optimally doped Bi2201, Bi2212 and Bi2223 at selected temperatures. Right: The far IR region on an enlarged scale together with fits (black lines) to the experimental data. We only made fits at temperatures above the critical temperature, except for Bi2201. In this case the gap quite small and the effect on the resulting $\tilde{\Pi}(\omega)$ function should be small.

where departs $R(\omega)$ from unity. This feature has been discussed extensively in the literature [81]. It is believed to arise from a combined effect of electrons coupling to bosonic modes and the pseudo-gap or superconducting gap. We used the method of chapter 5 to extract a $\tilde{\Pi}(\omega)$ function from the normal state reflectivity and ellipsometry data of these compounds. Some representative fits to the reflectivity are shown as black lines in figure 7.1. In the case of the OpD35, Bi2201 sample we also show a fit to the superconducting 10 K data. In this case the gap is quite small and its influence on the analysis relatively unimportant. We collect the $\tilde{\Pi}(\omega)$ functions for all samples in figure 7.2. The $\tilde{\Pi}(\omega)$ spectra show significant temperature dependence for all samples. Such temperature dependence is a direct consequence of the peculiar DC and far infrared conductivity, in particular the T-linear DC resistivity and ω/T scaling of $T\sigma(\omega, T)$ at optimal doping [74]. With increasing doping the temperature dependence diminishes, which is an indication that a more conventional Fermi liquid regime is approached. As dis-

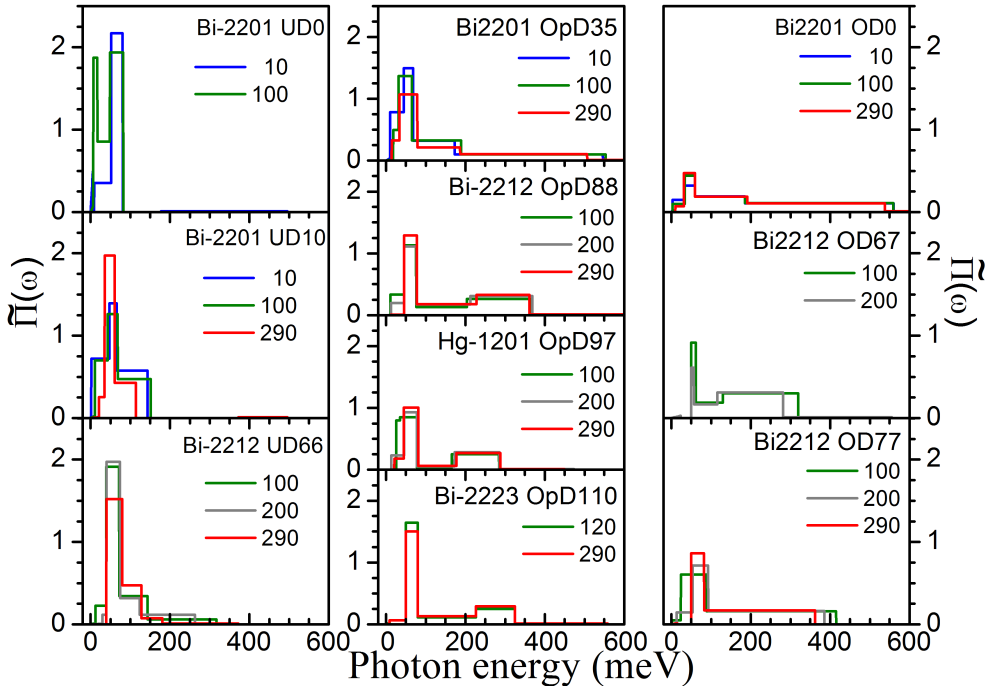

Figure 7.2: Electron-boson coupling function $\tilde{\Pi}(\omega)$ for Bi-2201 at four different charge carrier concentrations, Bi-2212 at four charge carrier concentrations, and optimally doped Bi-2223 and Hg-1201. The spectra are organized according to doping (UD, OpD and OD, left to right) and T_c (top to bottom).

cussed above the most strongly underdoped sample, Bi2201-UD0, exhibits an upturn of the imaginary part of the experimental optical self-energy for $\omega \to 0$. This aspect of the data can not be reproduced by the Eliashberg expression, resulting in an artificial and unphysical peak at $\omega \approx 0$ of the fitted $\tilde{\Pi}(\omega)$ function.

We observe two main features in the glue-function for all samples: A robust peak at 50-60 meV and a broad continuum. The upper limit of $\tilde{\Pi}(\omega)$ is situated around approximately 300 meV for the optimally doped bilayer and trilayer samples. The continuum extends to somewhat higher energy for overdoped samples (550 meV for the Bi2201 and 400 meV for the Bi2212 sample), while there is a clear contraction of the continuum to lower energies when the carrier concentration is reduced. An important observation is that the glue function has an energy well above the upper limit of the phonon frequencies in the cuprates ($\sim$ 100 meV). Consequently, the high energy part of $\tilde{\Pi}(\omega)$ reflects in one way or another the strong coupling between the electrons themselves, which may require a theoretical treatment beyond the strong coupling expansion outlined in chapter 2. This implies that the $\tilde{\Pi}(\omega)$ function obtained in our study should be interpreted as a representation of *all* interaction processes relevant for these strongly interacting electron systems.

As discussed before (section 5.7), in the standard Eliashberg formalism one does not expect $\tilde{\Pi}(\omega)$ to be temperature dependent. In principle the temperature dependence should be folded out by the

Fermi and Bose factors appearing in the expressions for the self-energy and conductivity. There are several reasons why $\tilde{\Pi}(\omega)$ nevertheless could acquire a temperature dependence. One reason could be that we have not taken into account the effect of a (pseudo)gap. Our method ignores any energy dependence of the density of states or the presence of a gap in the electronic spectrum. If at some temperature a gap opens, then our method will try to accommodate for the changes in the experimental data by adjusting the boson spectrum. Another possibility is a feedback effect: if $\tilde{\Pi}(\omega)$ is made up out of low energy bosons, which derive from integrating out high energy electron degrees of freedom, then changing temperature will induce temperature dependence in $\tilde{\Pi}(\omega)$ due to changes in the electron distribution function with temperature. This effect can be particularly large if at a certain temperature a gap opens up in the electronic spectrum. For example, in the spin fluctuation theory the low energy bosons are spin fluctuations. In the normal, ungapped state the spin modes are diffusive and form a broad featureless spectrum (see Eq. 5.11). When a gap opens up in the electronic spectrum the effect on the spin fluctuation spectrum is substantial: the continuum also becomes gapped and a propagating spin mode is formed in the gap [153]. This example demonstrates that the temperature dependence can arise from a complicated interplay of several factors.

In chapter 5 we showed that the temperature dependence of the optical spectra could by and large be explained assuming a temperature *independent* $\tilde{\Pi}(\omega)$ function. The remaining small discrepancies between experiment and calculation arise from the temperature dependence of $\tilde{\Pi}(\omega)$. Figure 7.3 shows the optical self energy for optimally doped Bi2201, Bi2212 and Bi2223. In each case we use the room temperature $\tilde{\Pi}(\omega)$ function to calculate the optical self energy at lower temperatures. The comparison between experiment and calculation is almost perfect for the Bi2212 and Bi2223 samples. The less good fit for the Bi2201 sample is reflected by the strong temperature dependence of the $\tilde{\Pi}(\omega)$ function in this case (see fig. 7.2), while the good fit at low temperatures in the other two cases reflects the weak temperature dependence of $\tilde{\Pi}(\omega)$. Another interesting feature in the optical self energy is the peak around 100 meV, which can be most clearly seen in the superconducting state. This peak can be directly related to the "dip" in the reflectivity mentioned above. Figure 7.3 clearly shows that this structure arises from the coupling to a bosonic mode at 50 - 60 meV, evidenced by the shoulder seen in the calculations. Above T_c this allows to perfectly reproduce the experimental $\Sigma_{opt}(\omega)$. Below T_c the experimental peak is more pronounced than predicted by our calculation. The origin of this discrepancy can be found in the opening of the superconducting gap as shown in figure 5.8. This effect is largest for Bi2223, for which we know the superconducting gap to be largest. For Bi2223 we also discern a slight shift of the maximum to higher energy in the 20 K curve. This is expected: in an s-wave superconductor one expects this maximum to occur at $2\Delta + \omega_0$, where ω_0 is the energy of a sharp boson mode. In the cuprates this shift is never exactly observed. A possible reason for this could

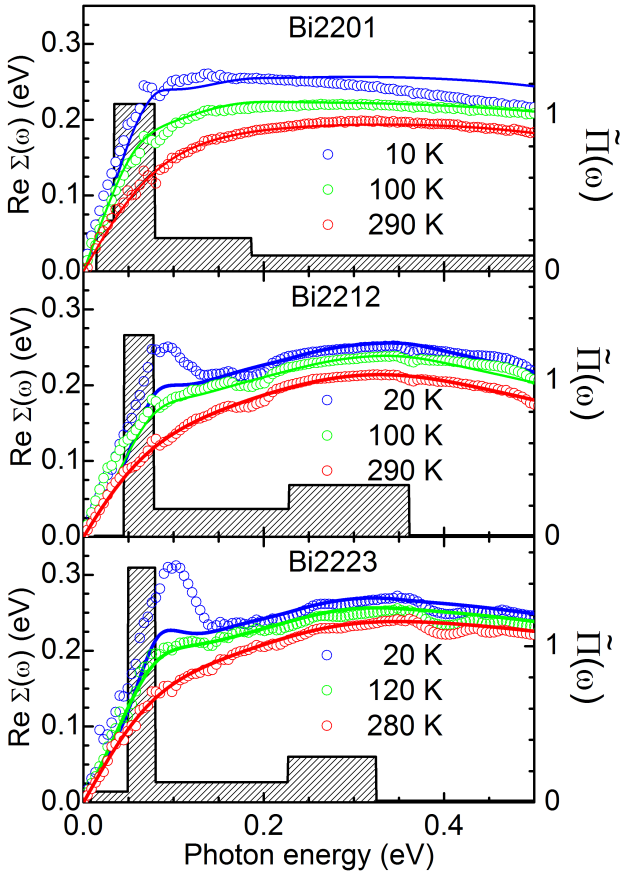

Figure 7.3: Experimental $\Sigma_{opt}(\omega)$ for optimally doped Bi2201, Bi2212 and Bi2223 (symbols). Also shown are the $\Sigma_{opt}(\omega)$ calculated from the $\tilde{\Pi}(\omega)$ function indicated by the shaded area.

be that the gap is not a full s-wave gap and the momentum dependence may change or smear out the onset energy of scattering.

Another feature born out by figure 7.3 is a one to one correspondence between structure in $\tilde{\Pi}(\omega)$ and structure in $\Sigma_{opt}(\omega)$ [140]. We already discussed the correspondence between the low energy peak and the maximum in the low temperature $\Sigma_{opt}(\omega)$. In the Bi2212 and Bi2223 $\tilde{\Pi}(\omega)$ function there is a second maximum around 300 meV. This maximum is reflected in a maximum in $\Sigma_{opt}(\omega)$. In the case of Bi2201 the continuum appears to have a maximum at lower energy (just above the low energy peak) and this is reflected in a $\Sigma_{opt}(\omega)$ that is slowly decreasing at high energy. Before turning to an interpretation of our results we first compare our observations to what is found in other experiments and using other methods of data inversion.

7.3 Comparison with other optical experiments.

Hwang *et al.* have investigated the coupling to bosonic modes by analyzing the optical scattering rates of Bi-2212 [117, 84, 154, 155, 156, 157], YBCO [158] and LSCO [159]. Several other groups have applied different methods of analysis to optical spectra with similar results but differing interpretations [160, 161, 162, 163, 164, 165, 166, 111, 167, 168]. Several other techniques, like ARPES [127, 119, 128, 118, 131, 132, 169, 120, 133, 95, 129, 130] and tunneling [136, 137, 170, 138], also show evidence for coupling of electrons to bosonic modes as discussed in section 5.6.

We first compare our results with other optical experiments. Most authors find a spectral function consisting of two contributions: a peak below 100 meV and structure in the 200 - 300 meV range. The doping trend of $\Sigma_{opt}(\omega)$ seen in Fig. 5.9 is similar to the one observed in Ref. [154] for $Bi_2Sr_2CaCu_2O_{8+\delta}$, namely that $\Sigma_{opt}(\omega)$ is a broad and featureless function for high dopings and becomes peaked and narrow for lower dopings. These authors apply an analysis [155] similar to ours and also find an overall decrease in intensity in $\tilde{\Pi}(\omega)$ with increasing doping (note that in Ref. [155] the notation $I^2\chi(\omega)$ is used instead of $\tilde{\Pi}(\omega)$). In figure 7.4 we compare our result for optimally doped Bi2212 to the result obtained by Hwang *et al.* . The main difference that appears from fig. 7.4 is that we

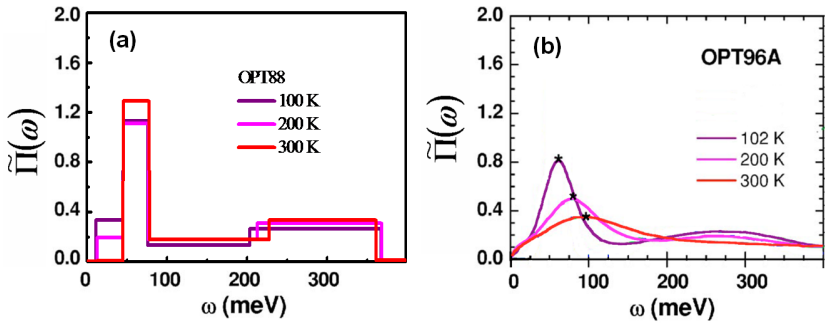

Figure 7.4: Comparison of the $\tilde{\Pi}(\omega)$ functions obtained by (a): our analysis and (b): the analysis of Ref. [155]. The samples are both optimally doped but the sample in panel (b) has Y mixed in.

find the spectra to be much less temperature dependent in the low energy region of $\tilde{\Pi}(\omega)$, in agreement with the results obtained by Dordevic *et al.* [111]. Hwang *et al.* explain the temperature and doping dependence of these spectra as arising from the presence of a pseudogap at lower temperatures for the underdoped samples [157]. The analysis in Fig. 5.8 and 5.9 allows another interpretation. The peak in $\Sigma_{opt}(\omega)$ at low doping arises from the coupling to a bosonic mode. This peak is smeared out at higher temperatures by the Bose and Fermi factors appearing in Eq's 5.2 and 5.4. The peak in $\Sigma_{opt}(\omega)$ disappears with increasing doping simply because the coupling to low energy bosonic modes gets weaker. The temperature effect is much more pronounced in fig. 5.8 and fig. 7.3 where the low energy peak in $\Sigma_{opt}(\omega)$ is more clearly visible. Although there is no simple relation between the energy of a peak seen in $\Sigma_{opt}(\omega)$ and one seen in $\tilde{\Pi}(\omega)$ a pseudogap would shift the peak in $\Sigma_{opt}(\omega)$ to higher energies as

compared to the peak in $\tilde{\Pi}(\omega)$. We note that the experimental $\Sigma_{opt}(\omega)$ for underdoped Bi2201 (where the pseudogap is expected to be largest) shows the opposite trend, i.e. the peak in $\Sigma_{opt}(\omega)$ shifts to *lower* energy with decreasing temperature. The only case where there is a clear shift of the low energy peak in $\Sigma_{opt}(\omega)$ is that of Bi2223 in the superconducting state. Our analysis thus shows that features in the optical spectra which have been attributed to the opening of a pseudogap [22, 157] can in fact be explained by a nearly temperature independent peak in $\tilde{\Pi}(\omega)$ in the 50 - 60 meV range.

7.4 Other inversion methods.

There are many ways to "invert" Eq.'s 5.2 and 5.4. Since there exists no unique solution to this ill-posed problem it is easy to imagine that different methods will give quite different results. A comparison of results from different methods would therefore be very useful. Such an analysis was presented in Ref. [171] were different methods were tested using model calculations. Here we compare our method to two other methods of extracting $\tilde{\Pi}(\omega)$, and show how the results change when these methods are applied to the same experimental data. The first method is due to Dordevic *et al.* [111] and the second is due to Schachinger *et al.* [171]. We first briefly recapitulate these methods and then compare results obtained from an analysis of the Hg-1201 data presented in chapter 3. I am indebted to both S. Dordevic and E. Schachinger who analyzed the Hg1201 experimental data using their inversion method.

The method by Dordevic *et al.* is based on a direct inversion of the optical scattering rate. They consider the finite temperature form for the scattering rate derived by Shulga *et al.* [147], Eq. 6.8. This expression can be written as [111],

$$\frac{1}{\tau(\omega,T)} = \int_0^\infty d\Omega \Pi(\Omega) K(\omega,\Omega,T) \tag{7.1}$$

where $1/\tau(\omega,T)$ has been determined experimentally, $K(\omega,\Omega,T)$ is a kernel and $\Pi(\Omega)$ is the function to be determined. This expression can be inverted numerically, provided that we discretize Eq. 7.1,

$$\frac{1}{\tau(\omega_i,T)} = \sum_{j=1}^{N} \Delta\Omega_j \Pi(\Omega_j) K(\omega_i,\Omega_j,T) \tag{7.2}$$

where i runs over the number of data points. This is a simple matrix equation and the problem is reduced to finding the inverse of the matrix $K(\omega_i,\Omega_j,T)$. Dordevic *et al.* do the inversion using a singular value decomposition (SVD), in which the matrix K is decomposed into three matrices K = USV^T. U and V are orthogonal matrices such that $U^T = U^{-1}$ and $V^T = V^{-1}$ while the matrix S is a diagonal matrix with elements w_j that are called the singular values off the matrix K. The inverse of K is than given by $K^{-1} = VS^{-1}U^T$. Once this decomposition has been made we can calculate the solution of the inversion problem. If all the singular values of K are kept in the inversion the method is exact but usually noisy [111]. The *solution* can be smoothed if we replace the largest $1/w_j$ by zeroes.

How many singular values should be kept to make an accurate inversion cannot be determined *a priori* so usually there is a trade off between noise in the solution and maximum number of singular values. A big advantage of this method is that it is very easy to generalize for different forms of the kernel K. For example, Dordevic *et al.* also consider the superconducting state where the kernel is given by,

$$K(\omega,\Omega,T)=\frac{2\pi}{\omega}\left(\omega-\Omega\right)E\left(\sqrt{1-\frac{4\Delta^2}{\left(\omega-\Omega\right)^2}}\right) \tag{7.3}$$

The big disadvantage is that the method allows for "unphysical" output: the $\tilde{\Pi}(\omega)$ functions derived with this method contain negative values. Dordevic *et al.* attribute these negative values to two different aspects of the analysis. Firstly there is the issue of numerical accuracy, and secondly there is the possibility that not all the physics is captured by Eq.' 7.1. In the first case the negative parts can usually be removed by using more singular values in the inversion process. In the second case the negative parts could have a physical origin. For example they could arise from a (pseudo) gap in the spectrum that has not been taken into account.

The second method is the one used by Schachinger *et al.* based on the maximum entropy method (MaxEnt) [171]. Since there are many solutions to the inversion problem, Eq. 7.1, that fit $1/\tau(\omega)$ within the experimental error bars, one can define a probability distribution $p(\mathbf{a}|\mathbf{t},\mathcal{I})$ of possible solutions $\mathbf{a}$ for the dataset $\mathbf{t}$. $\mathcal{I}$ contains information on the problem like the form of the kernel in Eq. 7.1. Bayes' theorem allows us to relate this probability to three other probabilities,

$$p(\mathbf{a}|\mathbf{t},\mathcal{I})=\frac{p(\mathbf{t}|\mathbf{a},\mathcal{I})p(\mathbf{a}|\mathcal{I})}{p(\mathbf{t}|\mathcal{I})} \tag{7.4}$$

$p(\mathbf{a}|\mathcal{I})$ is known as the *prior*: the probability to find the solution $\mathbf{a}$ given $\mathcal{I}$ without knowledge of the experimental data. The probability that we want to calculate, $p(\mathbf{a}|\mathbf{t},\mathcal{I})$ is called the *posterior* and Eq. 7.4 tells us that it is proportional to finding the most probable solution $\mathbf{a}$ without knowledge of the data. The proportionality factor $p(\mathbf{t}|\mathbf{a},\mathcal{I})$ is known as the *likelihood* function. It gives a measure of how probable a solution $\mathbf{a}$ is given knowledge of the experimental data $\mathbf{t}$ and an estimate of the error bars of the measurement of $\mathbf{t}$. $p(\mathbf{t}|\mathcal{I})$ normalizes the posterior probability. In the case considered here the likelihood function we are interested in is $p(\mathbf{t}|\mathbf{t_0},\mathcal{I})$ where $\mathbf{t_0}$ is the model vector with elements $\mathbf{t_{0,i}}=1/\tau(\omega_i)$ calculated from input parameters a_j. We now make the assumption that,

$$p(\mathbf{t}|\mathbf{t_0},\mathcal{I})=\frac{1}{(2\pi\sigma)^{N/2}}\exp\left(-\frac{\chi^2}{2}\right) \tag{7.5}$$

which is a normal distribution with standard deviation σ of the χ^2 (χ^2 is given by Eq. 5.14). The most uninformative prior is given by [172],

$$p(\mathbf{a}|\alpha,\mathcal{I})=\frac{1}{\prod_{j=1}^{N}\sqrt{a_j}}\exp\left(-\alpha S\right) \tag{7.6}$$

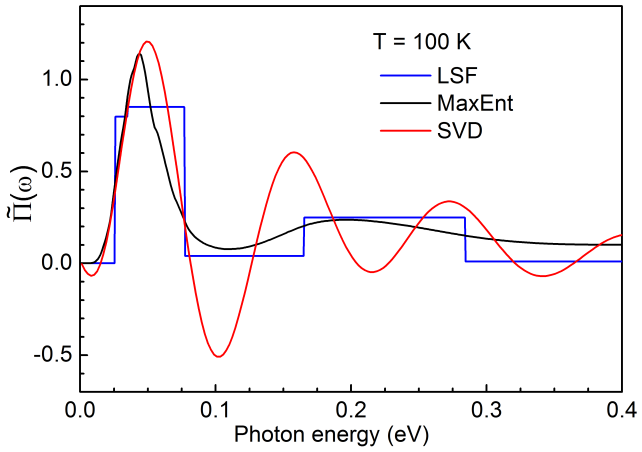

Figure 7.5: Comparison of the $\tilde{\Pi}(\omega)$ functions obtained with (blue) the LSF method used in this thesis, (black) the MaxEnt method and (red) the SVD method. For the MaxEnt method a σ = 5.0 was used, while in the SVD method about 15 of 300 svs were kept.

where,

$$S = \sum_{j=1}^{N} \left[a_j - m_j - a_j \log(\frac{a_j}{m_j}) \right] \tag{7.7}$$

which is known as the Shannon-Jaynes entropy. Here **m** is the default model vector, that represents the most probable solution without any knowledge of experimental results. The α appearing in Eq. 7.6 is a regularization parameter. One way is to adjust α such that χ^2 = N. The MaxEnt method states that the most probable solution **a** is the one that optimizes the entropy Eq. 7.7, as this will maximize the prior $p(\mathbf{a}|\alpha, \mathcal{I})$. The likelihood $p(\mathbf{t}|\mathbf{t_0}, \mathcal{I})$ ensures that this solution is within a standard deviation of the experimental data **t**. There are several possibilities for choosing the model vector **m**. If nothing is known about the solution, the best choice is a constant. Schachinger *et al.* apply this method to invert experimental data of $1/\tau(\omega)$ in both the superconducting and normal state. They start from a constant vector **m** and require that the final solution converges to this value at the highest frequency considered. One has to carefully check the dependence of the solution on the choice of this value. In a second step the resulting $\tilde{\Pi}(\omega)$ function is further optimized in a least squares fitting routine based on the Eliashberg equations.

Figure 7.5 shows a comparison of the $\tilde{\Pi}(\omega)$ function obtained at 100 K with the three different inversion methods: least squares fitting (LSF), maximum entropy (MaxEnt) and singular value decomposition inversion (SVD). We have used 100 K here because the inversion at higher temperatures is unstable with the SVD method, while at lower temperatures the superconducting gap makes the analysis more complicated. The agreement in the determination of the 50 - 60 meV peak is quite good in both position and amplitude. However, comparing the energy of the maximum of the MaxEnt and SVD spectra with the central energy of the largest block one finds $\omega_{MN} \approx 44$ meV, $\omega_{SVD} \approx 50$ meV

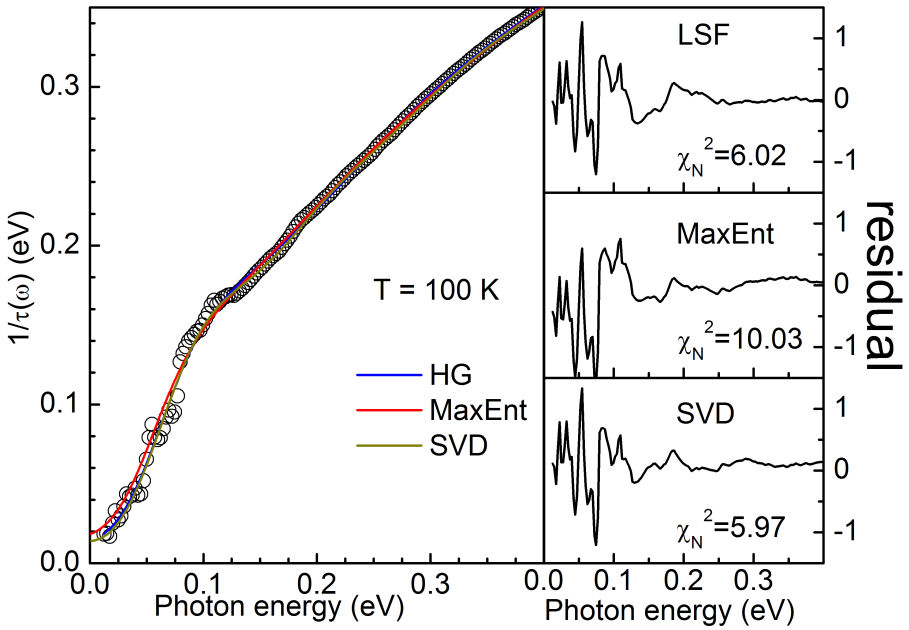

Figure 7.6: Left panel: Experimental $1/\tau(\omega)$ (open symbols) compared with calculated scattering rates from the $\tilde{\Pi}(\omega)$ functions in figure 7.5. Right panels: Residuals (see text) for the three different models. Also indicated are the χ^2 for each model normalized to N^2, where N = 156 in each case.

and $\omega_{LSF} \approx 54$ meV. This is quite a significant difference. Both the MaxEnt and LSF methods display a peak around 200 meV, but the energy seems to be slightly smaller in the MaxEnt result. The SVD method does not seem to give useful results above the first negative dip.

The scattering rates calculated with these $\tilde{\Pi}(\omega)$ functions are shown in figure 7.6. The model scattering rates are all very close to the measured scattering rate. To quantify the differences between the three curves we plot the residual defined as $r_i = (1/\tau(\omega_i) - f(\omega_i))/\sigma$ (see the Eq. 5.14) in the right panels of Fig. 7.6. A comparison of these three panels shows some remarkable things. Firstly, the LSF and SVD methods give an almost identical reproduction of the $1/\tau(\omega_i)$ data. The MaxEnt method clearly gives a slightly different result with a less good fit at low energy. We also indicated the value of χ^2 calculated for each spectrum normalized to N^2, where N = 156 is the number of experimental points and is thus the same in each case. The LSF and SVD methods are equally good while the MaxEnt is less good in a least squares sense. This does not necessarily mean that the MaxEnt $\tilde{\Pi}(\omega)$ function is not a good solution: a different criterium was used to determine $\tilde{\Pi}(\omega)$. In the language of the MaxEnt method each of these solutions is indistinguishable because they fall within a standard deviation from the best solution defined by Eq. 7.5. In such a case the MaxEnt method requires additional input (the background information $\mathfrak{I}$) from other experiments.

As explained in the previous section Hwang *et al.* find a different high temperature behavior of $\tilde{\Pi}(\omega)$ compared to our result. They find that at high temperature the low energy feature disappears

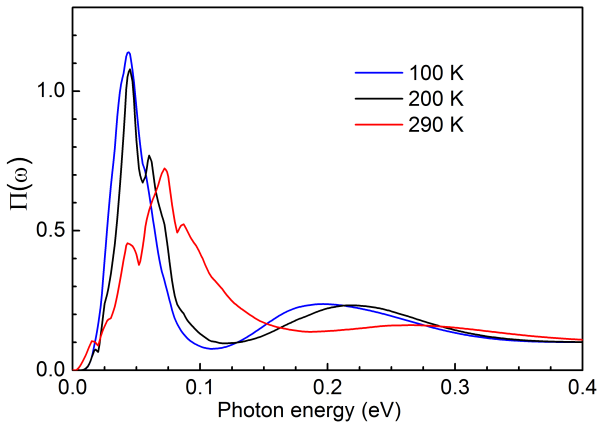

Figure 7.7: $\tilde{\Pi}(\omega)$ function obtained with the MaxEnt method for three different temperatures. There is a clear blue-shift of the low energy peak with increasing temperature. These result should be compared to Fig. 5.2f.

into the continuum. A similar, although weaker, trend is obtained by applying their analysis to our Hg1201 data. The $\tilde{\Pi}(\omega)$ functions obtained using the method of Schachinger on the Hg1201 data presented in chapter 3 are shown in figure 7.7. In this case the effect is not as strong as reported in [155], where the peak almost completely disappears (compare with the right hand panel in fig. 7.4). The room temperature result obtained in our study can be reproduced with the MaxEnt method if the default vector **m** is chosen to be equal to the solution obtained at 200 K. This highlights a difficulty in the MaxEnt method: the solution to the inversion problem somehow depends on how much is known about the solution. We stress that if one only uses the LSF method, as used in this thesis, as a criterion for determining the quality of the solution, this ambiguity is almost always resolved.

Besides a different criterion for determining the quality of a given solution, there could be two other reasons for the difference between the three methods. Firstly, we use the full Kubo formula as opposed to the memory function approximation for the scattering rate. Secondly, our method is less prone to errors made in the determination of the interband contributions. As explained in section 2.4.4 to determine $1/\tau(\omega)$ one has to make assumptions on ω_p and ε_∞. Our method is applied directly to the reflectivity and ellipsometric data where we include the interband contribution explicitly. Moreover, our method takes into account both the real *and* imaginary parts of the conductivity simultaneously.

The finite temperature extension derived by Shulga *et al.* is reasonably good at low temperature and frequency, but less good at high temperatures and frequency. In figure 7.8 we show a comparison between the scattering rates calculated from the Kubo conductivity, Eq. 5.2, and from the approximation derived by Shulga, Eq. 6.8. All spectra are calculated using the same input $\tilde{\Pi}(\omega)$ function. We note two differences between the Kubo and Shulga results: (i) the high frequency scattering rate saturates much earlier in the Shulga approximation and (ii) the structure induced by the 50 - 60 meV

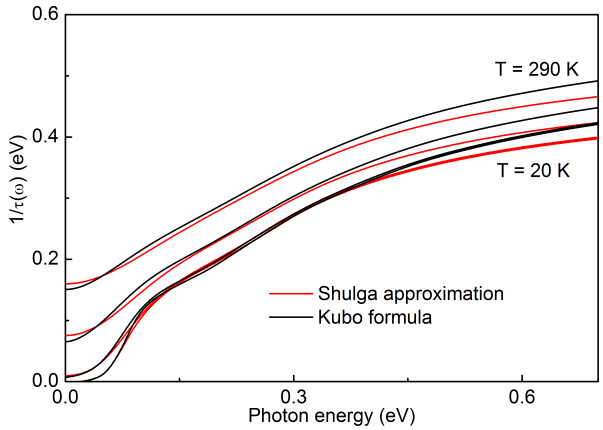

Figure 7.8: Scattering rates calculated from the Kubo formula Eq. 5.2 (black) and the approximation derived by Shulga 6.8 (red). In all cases we have used the room temperature $\tilde{\Pi}(\omega)$ function of Hg1201 presented in fig. 7.2. The displayed temperatures are 20 K, 100 K, 200 K, and 290 K from top to bottom.

peak is much weaker in the Shulga approximation and becomes even weaker at high temperature.

This comparison shows that using the Shulga approximation at room temperature is clearly a bad idea. Schachinger *et al.* use this approximation together with the MaxEnt method to obtain a $\tilde{\Pi}(\omega)$ function. Schachinger *et al.* then parameterize the $I^2\chi$ using a few parameters, and optimize these parameters using a least squares fitting routine. In this last step they use the Eliashberg equations together with the full Kubo expression for the conductivity. It is clear that part of the difference between our results could be explained if only the Shulga result was used. At 100 K and 200 K their method gives the same result as our method: a nearly temperature independent $\tilde{\Pi}(\omega)$ function with a peak at 50 - 60 meV and a continuum. The χ^2 obtained at these two temperatures is nearly identical to the ones obtained with our method. At room temperature their method shows a small but significant shift of the 50 - 60 meV peak that is not observed with our method. It is possible that the parametrization of the room temperature $\tilde{\Pi}(\omega)$ function obtained with the MaxEnt method is not flexible enough to correct for the error introduced by using the Shulga approximation.

We conclude from the above comparison that results obtained from our method and the MaxEnt method are indeed very close. It appears that at temperatures above 200 K the combination of MaxEnt and the full Eliashberg analysis are a less accurate than our method. This statement is based on the fact that our method gives a better fit to the original reflectivity data or the scattering rate. The resulting difference between our $\tilde{\Pi}(\omega)$ function and the one obtained by Schachinger *et al.* is crucial: based on the results obtained for optimally doped Bi2212 in Ref. [155] (see fig. 7.4), one would be tempted to conclude that the optical spectra are well described by a model in which the electrons interact with a spin fluctuation continuum. This continuum is broad and featureless at room temperature, while it develops a resonant structure at lower temperatures due to the opening of a (pseudo-) gap. Our

analysis also indicates the coupling to a broad spin fluctuation spectrum, but it clearly shows that an important part of $\tilde{\Pi}(\omega)$ cannot be attributed to spin fluctuations, and has clear characteristics of the electron-phonon interaction.

7.5 Discussion

From the results presented in this thesis we can conclude that the optical properties of cuprates can be well described within a generalized Eliashberg formalism. The frequency and temperature dependence of the conductivity of optimally and overdoped materials can be almost completely characterized by a single $\tilde{\Pi}(\omega)$ function. This gives strong evidence that in this part of the phase diagram the normal state is a Fermi liquid. The peculiar properties or "strangeness" of the normal state arises from a strong scattering of the electrons from phonon and electronic degrees of freedom, that decoheres the electron motion. With increasing doping this scattering mechanism weakens and the electrons behave more coherently, and hence more Fermi liquid like. This behavior is also seen in ARPES experiments where strongly doped samples show sharp, coherent Fermi surfaces [173]. With decreasing doping the Fermi surface breaks up into Fermi arcs below optimal doping [95, 174]. Recently, the observation of quantum oscillations in underdoped samples was taken as evidence that the Fermi arcs seen in ARPES are actually small Fermi pockets [175]. This suggests that even for underdoped samples a Fermi liquid state may still be a valid starting point for a perturbation expansion. The $\tilde{\Pi}(\omega)$ functions in the left hand panels of figure 7.2 suggest that with decreasing doping the conventional Eliashberg picture is less good in capturing all the details of the optical spectra. This indicates that some modification of the theory has to be made. Since the Eliashberg formalism is essentially a perturbation expansion, the validity of the formalism is governed by a "small parameter". This parameter is usually expressed as an effective coupling constant. A measure for this coupling constant is given by, $\lambda = 2\int_0^\infty \tilde{\Pi}(\omega)/\omega d\omega$ (see section 5.4). The coupling strength, shown in Fig. 7.9, shows a strong and systematic increase of λ for decreasing hole concentration. We note that the coupling constant increases toward lower temperatures, and that the temperature dependence is stronger at lower doping. As can be see from Fig. 7.2, this systematic temperature dependence of λ is a direct consequence of a growth of weight for energies below the 50-60 meV feature. As discussed above this temperature dependence reflects the electronic nature of $\tilde{\Pi}(\omega)$ Several theoretical proposals exist that would give rise to a boson spectrum deriving from electronic degrees of freedom [39, 112, 113, 116]. The coupling strengths reported in figure 7.9 are extremely large compared to those observed in normal metals. The trend of increasing coupling strength with decreasing doping is consistent with the observation of a increasingly incoherent Fermi surface in ARPES. An interesting question that is not completely answered by our study is whether this coupling strength diverges at lower dopings, as expected in a picture where the undoped

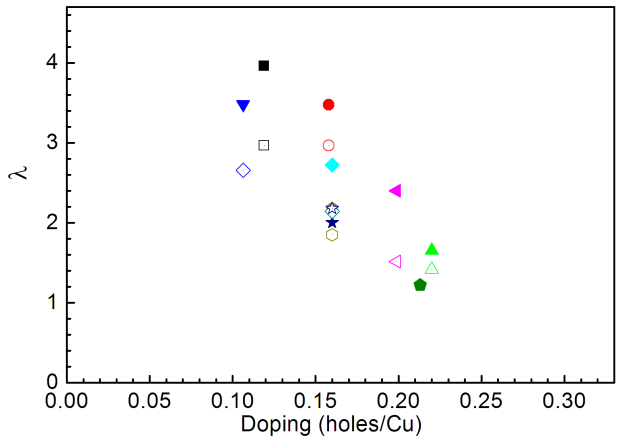

Figure 7.9: Coupling strength as a function of carrier concentration. Open symbols: 290 K, closed symbols: 100K. The symbol colors and types refer to the same samples as in Fig. 7.10. The observed trend of decreasing λ with doping is consistent with other experiments (e.g Ref's. [155, 118, 95])

state is a Mott insulator. In this picture the undoped parent compound is a strongly correlated antiferromagnetic insulator. Since the electrons then become completely localized they can be described as having infinitely large effective mass. Doping such a state will make the electrons more and more mobile leading to a finite mass that decreases with increasing doping [17]. We have found one sample where the Eliashberg formalism clearly can not describe the optical data (the UD0 Bi2201 sample) but in this sample disorder may play a much more important role than the approach to the Mott insulator.

The most prominent feature, present in all spectra reproduced in Fig. 7.2, is a peak corresponding to an average frequency of 50 -60 meV. Perhaps the most striking aspect of this peak is the fact that its energy, displayed in Fig. 7.10, is practically independent of temperature (up to room temperature) and sample composition. Moreover, the intensity and width are essentially temperature independent. While our results confirm by and large the observations of Hwang *et al.* in the pseudo-gap phase [155, 156], the persistence of the 50-60 meV peak to room temperature has not been reported before.

It is difficult to determine the origin of the structures in $\tilde{\Pi}(\omega)$ due to the closeness of several energy scales. The 50 - 60 meV peak has been previously ascribed to the spin resonance seen by neutron scattering. The fact that in our analysis it persists to room temperature almost unchanged seems to exclude an interpretation solely in terms of spin-fluctuations. The coupling to oxygen vibrations falls in this range but first principles calculations put an upper limit of $\lambda \approx 0.6$ on the *total* (*i.e., integrated over all vibrational modes*) electron-phonon coupling constant. This is too small to explain the coupling seen below 100 meV except perhaps for the most overdoped Bi2201 and Bi2212 samples. It is clear that the continuum extending up to 300 meV has to be of electronic nature. Indeed Maier, Poilblanc and Scalapino obtained from numerical studies of the Hubbard model [176] a *d*-wave projected susceptibility which has structure around the energy scale $2J \approx 280$ meV, close to the structure in $\tilde{\Pi}(\omega)$ seen

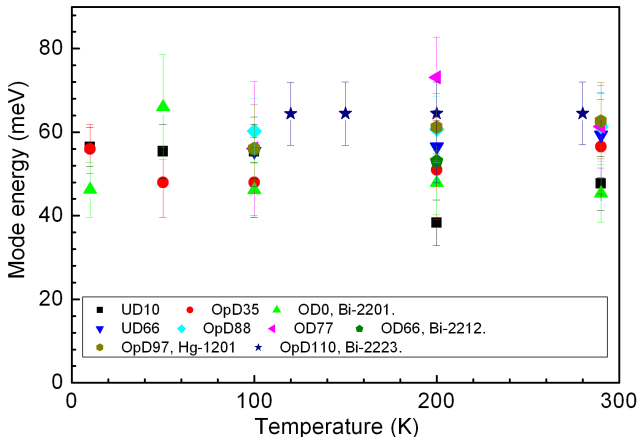

Figure 7.10: Frequency of the peak maximum in the electron-boson coupling functions of Fig. 7.2 as a function of temperature. The mean frequency for all temperatures and samples is 56 $\pm$ 8 meV

in the optimally doped samples. This continuum also gives a contribution to $\tilde{\Pi}(\omega)$ in the range below 100 meV. With decreasing doping the continuum contracts adding more amplitude in the range below 100 meV. This observation together with the observation that the strength of the 50 - 60 meV peak increases with decreasing doping suggests an interplay between phonon and electronic degrees of freedom [141, 142, 177]. This interpretation naturally explains the doping and temperature dependence of the 50 - 60 meV peak in all samples.

Maier *et al.* also showed that the 'anomalous' self-energy associated with the pairing has a small but finite contribution extending to an energy as high as U, demonstrating that the pairing-interaction is, in part, effectively non-retarded. The theoretical approaches to the pairing mechanism are divided in two main schools: One which concentrates on a pairing-mechanism entirely due to this 'non-retarded' interaction [36] or so-called Mottness [178], and the other which attributes it to the retarded glue-function [39, 112, 113, 153]. Indeed our experiments indicate this mixing to take place as evidenced by the anomalous spectral weight transfer at the critical temperature discussed in the previous chapter.

The function $\tilde{\Pi}(\omega)$ obtained in our analysis represents the total spectral density of bosons in all angular momentum channels. The properties of the superconducting state in the cuprates are mainly determined by the projection of $\tilde{\Pi}(\omega)$ on the d-wave channel as evidenced by the symmetry of the order parameter. We can obtain an upper limit on the critical temperature by assuming that the entire $\tilde{\Pi}(\omega)$ has a projection on the d-wave channel and assuming that the pseudo-potential $\mu^* = 0$. Obviously, the actual critical temperatures will be lower as a result of the pair-breaking contributions in $\tilde{\Pi}(\omega)$. The critical temperature can be calculated straightforwardly from the Eliashberg equations [179] when $\tilde{\Pi}(\omega)$ is known. As shown in Fig. 7.11, the T_c's are in the 150-300 K range for all samples studied here, and they correlate with the experimentally observed doping trends of T_c for the single-layer and

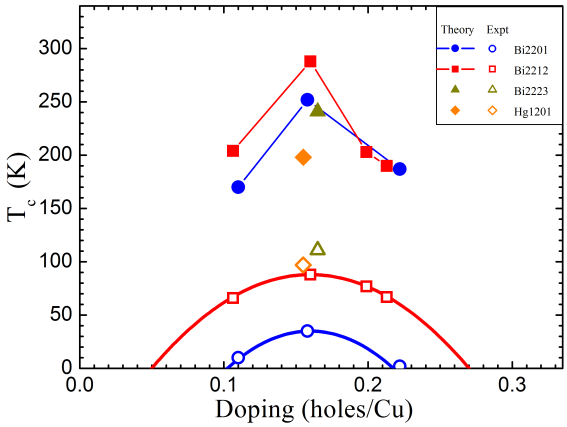

Figure 7.11: Experimental critical temperatures and upper limit on T_c calculated from Eliashberg theory using the $\tilde{\Pi}(\omega)$ functions of Fig. 7.2 at 290 Kelvin as input.

bilayer high-T_c materials. The low value of T_c in single layer Bi2201 correlates with a relatively high amplitude of $\tilde{\Pi}(\omega)$ below the 50-60 meV peak, and a very low amplitude or absence of the 0.25 eV peak. In contrast, the three samples with the highest critical temperature, Bi2212 OpD88, Bi-2223 and Hg-1201, show the most pronounced weight at $\sim$ 0.25 eV. We note that in order to get a substantial value for T_c in the overdoped samples the high energy part of $\tilde{\Pi}(\omega)$ is necessary.

7.6 Conclusion

I have presented an analysis of the optical properties of several hole doped cuprates using a generalized Eliashberg formalism. I have shown that this formalism can be consistently applied for optimally and overdoped samples. The formalism needs to be modified in the underdoped region of the phase diagram, where one should probably include the presence of a pseudogap or consider the role played by vertex corrections due to the extremely large coupling strength. Although such modifications will definitely influence the resulting $\tilde{\Pi}(\omega)$ functions I believe the main result will be to reduce the temperature dependence of the $\tilde{\Pi}(\omega)$ functions. near optimal doping and above the $\tilde{\Pi}(\omega)$ function consists of two features: a peak at 50 - 60 meV and a continuum. The 50 -60 meV peak likely arises in part from phonon degrees of freedom. The continuum is electronic in origin, and possibly related to diffusive spin modes. With decreasing doping the continuum contracts and the intensity in the 50 - 60 meV peak increases. This suggests an interplay between phonon and magnetic degrees of freedom, in support of several recent theoretical and experimental observations [141, 142]. Under the assumption that the entire $\tilde{\Pi}(\omega)$ function projects favorably on the $d-wave$ channel, we find that it can easily explain the high critical temperature in these materials. Taken together our observations suggest that superconductivity in the cuprates arises through the exchange of force mediating bosons.

Bibliography

[1] Bardeen, J., Cooper, L. N., and Schrieffer, J. R. *Phys. Rev.* **106**(1), 162–164 Apr (1957).

[2] Bardeen, J., Cooper, L. N., and Schrieffer, J. R. *Phys. Rev.* **108**(5), 1175–1204 Dec (1957).

[3] Migdal, A. *Sov. Phys. JETP* **7**, 996 (1957).

[4] Eliashberg, G. M. *Sov. Phys. JETP* **11**, 696 (1960).

[5] Nambu, Y. *Phys. Rev.* **117**(3), 648–663 Feb (1960).

[6] Giaever, I. *Phys. Rev. Lett.* **5**(4), 147–148 Aug (1960).

[7] Giaever, I., Hart, H. R., and Megerle, K. *Phys. Rev.* **126**(3), 941–948 May (1962).

[8] McMillan, W. L. and Rowell, J. M. *Phys. Rev. Lett.* **14**(4), 108–112 Jan (1965).

[9] Scalapino, D. J., Schrieffer, J. R., and Wilkins, J. W. *Phys. Rev.* **148**(1), 263–279 Aug (1966).

[10] Mazin, I. I. *cond-mat/0708.1947* .

[11] Cohen, M. L. and Anderson, P. W. In *Superconductivity in d- and f-band Metals,* Douglass, D. H., editor, 17 (AIP, New York, 1972).

[12] Kirzhnits, D. A. *Sov. Phys.-Usp* **19**, 530 (1976).

[13] Bednorz, J. G. and Müller, K. A. *Z. Phys. B Cond. Mat* **64**, 189 (1986).

[14] Wu, M. K., Ashburn, J. R., Torng, C. J., Hor, P. H., Meng, R. L., Gao, L., Huang, Z. J., Wang, Y. Q., and Chu, C. W. *Phys. Rev. Lett.* **58**(9), 908–910 Mar (1987).

[15] Gao, L., Xue, Y. Y., Chen, F., Xiong, Q., Meng, R. L., Ramirez, D., Chu, C. W., Eggert, J. H., and Mao, H. K. *Phys. Rev. B* **50**(6), 4260–4263 Aug (1994).

[16] Pickett, W. E. *Rev. Mod. Phys.* **61**(2), 433–512 Apr (1989).

[17] Imada, M., Fujimori, A., and Tokura, Y. *Rev. Mod. Phys.* **70**(4), 1039–1263 Oct (1998).

[18] Grueninger, M. *Of spin and charge in the cuprates.* PhD thesis, University of Groningen, (1999).

[19] Maksimov, E. G. *Physics-Uspekhi* **43**(10), 965–990 (2000).

[20] Damascelli, A., Hussain, Z., and Shen, Z. X. *Rev. Mod. Phys.* **75**(2), 473–541 Apr (2003).

[21] Marsiglio, F. and Carbotte, J. In *The Physics of Conventional and Unconventional Superconductors,* Bennemann, K. and Ketterson, J., editors, 233–345. Springer-Verlag, (2003).

[22] Basov, D. N. and Timusk, T. *Rev. Mod. Phys.* **77**(2), 721 (2005).

[23] Lee, P. A., Nagaosa, N., and Wen, X. G. *Rev. Mod. Phys.* **78**(1), 17 (2006).

[24] Zhou, X. J., Cuk, T., Devereaux, T., Nagaosa, N., and Shen, Z. X. *Handbook of High-Temperature Superconductivity: Theory and Experiment, edited by J. R. Schrieffer, (Springer)* (2007).

[25] Fischer, O., Kugler, M., Maggio-Aprile, I., Berthod, C., and Renner, C. *Rev. Mod. Phys.* **79**(1), 353 (2007).

[26] Zaanen, J., Sawatzky, G. A., and Allen, J. W. *Phys. Rev. Lett.* **55**(4), 418–421 Jul (1985).

[27] Anderson, P. W. *Science* **235**(4793), 1196–1198 (1987).

[28] Li, Y., Balédent, V., Barisic, N., Cho, Y., Fauqué, B., Sidis, Y., Yu, G., Zhao, X., Bourges, P., and Greven, M. *Nature* **455** (2008).

[29] Varma, C. M. *Phys. Rev. B* **55**(21), 14554–14580 Jun (1997).

[30] Varma, C. M. *Phys. Rev. B* **73**(15), 155113 (2006).

[31] Weber, C., Läuchli, A., Mila, F., and Giamarchi, T. *condmat/0803.3983* .

[32] Hufner, S., Hossain, M. A., Damascelli, A., and Sawatzky, G. *Rep. Prog. Phys.* **71**, 062501 (2008).

[33] V. J. Emery, S. V. K. *Nature* **374**, 434 (1995).

[34] Corson, J., Mallozzi, R., Orenstein, J., Eckstein, J. N., and Bozovic, I. *Nature* **398**, 221 (1999).

[35] Anderson, P. W., Lee, P. A., Randeria, M., Rice, T. M., Trivedi, N., and Zhang, F. C. *J. Phys: Cond. Mat.* **16**(24), R755–R769 (2004).

[36] Anderson, P. W. *Science* **316**(5832), 1705–1707 (2007).

[37] Eichenberger, D. and Baeriswyl, D. *Phys. Rev. B* **76**(18), 180504 (2007).

[38] Mahan, G. Physics of solids and liquids (Plenum Press, New york and London, 1981).

[39] Scalapino, D. J., Loh, E., and Hirsch, J. E. *Phys. Rev. B* **34**(11), 8190–8192 Dec (1986).

[40] Tsuei, C. C., Kirtley, J. R., Chi, C. C., Yu-Jahnes, L. S., Gupta, A., Shaw, T., Sun, J. Z., and Ketchen, M. B. *Phys. Rev. Lett.* **73**(4), 593–596 Jul (1994).

[41] Wooten, F. *optical Properties of Solids*. Academic Press, New-York, (1972).

[42] Dressel, M. and Grunner, G. *Electrodynamics of Solids: Optical Properties of Electrons in Matter*. Cambridge University Press, Cambridge, (2002).

[43] van Heumen, E. and van der Marel, D. In *LECTURES ON THE PHYSICS OF STRONGLY CORRELATED SYSTEMS XI: Eleventh Training Course in the Physics of Strongly Correlated Systems,* Mancini, F. and Avella, A., editors, AIP Conference Proceedings Volume 918, Materials Physics and Applications, 203. AIP, (2007).

[44] van Heumen, E. and van der Marel, D. *http://arxiv.org/abs/0807.3261* (2007).

[45] Molegraaf, H. J. A., Presura, C., van der Marel, D., Kes, P. H., and Li, M. *Science* **295**(5563), 2239–2241 (2002).

[46] Carbone, F., Kuzmenko, A. B., Molegraaf, H. J. A., van Heumen, E., Lukovac, V., Marsiglio, F., van der Marel, D., Haule, K., Kotliar, G., Berger, H., Courjault, S., Kes, P. H., and Li, M. *Phys. Rev. B* **74**(6), 064510 (2006).

[47] Carbone, F., Kuzmenko, A. B., Molegraaf, H. J. A., van Heumen, E., Giannini, E., and van der Marel, D. *Phys. Rev. B* **74**(2), 024502 (2006).

[48] Uemura, Y. J., Luke, G. M., Sternlieb, B. J., Brewer, J. H., Carolan, J. F., Hardy, W. N., Kadono, R., Kempton, J. R., Kiefl, R. F., Kreitzman, S. R., Mulhern, P., Riseman, T. M., Williams, D. L., Yang, B. X., Uchida, S., Takagi, H., Gopalakrishnan, J., Sleight, A. W., Subramanian, M. A., Chien, C. L., Cieplak, M. Z., Xiao, G., Lee, V. Y., Statt, B. W., Stronach, C. E., Kossler, W. J., and Yu, X. H. *Phys. Rev. Lett.* **62**(19), 2317–2320 May (1989).

[49] van der Marel, D., Somal, H. S., Feenstra, B. J., van der Eb, J. E., Schuetzmann, J., and Kim, J. H. In *Proc. of the 10th Anniv. HTS Workshop on Physics, Materials and Applications.,* Batlogg, B., Chu, C., Chu, W., Gubser, D., and Muller, K., editors, 357 (World Scientific, Singapore, 1996).

[50] van Heumen, E., Lortz, R., Kuzmenko, A. B., Carbone, F., van der Marel, D., Zhao, X., Yu, G., Cho, Y., Barisic, N., Greven, M., and Dordevic, C. H. S. *Phys. Rev. B* **75**(5), 054522 (2007).

[51] Smith, D. Y. and Shiles, E. *Phys. Rev. B* **17**(12), 4689–4694 Jun (1978).

[52] Tinkham, M. and Ferrell, R. A. *Phys. Rev. Lett.* **2**(8), 331–333 Apr (1959).

[53] Kubo, R. *J. Phys. Soc. Jpn.* **12**, 570 (1957).

[54] van der Marel, D., Molegraaf, H. J. A., Pressura, C., and Santosa, I. In *Concepts in electron correlation,* Hewson, A. and Zlatic, V., editors, 7. Kluwer, (2003).

[55] Santander-Syro, A. F., Lobo, R. P. S. M., Bontemps, N., Konstantinovic, Z., Li, Z. Z., and Raffy, H. *Europhys. Lett.* **62**(4), 568–574 (2003).

[56] Kuzmenko, A. B., Molegraaf, H. J. A., Carbone, F., and van der Marel, D. *Phys. Rev. B* **72**(14), 144503 (2005).

[57] Hirsch, J. E. *Physica C* **199**(3-4), 305 (1992).

[58] Hirsch, J. E. and Marsiglio, F. *Physica C* **331**, 150 (2000).

[59] Hirsch, J. E. and Marsiglio, F. *Phys. Rev. B* **62**(22), 15131–15150 Dec (2000).

[60] Norman, M. R. and Pépin, C. *Phys. Rev. B* **66**(10), 100506 Sep (2002).

[61] Eckl, T., Hanke, W., and Arrigoni, E. *Phys. Rev. B* **68**(1), 014505 Jul (2003).

[62] Wróbel, P., Eder, R., and Fulde, P. *J. Phys: Cond. Mat.* **15**(38), 6599–6616 (2003).

[63] Knigavko, A., Carbotte, J. P., and Marsiglio, F. *Phys. Rev. B* **70**(22), 224501 (2004).

[64] Maier, T. A., Jarrell, M., Macridin, A., and Slezak, C. *Phys. Rev. Lett.* **92**(2), 027005 Jan (2004).

[65] Toschi, A., Capone, M., Ortolani, M., Calvani, P., Lupi, S., and Castellani, C. *Phys. Rev. Lett.* **95**(9), 097002 (2005).

[66] Marsiglio, F. *Phys. Rev. B* **73**(6), 064507 (2006).

[67] Marsiglio, F., Carbone, F., Kuzmenko, A. B., and van der Marel, D. *Phys. Rev. B* **74**(17), 174516 (2006).

[68] Benfatto, L., Carbotte, J. P., and Marsiglio, F. *Phys. Rev. B* **74**(15), 155115 (2006).

[69] Haule, K. and Kotliar, G. *Europhys. Lett.* **77**(2), 27007 (5pp) (2007).

[70] Norman, M. R., Chubukov, A. V., van Heumen, E., Kuzmenko, A. B., and van der Marel, D. *Phys. Rev. B* **76**(22), 220509 (2007).

[71] Marsiglio, F., van Heumen, E., and Kuzmenko, A. B. *Phys. Rev. B* **77**(14), 144510 (2008).

[72] Allen, J. W. and Mikkelsen, J. C. *Phys. Rev. B* **15**(6), 2952–2960 Mar (1977).

[73] El Azrak, A., Nahoum, R., Bontemps, N., Guilloux-Viry, M., Thivet, C., Perrin, A., Labdi, S., Li, Z. Z., and Raffy, H. *Phys. Rev. B* **49**(14), 9846–9856 Apr (1994).

[74] van der Marel, D., Molegraaf, H. J. A., Zaanen, J., Nussinov, Z., Carbone, F., Damascelli, A., Eisaki, H., Greven, M., Kes, P. H., and Li, M. *Nature* **425**, 271–274 (2003).

[75] Barisic, N., Li, Y., Zhao, X., Cho, Y.-C., Chabot-Couture, G., Yu, G., and Greven, M. *Phys. Rev. B* **78**(5), 054518 (2008).

[76] Zhao, X., Yu, G., Cho, Y., Chabot-Couture, G., Barisic, N., Bourges, P., Kaneko, N., Li, Y., Lu, L., Motoyama, E. M., Vajk, O. P., and Greven, M. *Adv. Mater.* **18**, 3243 (2006).

[77] Lu, L., Chabot-Couture, G., Zhao, X., Hancock, J. N., Kaneko, N., Vajk, O. P., Yu, G., Grenier, S., Kim, Y. J., Casa, D., Gog, T., and Greven, M. *Phys. Rev. Lett.* **95**(21), 217003 (2005).

[78] Lee, W. S., Yoshida, T., Meevasana, W., Shen, K. M., Lu, D. H., Yang, W. L., Zhou, X. J., Zhao, X., Yu, G., Cho, Y., Greven, M., Hussain, Z., and Shen, Z. X. *arXiv:cond-mat/0606347* (2006).

[79] Pimenov, A., Pronin, A. V., Loidl, A., Tsukada, A., and Naito, M. *Phys. Rev. B* **66**(21), 212508 Dec (2002).

[80] Kuzmenko, A. B. *Rev. Sci. Inst.* **76**(8), 083108 (2005).

[81] Timusk, T. *Solid State Commun.* **127**, 337 (2003).

[82] Wang, Y., Plackowski, A. T., and Junod, A. *Physica C* **355**, 179 (2001).

[83] Billon, B., Charalambous, M., Riou, O., Chaussy, J., and Pelloquin, D. *Phys. Rev. B* **56**(17), 10824–10827 Nov (1997).

[84] Hwang, J., Timusk, T., and Gu, G. D. *Nature* **427**, 714 (2004).

[85] Homes, C. C., Dordevic, S. V., Strongin, M., Bonn, D. A., Liang, R., Hardy, W. N., Komiya, S., Ando, Y., Yu, G., Kaneko, N., Zhao, X., Greven, M., Basov, D. N., and Timusk, T. *Nature* **430**(19), 539–541 July (2004).

[86] Marsiglio, F., Carbone, F., Kuzmenko, A. B., and van der Marel, D. *Phys. Rev. B* **74**(17), 174516 (2006).

[87] Kuzmenko, A. B., van der Marel, D., Carbone, F., and Marsiglio, F. *New J. Phys.* **9**(7), 229 (2007).

[88] Meingast, C., Pasler, V., Nagel, P., Rykov, A., Tajima, S., and Olsson, P. *Phys. Rev. Lett.* **86**(8), 1606–1609 Feb (2001).

[89] T. Schneider, J. S. Imperial College Press, (2000).

[90] Junod, A., Roulin, M., Genoud, J. Y., Revaz, B., Erb, A., and Walker, E. *Physica C* **275**, 245 (1997).

[91] A. Junod, K.Q. Wang, G. T. and Muller, J. *Physica B* **194-196**, 1497 (1994).

[92] Lortz, R., Meingast, C., Rykov, A. I., and Tajima, S. *Phys. Rev. Lett.* **91**(20), 207001 Nov (2003).

[93] van der Marel, D., Leggett, A. J., Loram, J. W., and Kirtley, J. R. *Phys. Rev. B* **66**(14), 140501 Oct (2002).

[94] Yang, K., Xie, B. P., Shen, D. W., Zhao, J. F., Ou, H. W., Wei, J., Wang, S., Wang, Y. H., Lu, D. H., He, R. H., Arita, M., Qiao, S., Ino, A., Namatame, H., Taniguchi, M., Xu, F. Q., Kaneko, N., Eisaki, H., and Feng, D. L. *Phys. Rev. B* **73**(14), 144507 (2006).

[95] Meevasana, W., Ingle, N. J. C., Lu, D. H., Shi, J. R., Baumberger, F., Shen, K. M., Lee, W. S., Cuk, T., Eisaki, H., Devereaux, T. P., Nagaosa, N., Zaanen, J., and Shen, Z.-X. *Phys. Rev. Lett.* **96**(15), 157003 (2006).

[96] Hashimoto, M., Yoshida, T., Yagi, H., Takizawa, M., Fujimori, A., Kubota, M., Ono, K., Tanaka, K., Lu, D. H., Shen, Z. X., Ono, S., and Ando, Y. *Phys. Rev. B* **77**(9), 094516 (2008).

[97] Graf, J., d'Astuto, M., Jozwiak, C., Garcia, D. R., Saini, N. L., Krisch, M., Ikeuchi, K., Baron, A. Q. R., Eisaki, H., and Lanzara, A. *Phys. Rev. Lett.* **100**(22), 227002 (2008).

[98] Khasanov, R., Kondo, T., Strassle, S., Heron, D. O. G., Kaminski, A., Keller, H., Lee, S. L., and Takeuchi, T. *condmat/0811.2077* (2008).

[99] Tsvetkov, A. A., Schützmann, J., Gorina, J. I., Kaljushnaia, G. A., and van der Marel, D. *Phys. Rev. B* **55**(21), 14152–14155 Jun (1997).

[100] Tsvetkov, A. A., Dulić, D., van der Marel, D., Damascelli, A., Kaljushnaia, G. A., Gorina, J. I., Senturina, N. N., Kolesnikov, N. N., Ren, Z. F., Wang, J. H., Menovsky, A. A., and Palstra, T. T. M. *Phys. Rev. B* **60**(18), 13196–13205 Nov (1999).

[101] Ando, Y., Hanaki, Y., Ono, S., Murayama, T., Segawa, K., Miyamoto, N., and Komiya, S. *Phys. Rev. B* **61**(22), R14956–R14959 Jun (2000).

[102] Ono, S. and Ando, Y. *Phys. Rev. B* **67**(10), 104512 Mar (2003).

[103] Lee, K., Heeger, A. J., and Cao, Y. *Phys. Rev. B* **48**(20), 14884–14891 Nov (1993).

[104] Kim, J. H., Feenstra, B. J., Somal, H. S., van der Marel, D., Lee, W. Y., Gerrits, A. M., and Wittlin, A. *Phys. Rev. B* **49**(18), 13065–13069 May (1994).

[105] Uchida, S., Ido, T., Takagi, H., Arima, T., Tokura, Y., and Tajima, S. *Phys. Rev. B* **43**(10), 7942–7954 Apr (1991).

[106] Lee, Y. S., Segawa, K., Li, Z. Q., Padilla, W. J., Dumm, M., Dordevic, S. V., Homes, C. C., Ando, Y., and Basov, D. N. *Phys. Rev. B* **72**(5), 054529 (2005).

[107] Allen, P. B. *Phys. Rev. B* **3**(2), 305–320 Jan (1971).

[108] Farnworth, B. and Timusk, T. *Phys. Rev. B* **14**(11), 5119–5120 Dec (1976).

[109] Holstein, T. *Ann. Phys.* **29**(3), 410–535 (1964).

[110] Allen, P. B. *arXiv: cond-mat/0407777* (2004).

[111] Dordevic, S. V., Homes, C. C., Tu, J. J., Valla, T., Strongin, M., Johnson, P. D., Gu, G. D., and Basov, D. N. *Phys. Rev. B* **71**(10), 104529 (2005).

[112] Varma, C. M., Littlewood, P. B., Schmitt-Rink, S., Abrahams, E., and Ruckenstein, A. E. *Phys. Rev. Lett.* **63**(18), 1996–1999 Oct (1989).

[113] Millis, A. J., Monien, H., and Pines, D. *Phys. Rev. B* **42**(1), 167–178 Jul (1990).

[114] Aji, V. and Varma, C. M. *Phys. Rev. Lett.* **99**(6), 067003 (2007).

[115] van der Marel, D., Carbone, F., Kuzmenko, A. B., , and Giannini, E. *Ann. Phys.* **321**(7), 1716–1729 (2006).

[116] Chubukov, A. V. *Europhys. Lett.* **44**(5), 655–660 dec (1998).

[117] Hwang, J., Timusk, T., Puchkov, A. V., Wang, N. L., Gu, G. D., Homes, C. C., Tu, J. J., and Eisaki, H. *Phys. Rev. B* **69**(9), 094520 Mar (2004).

[118] Johnson, P. D., Valla, T., Fedorov, A. V., Yusof, Z., Wells, B. O., Li, Q., Moodenbaugh, A. R., Gu, G. D., Koshizuka, N., Kendziora, C., Jian, S., and Hinks, D. G. *Phys. Rev. Lett.* **87**(17), 177007 Oct (2001).

[119] Lanzara, A., Bogdanov, P. V., Zhou, X. J., Kellar, S. A., Feng, D. L., Lu, E. D., Yoshida, T., Eisaki, H., Fujimori, A., Kishio, K., Shimoyama, J. I., Noda, T., Uchida, S., Hussain, Z., and Shen, Z. X. *Nature* **412**, 510 (2001).

[120] Cuk, T., Baumberger, F., Lu, D. H., Ingle, N., Zhou, X. J., Eisaki, H., Kaneko, N., Hussain, Z., Devereaux, T. P., Nagaosa, N., and Shen, Z.-X. *Phys. Rev. Lett.* **93**(11), 117003 Sep (2004).

[121] Cuk, T., Lu, D. H., Zhou, X. J., Shen, Z. X., Devereaux, T. P., and Nagaosa, N. *Phys. Stat. Sol. (b)* **242**(1), 11 (2004).

[122] Savrasov, S. Y. and Andersen, O. K. *Phys. Rev. Lett.* **77**(21), 4430–4433 Nov (1996).

[123] Jepsen, O., Andersen, O. K., Dasgupta, I., and Savrasov, S. *J. Phys. Chem. Solids* **59**, 1718 (1998).

[124] Fink, J., Koitzsch, A., Geck, J., Zabolotnyy, V., Knupfer, M., Buchner, B., Chubukov, A., and Berger, H. *Phys. Rev. B* **74**(16), 165102 (2006).

[125] Meevasana, W., Devereaux, T. P., Nagaosa, N., Shen, Z.-X., and Zaanen, J. *Phys. Rev. B* **74**(17), 174524 (2006).

[126] Meevasana, W., Baumberger, F., Tanaka, K., Schmitt, F., Dunkel, W. R., Lu, D. H., Mo, S. K., Eisaki, H., and Shen, Z. X. *Phys. Rev. B* **77**(10), 104506 (2008).

[127] Bogdanov, P. V., Lanzara, A., Kellar, S. A., Zhou, X. J., Lu, E. D., Zheng, W. J., Gu, G., Shimoyama, J. I., Kishio, K., Ikeda, H., Yoshizaki, R., Hussain, Z., and Shen, Z. X. *Phys. Rev. Lett.* **85**(12), 2581–2584 Sep (2000).

[128] Kaminski, A., Randeria, M., Campuzano, J. C., Norman, M. R., Fretwell, H., Mesot, J., Sato, T., Takahashi, T., and Kadowaki, K. *Phys. Rev. Lett.* **86**(6), 1070–1073 Feb (2001).

[129] Valla, T., Kidd, T. E., Yin, W.-G., Gu, G. D., Johnson, P. D., Pan, Z.-H., and Fedorov, A. V. *Phys. Rev. Lett.* **98**(16), 167003 (2007).

[130] Inosov, D. S., Fink, J., Kordyuk, A. A., Borisenko, S. V., Zabolotnyy, V. B., Schuster, R., Knupfer, M., Buchner, B., Follath, R., Durr, H. A., Eberhardt, W., Hinkov, V., Keimer, B., and Berger, H. *Phys. Rev. Lett.* **99**(23), 237002 (2007).

[131] Gromko, A. D., Fedorov, A. V., Chuang, Y.-D., Koralek, J. D., Aiura, Y., Yamaguchi, Y., Oka, K., Ando, Y., and Dessau, D. S. *Phys. Rev. B* **68**(17), 174520 Nov (2003).

[132] Borisenko, S. V., Kordyuk, A. A., Kim, T. K., Koitzsch, A., Knupfer, M., Fink, J., Golden, M. S., Eschrig, M., Berger, H., and Follath, R. *Phys. Rev. Lett.* **90**(20), 207001 May (2003).

[133] Zhou, X. J., Shi, J., Yoshida, T., Cuk, T., Yang, W. L., Brouet, V., Nakamura, J., Mannella, N., Komiya, S., Ando, Y., Zhou, F., Ti, W. X., Xiong, J. W., Zhao, Z. X., Sasagawa, T., Kakeshita, T., Eisaki, H., Uchida, S., Fujimori, A., Zhang, Z., Plummer, E. W., Laughlin, R. B., Hussain, Z., and Shen, Z.-X. *Phys. Rev. Lett.* **95**(11), 117001 (2005).

[134] Stojkovic, B. P. and Pines, D. *Phys. Rev. B* **55**(13), 8576–8595 Apr (1997).

[135] Kaminski, A., Fretwell, H. M., Norman, M. R., Randeria, M., Rosenkranz, S., Chatterjee, U., Campuzano, J. C., Mesot, J., Sato, T., Takahashi, T., Terashima, T., Takano, M., Kadowaki, K., Li, Z. Z., and Raffy, H. *Phys. Rev. B* **71**(1), 014517 (2005).

[136] Miyakawa, N., Zasadzinski, J. F., Ozyuzer, L., Guptasarma, P., Hinks, D. G., Kendziora, C., and Gray, K. E. *Phys. Rev. Lett.* **83**(5), 1018–1021 Aug (1999).

[137] Zasadzinski, J. F., Ozyuzer, L., Miyakawa, N., Gray, K. E., Hinks, D. G., and Kendziora, C. *Phys. Rev. Lett.* **87**(6), 067005 Jul (2001).

[138] de Castro, G. L., Berthod, C., Piriou, A., Giannini, E., and Fischer, O. *arXiv: cond-mat/0703131* (2007).

[139] van Heumen, E., Muhlethaler, E., Kuzmenko, A., van der Marel, D., Meevasana, W., Shen, Z., and Eisaki, H. *submitted. Preprint available at condmat/0807.1730* (2008).

[140] Norman, M. R. and Chubukov, A. V. *Phys. Rev. B* **73**(14), 140501 (2006).

[141] Sangiovanni, G., Gunnarsson, O., Koch, E., Castellani, C., and Capone, M. *Phys. Rev. Lett.* **97**(4), 046404 (2006).

[142] Mishchenko, A. S., Nagaosa, N., Shen, Z.-X., Filippis, G. D., Cataudella, V., Devereaux, T. P., Bernhard, C., Kim, K. W., and Zaanen, J. *Phys. Rev. Lett.* **100**(16), 166401 (2008).

[143] Deutscher, G., Santander-Syro, A. F., and Bontemps, N. *Phys. Rev. B* **72**(9), 092504 (2005).

[144] Norman, M. R., Randeria, M., Jankó, B., and Campuzano, J. C. *Phys. Rev. B* **61**(21), 14742–14750 Jun (2000).

[145] Karakozov, A. E., Maksimov, E. G., and Dolgov, O. V. *Solid State Commun.* **124**, 119 (2002).

[146] Karakozov, A. E. and Maksimov, E. G. *Solid State Commun.* **139**, 80 (2006).

[147] Shulga, S. V., Dolgov, O. V., and Maksimov, E. G. *Physica C* **178**, 266 (1991).

[148] Mattis, D. C. and Bardeen, J. *Phys. Rev.* **111**(2), 412–417 Jul (1958).

[149] Chubukov, A. V., Abanov, A., and Basov, D. N. *Phys. Rev. B* **68**(2), 024504 Jul (2003).

[150] Lee, W., Rainer, D., and Zimmermann, W. *Physica C* **159**, 535 (1989).

[151] Zimmermann, W., Brandt, E. H., Bauer, M., Seider, E., and Genzel, L. *Physica C* **183**, 99 (1991).

[152] Marsiglio, F. *Phys. Rev. B* **44**(10), 5373–5376 Sep (1991).

[153] Ar. Abanov, A.V. Chubukov, J. S. *J. Elec. Spec. Rel. Phen.* **117**, 129 (2001).

[154] Hwang, J., Timusk, T., and Gu, G. D. *J. Phys: Cond. Mat.* **19**, 125208 (2007).

[155] Hwang, J., Timusk, T., Schachinger, E., and Carbotte, J. P. *Phys. Rev. B* **75**(14), 144508 (2007).

[156] Hwang, J., Nicol, E. J., Timusk, T., Knigavko, A., and Carbotte, J. P. *Phys. Rev. Lett.* **98**(20), 207002 (2007).

[157] Hwang, J., Carbotte, J. P., and Timusk, T. *Phys. Rev. Lett.* **100**(17), 177005 (2008).

[158] Hwang, J., Yang, J., Timusk, T., Sharapov, S. G., Carbotte, J. P., Bonn, D. A., Liang, R., and Hardy, W. N. *Phys. Rev. B* **73**(1), 014508 (2006).

[159] Hwang, J., Schachinger, E., Carbotte, J. P., Gao, F., Tanner, D. B., and Timusk, T. *Phys. Rev. Lett.* **100**(13), 137005 (2008).

[160] Thomas, G. A., Orenstein, J., Rapkine, D. H., Capizzi, M., Millis, A. J., Bhatt, R. N., Schneemeyer, L. F., and Waszczak, J. V. *Phys. Rev. Lett.* **61**(11), 1313–1316 Sep (1988).

[161] Schlesinger, Z., Collins, R. T., Holtzberg, F., C.Feild, Bickers, N. E., and Scalapino, D. J. *Nature* **343**, 242–243 (1991).

[162] Timusk, T., Porter, C. D., and Tanner, D. B. *Phys. Rev. Lett.* **66**(5), 663–666 Feb (1991).

[163] Carbotte, J. P., Schachinger, E., and Basov, D. N. *Nature* **401**(6701), 354–356 (1999).

[164] Munzar, D., Bernhard, C., and Cardona, M. *Physica C* **312**(1), 121–135 Jan (1999).

[165] Tu, J. J., Homes, C. C., Gu, G. D., Basov, D. N., and Strongin, M. *Phys. Rev. B* **66**(14), 144514 Oct (2002).

[166] Timusk, T. *J. Phys: Cond. Mat.* **127**(5), 337–348 May (2003).

[167] Lee, Y. S., Li, Z. Q., Padilla, W. J., Dordevic, S. V., Homes, C. C., Segawa, K., Ando, Y., and Basov, D. N. *Phys. Rev. B* **72**(17), 172511 (2005).

[168] Casek, P., Bernhard, C., Humlicek, J., and Munzar, D. *Phys. Rev. B* **72**(13), 134526 (2005).

[169] Zhou, X. J., Yoshida, T., Lanzara, A., Bogdanov, P. V., Kellar, S. A., Shen, K. M., Yang, W. L., Ronning, F., Sasagawa, T., Kakeshita, T., Noda, T., Eisaki, H., Uchida, S., Lin, C. T., Zhou, F., Xiong, J. W., Ti, W. X., Zhao, Z. X., Fujimori, A., Hussain, Z., and Shen, Z. X. *Nature* **423**, 398 (2003).

[170] Lee, J., Fujita, K., McElroy, K., Slezak, J. A., Wang, M., Aiura, Y., Bando, H., Ishikado, M., Masui, T., Zhu, J. X., Balatsky, A. V., Eisaki, H., Uchida, S., and Davis, J. C. *Nature* **442**, 546 august (2006).

[171] Schachinger, E., Neuber, D., and Carbotte, J. P. *Phys. Rev. B* **73**(18), 184507 (2006).

[172] Skilling, J. 45 (Kluwer, Dordrecht, 1989).

[173] Plate, M., Mottershead, J. D. F., Elfimov, I. S., Peets, D. C., Liang, R., Bonn, D. A., Hardy, W. N., Chiuzbaian, S., Falub, M., Shi, M., Patthey, L., and Damascelli, A. *Phys. Rev. Lett.* **95**(7), 077001 (2005).

[174] Shen, K. M., Ronning, F., Lu, D. H., Baumberger, F., Ingle, N. J. C., Lee, W. S., Meevasana, W., Kohsaka, Y., Azuma, M., Takano, M., Takagi, H., and Shen, Z. X. *Science* **307**, 901 (2005).

[175] Doiron-Leyraud, N., Proust, C., LeBoeuf, D., Levallois, J., Bonnemaison, J. B., Liang, R., Bonn, D. A., Hardy, W. N., and Taillefer, L. *Nature* **447**, 565–568 May (2007).

[176] Maier, T. A., Poilblanc, D., and Scalapino, D. J. *Phys. Rev. Lett.* **100**(23), 237001 (2008).

[177] G. Deutscher, P. G. d. G. *C. R. Physique* **8**, 937 (2007).

[178] Phillips, P. *Ann. Phys.* **321**, 1634 (2006).

[179] Owen, C. S. and Scalapino, D. J. *Physica* **55**, 691 (1971).

Publication List

- "Infrared spectroscopy of electronic bands in bilayer graphene"
  A.B. Kuzmenko, E. van Heumen, D. van der Marel, P. Lerch, P. Blake, K.S. Novoselov, A.K. Geim
  Preprint available at http://arxiv.org/abs/0810.2400

- "Observation of robust 55 meV resonance in the glue function of high T_c cuprates"
  E. van Heumen, E. Muhlethaler, A.B. Kuzmenko, D. van der Marel, H. Eisaki, W. Meevasana
  Preprint available at http://arxiv.org/abs/0807.1730

- "Optics clues to pairing glues in high T_c cuprates"
  E. van Heumen, A.B. Kuzmenko, D. van der Marel
  Conference proceedings article for LT25.

- "Impact of a finite cut-off for the optical sum rule in the superconducting state."
  F. Marsiglio, E. van Heumen, and A.B. Kuzmenko
  Phys. Rev. B **77**, 144510 (2008)
  Preprint available at http://arxiv.org/abs/0710.5941

- "Universal dynamical conductance in graphite."
  A.B. Kuzmenko, E. van Heumen, F. Carbone, D. van der Marel
  Phys. Rev. Lett. **100**, 117401 (2008)
  Preprint available at http://arxiv.org/abs/0712.0835

- "Optical Integral in the Cuprates and the Question of Sum Rule Violation"
  M.R. Norman, A.V. Chubukov, E. van Heumen, A.B. Kuzmenko, D. van der Marel
  Phys. Rev. B **76**, 220509(R) (2007)
  Preprint available at http://arxiv.org/abs/0709.3516

- "Optical and thermodynamic properties of the high-temperature superconductor $HgBa_2CuO_{4+\delta}$."
  E. van Heumen, R. Lortz, A.B. Kuzmenko, F. Carbone, D. van der Marel, X. Zhao, G. Yu, Y. Cho, N. Barisic, M. Greven, C.C. Homes, S.V. Dordevic
  Phys. Rev. B **75**, 054522 (2007)
  Preprint available at http://arxiv.org/abs/0610538

- "Optical probes of electron correlations in solids"
  E. van Heumen, D. van der Marel
  Lectures On The Physics Of Strongly Correlated Systems XI: Eleventh Training Course in the Physics of Strongly Correlated Systems
  Editors F. Mancini and A. Avella. AIP Conference Proceedings 918 (2006)
  Preprint available at http://arxiv.org/abs/0807.3261

- "Doping Dependence of the Redistribution of Optical Spectral Weight in $Bi_2Sr_2CaCu_2O_{8+\delta}$."
  F. Carbone, A.B. Kuzmenko, H.J.A. Molegraaf, E. van Heumen, V. Lukovac, F. Marsiglio, D. van der Marel, K. Haule, G. Kotliar, H. Berger, S. Courjault, P.H. Kes, M. Li
  Phys. Rev. B **74**, 064510 (2006)
  Preprint available at http://arxiv.org/abs/0605209

- "In-plane optical spectral weight transfer in optimally doped $Bi_2Sr_2Ca_2Cu_3O_{10}$"
  F. Carbone, A.B. Kuzmenko, H.J.A. Molegraaf, E. van Heumen, E. Giannini, D. van der Marel
  Phys. Rev. B **74**, 024502 (2006)
  Preprint available at http://arxiv.org/abs/0603737